Heinrich Heine
Universität
Düsseldorf

Method Development in Nanobiophysics

Inaugural-Dissertation

zur Erlangung des Doktorgrades der
Mathematisch-Naturwissenschaftlichen Fakultät der
Heinrich-Heine-Universität Düsseldorf

vorgelegt von

Daniel Alexander Kuckla
aus Köln

Düsseldorf, August 2023

aus dem Institut für Experimentelle Medizinische Physik
der Heinrich-Heine-Universität Düsseldorf

Gedruckt mit der Genehmigung der
Mathematisch-Naturwissenschaftlichen Fakultät
der Heinrich-Heine-Universität Düsseldorf

Berichterstatter:

1. Prof. Dr. Cornelia Monzel
   Experimentelle Medizinische Physik
   Heinrich-Heine-Universität Düsseldorf
2. Prof. Dr. Mathias Getzlaff
   Institut für Angewandte Physik
   Heinrich-Heine-Universität Düsseldorf

Tag der mündlichen Prüfung: 20.Nov.2023

Eidesstattliche Versicherung

Ich versichere an Eides Statt, dass die Dissertation von mir selbstständig und ohne unzulässige fremde Hilfe unter Beachtung der „Grundsätze zur Sicherung guter wissenschaftlicher Praxis an der Heinrich-Heine-Universität Düsseldorf“ erstellt worden ist.

Ort, Datum

Daniel Alexander Kuckla

Abstract

During this PhD, two projects were pursued.

Development of a Setup for Magnetic Hyperthermia
Magnetic hyperthermia describes heat dissipation by nanoparticles subjected to alternating magnetic fields. Due to the nanoscale localized heating, this phenomenon has a high potential for biological and medical applications. These include but are not limited to localized heating of cancerous tissue, causing conformational changes of heat sensitive molecules, and targeted drug release. However, the generation of temporally stable alternating magnetic fields remains a challenge. In this project, a robust, microscope-mountable setup for generating an alternating magnetic field is developed. For this purpose, different electrical components are tested to maximize the efficiency. The resulting setup is capable of maintaining a 100 kHz alternating magnetic field with an amplitude of 50 mT over a period of 30 min, and offers to apply fast heating-cooling cycles. An elaborate cooling system is introduced to minimize the effect of parasitic sample heating.

To test the system, Synomag® 70 particles, Bionized Nano Ferrite particles, and magnetosomes from magnetotactic bacteria (*Magnetospirillum gryphiswaldense*) are characterized in their physical and magnetic properties. The particles are compared regarding their core structure, hydrodynamic radius, surface charge, and alternating-current-susceptibility. The particles are then used to demonstrate the heating capability of the hyperthermia setup.

Track Separation in Single Particle Tracking
Intracellular transport is vital for cell division and metabolism. Single particle tracking is an essential tool for understanding these cellular processes. Today single-particle tracking can be performed on multiple particles simultaneously. Due to the high amount of data generated, computer algorithms are used to evaluate the results. In this project, an algorithm is developed which enables the separation of tracks in segments with different modes of transportation. This is accomplished via the point density of the recorded track, as criterion.

To test the developed algorithm, it is applied to tracking data of endosomes captured on an in-house built tracking setup and evaluated using the tracking algorithm u-Track. The resulting separation is then compared to the established analysis via mean square displacement theory, verifying the viability of the developed approach.

Contents

I

Magnetic-Hyperthermia

1 Introduction

Thinking about the energy which is critical for our world to function, one might quickly think of electric energy as power supply to almost every part of the infrastructure. This sounds reasonable, especially in times when almost every device of our everyday life operates with electric energy. A much more critical type of energy, which is, in fact, so important that it defines the habitable zone [1], is thermal energy. Concerning the vast range of temperatures appearing in nature, the one we can live in is particularly limited. Even more limited is our body temperature range of 20 °C to 44 °C at its maximum and 33 °C to 40 °C to the bearable extent without significant reduction of vital functions [2]. While the strong temperature dependence of human life can be a problem in extreme environmental temperatures, it also poses an excellent opportunity for medical treatment.

The best-known examples of thermal treatments are probably the hot-water bag and the ice pack. While the ice pack, representing cold, is used for short-term treatment of new injuries, the hot-water bag, representing heat, is used to mitigate physical afflictions.

The human body itself uses temperature to counter diseases in the form of fever. This is possible since biological processes are highly temperature dependent. Suppressing this natural defense mechanism has been linked to prolonging the duration of illnesses [3, 4] or increasing the mortality rate of patients [5]. There are also indications that fever can aid the recuperation from cancer [6, 7]. The downside of fever is the strain on the whole body. To minimize side effects on the surrounding healthy tissue, localized heat generation at the tumor side is preferable.

To generate heat locally, a commonly used technique is the implantation of heating devices, either by using implanted electrodes [8, 9] or microwave antennas [10, 11, 12]. Due to the low heat penetration inside the body, the heating devices must be placed close to the tumor. The techniques are invasive and therefore risk mechanical damage to the tumor, which can lead to metastasis spread. A noninvasive technique is preferable. One approach towards noninvasive localized hyperthermia is magnetic hyperthermia. In magnetic hyperthermia, magnetic nanoparticles are administered to the patient,

which then accumulate in the tumor. The high penetration of magnetic fields into tissue enables the remote heating of nanoparticles. In 1957 Gilchrist et al. [13] showed the treatment of cancerous lymph nodes by remotely stimulating magnetic nanoparticles with alternating magnetic fields. From this point on, the effectiveness of magnetic hyperthermia in cancer treatment has been shown numerous times [14, 15, 16, 17, 18, 19].

Aside from the use of magnetic hyperthermia in cancer therapy, there are other applications of magnetic hyperthermia. Here especially, the extremely high localization of the heat generated is of interest. Due to their extremely small size of only tens to a few hundred nanometers, it is possible to attach the particles to individual regions of the cell and control, for instance, individual ion channels [20, 21, 22]. The influence has also been shown for other cell functions [21, 23, 24].

A different use case of magnetic nanoparticles than the direct influence of biological processes is the aid in drug releases. Here the drug delivery system contains magnetic nanoparticles, which are used to initiate drug release [25, 26, 27].

Beyond the medical applications, there are also other systems where magnetic hyperthermia is used, such as the purification of proteins [28], water purification [29, 30], and the development of heat and pH-sensitive polymers [31].

1.1 Outline of this Project

This project focuses on the biomedical application of magnetic nanoparticles. It is aimed to provide a robust magnetic hyperthermia setup that can be used for live imaging of cells with magnetic nanoparticles under the influence of alternating magnetic fields.

The second chapter discusses the theoretical basics of electromagnetism, magnetism in matter, and the general heat generation of magnetic nanoparticles. Afterwards, the evaluation method applied in this project is introduced.

The third chapter introduces the methods used for the characterization of nanoparticles, namely dynamic light scattering, electrophoretic light scattering, transmission electron microscopy, and alternating current susceptometry are introduced. The chapter then closes with the introduction of thermal imaging, which is used to measure heat generation.

The fourth chapter discusses the experimental setup and its ability to generate heat. At first, several components are tested and characterized towards the applicability in a

high-power alternating current circuit. The characterized materials are then combined into a resonant transformer as the basic principle of the setup. To reach the full potential of the setup and decrease the influence on the sample, a custom water cooling system is fabricated and fitted to the setup. The setup is then thoroughly characterized by its electric and magnetic properties.

In the second part of chapter four, three different magnetic nanoparticles are characterized to serve as test systems to determine the usability of the proposed setup to generate heat by exposing the characterized particles to an alternating magnetic field.

Finally, the system is tested with the characterized particles towards its usability for microscopic observation of biological systems. For this purpose, the heat generation, the influence of parasitic heating by heat radiated from the setup, and the usability of the setup in combination with a microscope, and microscopable chambers are tested.

In the fifth chapter, the results are discussed, and a conclusion on the usability is given.

1.2 Contributions and Publications

This project has been conducted in the group for Experimental Medical Physics. As the research is interdisciplinary, I have collaborated closely with other group members. Additionally, I have supervised several students during their thesis.

1.2.1 Contribution to this Thesis

A detailed list of contributions to the data shown is given in the following.

- Dr. Philipp Hagemann performed and evaluated dynamic light scattering and ζ-sizer measurements on Bionized Nano Ferrite particles and Synomag® 70 particles.
- Andreas Neusch performed and evaluated transmission electron microscopy measurements on Bionized Nano Ferrite particles and Synomag® 70 particles.
- Bastian Czech cultivated *Magnetospirillum gryphiswaldense*, provided magnetosomes with transmission electron microscopy measurements and properties thereof. He also assisted with hyperthermia and AC-Susceptibility measurements on the magnetosomes. This was done in the scope of his master thesis.

- Julia-Sarita Brand performed the measurements of the coupling factor and assisted during hyperthermia measurements. This was done in the scope of her bachelor thesis.
- Vinzenz Jüttner performed the spatial measurement of the magnetic field strength and assisted during hyperthermia measurements.

1.2.2 Publications

The results from this project are submitted for publication:
An efficient magnetothermal actuation setup for fast heating/cooling cycles or long-term induction heating of different magnetic nanoparticle classes
in *Journal of Physics D: Applied Physics*.
The authors are: Kuckla, Daniel; Brand, Julia-Sarita; Neusch, Andreas; Czech, Bastian; Jüttner, Vinzenz; Asharion, Amirarsalan; Novoselova, Iuliia; Getzlaff, Mathias; Monzel, Cornelia.

Parts of this work have been published in posters on different occasions.

- Poster at DPG Frühjahrstagung Regensburg 2022: *An Efficient Magnetic Hyperthermia Setup for Controlled Nanoparticle Heating*
  Authors: Kuckla, Daniel; Asharion, Amirarsalan; Brand, Julia-Sarita; Jüttner, Vinzenz; Czech, Bastian; Getzlaff, Mathias; Monzel, Cornelia.
- Poster at SKM 2021: *Hyperthermia Setup for Efficient Nanoparticle Heating*
  Authors: Kuckla, Daniel; Asharion, Amirarsalan; Brand, Julia-Sarita; Jüttner, Vinzenz; Monzel, Cornelia.

Parts of this project are also included in supervised bachelor and master theses and cooperative works.

- Amirarsalan Asharion: *Design and Implementation of a Magnetothermal Actuation Setup* (Master Thesis)
- Julia-Sarita Brand: *A Magnetothermal Actuation Setup for Magnetic Nanoparticle Heating* (Bachelor Thesis)
- Bastian Czech: *Hyperthermie: Untersuchung von Eisenoxid-Nanopartikeln aus Magnetospirillum gryphiswaldense Bakterien* (Master Thesis, cooperational)

2 Theoretical Background

In this chapter, a short recapitulation of the underlying physical basics of this work shall be given in order to aid the understanding of this work. Effects that directly affect the development of the setup are explained in the corresponding section of the work. The chapter starts with the foundation of electromagnetism, namely the Maxwell equations and the Lorentz force; it continues with the effect of magnetism in matter, focusing on the phenomenon of superparamagnetism and the linear response theory. The chapter closes with a motivation for heating and cooling fit formulas.

2.1 Maxwell and Lorentz equations

The basics of classical electromagnetism are given by a set of five equations. The first four are the Maxwell equations constituted by James Clerk Maxwell in 1865 [32], albeit in different forms. Nowadays, two commonly known forms of these equations exist in the International System of Units (SI). The first is the microscopic or differential form which reads as [33]

$$\vec{\nabla} \cdot \vec{E} = \frac{\rho}{\epsilon_0}, \tag{2.1}$$

$$\vec{\nabla} \cdot \vec{B} = 0, \tag{2.2}$$

$$\vec{\nabla} \times \vec{E} = -\frac{\partial \vec{B}}{\partial t} \text{ and} \tag{2.3}$$

$$\vec{\nabla} \times \vec{B} = \mu_0 \vec{j_c} + \mu_0 \epsilon_0 \frac{\partial \vec{E}}{\partial t}. \tag{2.4}$$

These equations describe the dependencies of the electric field $\vec{E}$, charge density ρ, magnetic flux density $\vec{B}$, and the total current density $\vec{j_c}$ with the vacuum permittivity ϵ_0 and the vacuum permeability μ_0. The physical statements of these equations are:

- The divergence of the electric displacement field is proportional to the free charge density, so charges are the source of the electric field. (Equation (2.1))
- There is no divergence of the magnetic field, meaning there is no source of

the magnetic field. In other words, there are no magnetic monopoles. (Equation (2.2))

- Every temporal change in the magnetic flux causes a curled electric field. (Equation (2.3))
- A temporal changing electric field and/or a current cause a curled electric field. (Equation (2.4))

The second form is the macroscopic or integral form which can be transformed from the differential form by utilizing Gauss's theorem and the generalized Stokes theorem (Appendix A.1). They read as [33]

$$\oiint_{\partial V} \vec{D} \cdot \mathrm{d}\vec{A} = Q, \tag{2.5}$$

$$\oiint_{\partial V} \vec{B} \cdot \mathrm{d}\vec{A} = 0, \tag{2.6}$$

$$\oint_{\partial A} \vec{E} \cdot \mathrm{d}\vec{s} = -\frac{\mathrm{d}\Phi_\mathrm{B}}{\mathrm{d}t} \text{ and} \tag{2.7}$$

$$\oint_{\partial A} \vec{H} \cdot \mathrm{d}\vec{s} = \vec{i} + \frac{\mathrm{d}\Phi_\mathrm{D}}{\mathrm{d}t}. \tag{2.8}$$

The physical meanings of the integral form are:

- The electric displacement field $\vec{D}$ through a closed surface $\vec{A}$ around a Volume V is caused by the overall charge Q inside the Volume. (Equation (2.5))
- The total magnetic flux through a closed surface is equal to zero due to the non-existence of magnetic monopoles. (Equation (2.6))
- The electric circulation around a surface A along its perimeter s opposes the temporal change of magnetic flux $\mathrm{d}\Phi_\mathrm{B}$ through the surface. (Equation (2.7))
- The circulation of the magnetic field strength $\vec{H}$ around a surface equals the temporal change of the electric displacement field and the current density $\vec{i}$ through the surface. (Equation (2.8))

The electric displacement field $\vec{D}$ and the magnetic field strength $\vec{H}$ are thereby given by [33]

$$\vec{D} \coloneqq \epsilon_0 \vec{E} + \vec{P} \text{ and} \tag{2.9}$$

$$\vec{H} \coloneqq \frac{\vec{B}}{\mu_0} - \vec{M}, \tag{2.10}$$

with the polarization $\vec{P}$ and the magnetization $\vec{M}$. Polarization and magnetization are macroscopic material properties that are used to describe the influence of electric and

magnetic dipole moments of permanent or temporal character. These effects can not be explained by the microscopic Maxwell equations and classical electromagnetism, as they are caused by quantum mechanical effects.

The last equation needed is the electromagnetic force or Lorentz force $\vec{F}_{\mathrm{L}}$, which is given by [34, p.89]

$$\vec{F}_{\mathrm{L}} = q\left(\vec{E} + \vec{v} \times \vec{B}\right).$$

It describes the force acting on a charge q in the presence of an electric field and the effect a magnetic field has on the charge moving with the velocity $\vec{v}$ through the magnetic field.

2.2 Magnetism in Matter

As discussed in section 2.1, magnetization describes the influence of magnetic dipole moments in matter. These dipole moments can be of permanent or temporal character. Permanent dipole moments are a material inherent quantum-mechanical property, while temporal dipole moments are induced by external magnetic fields. However, the response to external magnetic fields can be vastly different. The responses can be categorized using the magnetic permeability

$$\mu \coloneqq \frac{B}{H},$$

which is the proportionality factor of magnetic flux density and magnetic field strength and therefore describes the ability of a material's magnetization to follow an external magnetic field. μ is the permeability of a material, which is the product of the vacuum permeability μ_0 and the relative permeability μ_{r}[35]. In the following, the different magnetic behaviors will be introduced. The same classification can be done with the magnetic susceptibility, which is given by $\chi = \mu_{\mathrm{r}} - 1$.

Diamagnetism : $0 \leq \mu < 1$
A magnetic permeability below one means the magnetic flux density inside a diamagnetic material is lower than it would be in a vacuum. Therefore the magnetic dipoles inside the material need to be oriented opposing the external magnetic field strength, resulting in a net force causing the material to leave the magnetic field. Due to this force, it is possible to keep diamagnetic materials levitating in sufficiently strong magnetic fields. In the case of $\mu = 0$, the magnetic field inside the material completely

vanishes; this is called the Meissner–Ochsenfeld effect [36], a key property of superconductors.

Paramagnetism : $\mu > 1$
In this case, the magnetic flux density inside the material is larger than it would be in a vacuum. This is the case for most materials. Regarding internal dipole behavior, the dipoles orient themselves with the external magnetic field. This leads to a net force causing the material to enter an external magnetic field. Although paramagnetic materials align their magnetic dipoles in the presence of an external magnetic field, they do not retain their magnetization when the external field vanishes, and the material does not have an inherent magnetization.

2.2.1 Collective/Ordered Magnetism

Collective or ordered magnetism describes the phenomenon of magnetic moments inside the material aligning without external magnetic fields. Although only some of these materials exhibit a natural net magnetization, this type of behavior is colloquially known as magnetism.

Ferromagnetism : $\mu >> 1$
In ferromagnetic materials, the internal dipoles are divided into regions called magnetic domains. Inside these domains, the magnetic dipole moments are aligned parallel (Figure 2.1a) even if no external magnetic field is applied. The cause of this alignment is not explainable with a classical approach. In the quantum mechanical picture, the alignment is caused by the exchange interaction, which is no additional type of interaction but a coulomb interaction causing the alignment of spins to be energetically favorable for certain materials.

Since these domains do not need to be aligned with each other, the material does not need to exhibit an externally measurable magnetic field. In the presence of an external magnetic field, however, the domains are aligned and increase the magnetic flux density by up to 1×10^6 [37]. If the external field is removed, the thermal energy at room temperature is insufficient to break the alignment of the magnetic moments inside a domain, so an intrinsic magnetization remains. This magnetization is called remanent magnetization, which will be further explained in Section 2.2.2. If the temperature increases above the material-dependent Curie-temperature T_C, the thermal energy is sufficient to break the alignment of the magnetic domains, leading to magnetization loss. At temperatures higher than T_C, the material shows paramagnetic behavior.

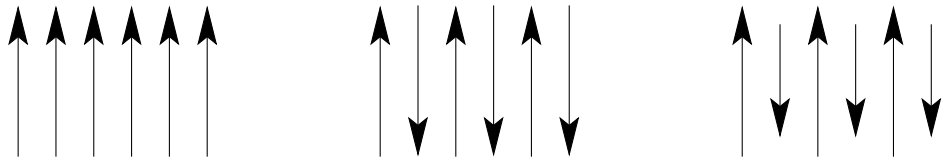

(a) Ferromagnet **(b)** Antiferromagnet **(c)** Ferrimagnet

Figure 2.1: Relative alignment of magnetic moments for different types of ordered magnetism.

Antiferromagnetism :
Antiferromagnetic materials, just like ferromagnets, align their magnetic moments. The difference is that the lattice of magnetic moments is separated into two groups which are oriented antiparallel (Figure 2.1b). This leads to a net magnetic moment of zero. In the presence of an external magnetic field, the magnetic moments are rotated in line with the external magnetic field. If the moments are fully aligned with the external magnetic field, there is no longer a difference to a ferromagnetic system. Just like ferromagnets, the alignment of the magnetic dipole moments can be revoked if the temperature is increased and the thermal energy is sufficient to overcome the alignment. In the case of antiferromagnets, this temperature is called Néel temperature T_{N}. Above T_{N} antiferromagnets exhibit paramagnetic behavior.

Ferrimagnetism :
Ferrimagnets are antiferromagnets with magnetic dipoles of different magnitudes. This leads to a net magnetic moment even if neighboring magnetic moments are aligned antiparallel (Figure 2.1c). Due to the remaining net magnetic moment of the magnetic domains, ferrimagnets also exhibit a remanent magnetization. If a ferrimagnet is heated above T_{C}, it exhibits paramagnetic behavior. A sketch of the magnetic moments is shown in Figure 2.1c.

2.2.2 Hysteresis

In general, hysteresis describes a behavior where the state of a system is dependent not only on momentary external input but also on the system's previous state. In magnets, this behavior is a result of the anisotropy of the magnetic crystal. The anisotropy is caused by the interaction of electron orbitals and the crystallographic structure. As a result of this interaction, the spins prefer to be aligned along specific axes, which are defined by the crystallographic structure and are energetically favorable [38]. The axis along which these orientations are aligned are called easy axes. In the

simplest case, a crystal possesses one easy axis. Therefore the magnetic moment has two favorable orientations, namely parallel and antiparallel to the easy axis. To switch the orientation, the magnetic moment needs to be rotated, surpassing energetically higher orientation states, which creates an energy barrier between the two favorable orientations. Due to this energy barrier, the orientation of the moment is switched only if the supplied energy is larger than the energy barrier. As a result, the orientation of the magnetic moment is dependent not solely on an external magnetic field but also on the orientation the magnetic moment is in before the external field is applied. The magnetization which is present inside a material after it is removed from an external magnetic field is called remanent magnetization M_r.

As described in Section 2.2 Ferromagnetism and Ferrimagnetism, these types of materials exhibit a remanent magnetization. In ideal crystals, the hysteresis is only caused by anisotropy. In real crystals, however, the hysteresis is increased by a slip-and-stick type of motion of the domain walls. Domain walls are the transition region between two neighboring magnetic domains. Depending on the material, the angular difference of neighboring domains can vary. For a phase change of 180°, there are two different wall types. The first is the Bloch wall, characterized by a spin rotation around an axis perpendicular to the magnetic moment orientation and wall plane. The second is the Néel wall, characterized by a spin rotation around an axis perpendicular to the magnetic moment but in the wall plane. If an external magnetic field is applied, the domain walls are rearranged to form a larger domain hence a larger net magnetic moment. This process increases the material's magnetization until all magnetic moments are aligned in the same direction. If the external magnetic field is removed, the magnet is no longer in the energetic minimum due to the energy stored in the demagnetizing field. The demagnetizing field is the magnetic stray field generated by the material's magnetization. In the absence of an external magnetic field ($\vec{H} = 0$), the resulting magnetic field $\vec{B}$ is solely caused by the magnetization $\vec{M}$ (Equation (2.10)). To reduce the energy stored in the stray field, the magnetization needs to be reduced. Demagnetization is caused by either splitting or rearrangement of domains or by moving domain walls. However, domain walls tend to get stuck in lattice defects during this movement. The pinned domain walls impede the demagnetization, thus increasing the remanent magnetization and the hysteresis effect. If the energy available to move the wall is sufficient, the domain walls tend to slip to the next lattice defect. The magnitude of demagnetization is dependent on the magnetized material.

In Figure 2.2, an arbitrary magnetic hysteresis curve is depicted. To classify magnetic materials, three distinctive parameters, extractable from the curve, are of interest: The saturation magnetization M_max, which directly influences the maximum achievable flux

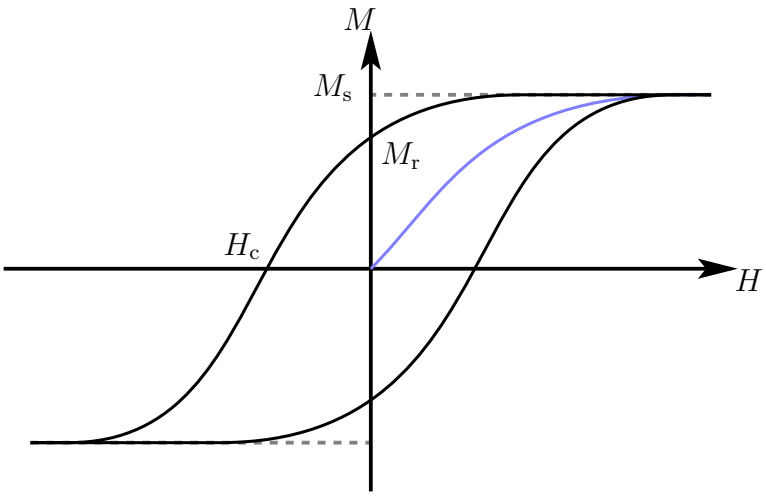

Figure 2.2: Exemplary hysteresis curve which indicates remanent magnetization M_r, coercive field strength H_c and saturation magnetization M_s. The initial magnetization curve (blue) can only be measured in previously non-magnetized materials

density B_{max} in the presence of an external magnetic field; the remanent magnetization M_r, which defines the residual magnetization after removing the magnet from an external field; and the coercive field H_c, which is the field needed to demagnetize the material completely. The ability of a material to retain magnetization is called magnetic hardness. Materials that retain a high remanent magnetization are called magnetically hard, while materials that retain close to no remanent magnetization are called magnetically soft. The desired behavior depends on the use case. While magnetically hard materials are favorable for data storage on hard drives due to the unlikeliness of spontaneous demagnetization, magnetically soft materials are favorable in the case of applications that demand frequent switching of magnetization direction. Examples of this are transformers or alternating current-driven electromagnets due to the hysteresis losses. These losses arise from the energy required to change the magnetization. The energy is converted to heat and is directly proportional to the area inside the hysteresis loop Appendix A.1. The energy converted can be calculated using

$$E_H = -\mu_0 \oint M \mathrm{d}H, \tag{2.11}$$

where E_H is the energy dissipated, μ_0 is the magnetic permeability of the vacuum, M is the magnetization, and H is the magnetic field strength.

2.2.3 Superparamagnetism

Superparamagnetism is a material property of ferro- and ferrimagnets if the size of the material is below a material-dependent limit. When reducing the size of a magnet, the amount of domains is reduced due to material removal. If the magnet size is reduced sufficiently, the number of domains is reduced to one. In the absence of an external magnetic field, the orientation is mainly determined by the anisotropy of the crystal. As described in Section 2.2.2, in the simplest case, a magnetic crystal possesses one easy axis. In the case of nanoparticles, switching of the energetically favorable orientations is possible via two relaxation mechanisms. The first is the Brownian relaxation which describes a change in magnetic moment caused by the rotation of the nanoparticle. The second is the Néel relaxation mechanism which describes a flip of magnetization moment along the easy axis of the magnetic crystal. The switching of the orientation needs to overcome this energy barrier. If the energy barrier is now in the order of magnitude of the thermal energy, the switching can happen spontaneously. Particles where the energy needed to switch the magnetization is lower than thermal energy at room temperature are called superparamagnetic [1]. If the particle is, however, cooled further, the thermal energy is reduced, and the magnetic moments are blocked. The temperature at which the thermal energy is equal to the energy difference is called blocking temperature T_{BT} and is given by

$$T_{\mathrm{BT}} = \frac{\Delta E}{k_{\mathrm{B}}},$$

with the energy barrier ΔE and the Boltzmann constant k_{B}. The switching of the magnetic moment happens with the period of

$$\tau = \tau_0 \mathrm{e}^{-\frac{\Delta E}{k_{\mathrm{B}} T}},$$

where τ_0 is the attempt time, a material-specific constant [38]. As a result of the frequent switching of the magnetic moment, the net magnetization $\vec{M}$ vanishes.

[1] The "super" is to note the large magnetic moment of the particles compared to normal paramagnets.

2.3 Linear Response Theory

In Section 2.1, the dependence of magnetic field strength, magnetic flux density, and magnetization is introduced in Equation (2.10). This formula can be rearranged to

$$\begin{aligned}\vec{B} &= \mu_0 \left(\vec{H} + \vec{M}\right) \\ &= \mu_0 \left(1 + \chi\right) \vec{H} \\ &= \mu_0 \mu_\mathrm{r} \vec{H},\end{aligned} \tag{2.12}$$

with the magnetic susceptibility χ and the relative permeability $\mu_\mathrm{r} = (1 + \chi)$. This equation holds true for linear media in temporally stable or slowly changing magnetic fields. In sinusoidal magnetic fields, the magnetization will also show sinusoidal behavior. To be able to describe this behavior, Rosensweig developed the linear response theory[2] [39]. While the theory has some flaws, which will be discussed at the end of the chapter, it represents a simple description to understand the processes causing hysteretic heating in single-domain particles. The following explanation follows the work of Rosensweig. The idea is to describe magnetization as a complex entity. This gives the possibility to describe the sinusoidal behavior, including a phase shift towards the external magnetic field. The resulting magnetization can then be written as

$$\begin{aligned}M(t) &= \Re \left(\chi H(t)\right) \\ &= \Re \left(\chi H_0 \mathrm{e}^{\mathrm{i}\omega t}\right) \\ &= H_0 \left(\chi' \sin\left(\omega t\right) + \chi'' \cos\left(\omega t\right)\right),\end{aligned} \tag{2.13}$$

with $\chi = \chi' + \mathrm{i}\chi''$, ω the angular frequency of the external field, and the time t. For an externally applied magnetic field of the form

$$H(t) = H_0 \cos\left(\omega t\right) = \Re \left(H_0 \mathrm{e}^{\mathrm{i}\omega t}\right). \tag{2.14}$$

Inserting these formulas into Equation (2.11) leads to

$$\Delta E = 2\mu_0 H_0^2 \chi'' \int_0^{2\pi/\omega} \sin^2\left(\omega t\right) \mathrm{d}t, \tag{2.15}$$

[2] There are several theories with this name.

which leads to

$$E_{\mathrm{H}} = \frac{2\pi\mu_0 H_0^2 \chi''}{\omega}.$$

Due to the sole dependence of E_{H} on the out-of-phase component, it is also called the loss component. The power P dissipated is the energy loss per cycle multiplied by the cycles per second; therefore, it can be calculated by

$$P = f E_{\mathrm{H}} = f\mu_0\pi\chi'' H_0^2, \tag{2.16}$$

where f is the frequency of the external field. As visible in Figure 2.2, the area inside the hysteresis curve is caused by the remanent magnetization; if there is none, the hysteresis curve does not enclose any area. However, the phase shift between field and magnetization causes the loop to open again. Figure 2.3b shows the resulting hysteresis loops for different frequencies caused by the arbitrary susceptibility shown in Figure 2.3a. The susceptibility for the plot is given by

$$\chi' = \frac{\chi_0}{1 + (\omega t)^2},$$
$$\chi'' = \frac{\chi_0 \omega\tau}{1 + (\omega t)^2},$$

with the relaxation time τ. It is visible that the χ is dependent on the frequency and therefore differs from the material's susceptibility in the presence of a static magnetic field. As a result of this, it is also called **A**lternating **C**urrent **S**usceptibility (ACS). The vanishing of the hysteresis loop does have different causes for the limits of $f \to 0$ and $f \to \infty$. For close to DC ($f \to 0$) fields, there is no hysteresis loop as the particles can follow the external field without a phase lag, resulting in a closed hysteresis loop along the $y = x$ diagonal. For $f \to \infty$, the magnetic moments cannot follow the external magnetic field resulting in no magnetization, which leads to a closed hysteresis loop along the x-axis.

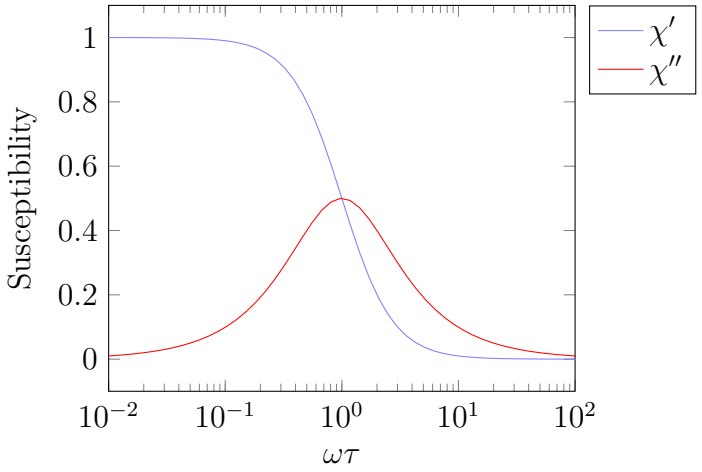

(a) Simulated AC-Susceptibility for a superparamagnetic particle system. Showing the regime of χ' and χ'' according to Rosensweigs model.

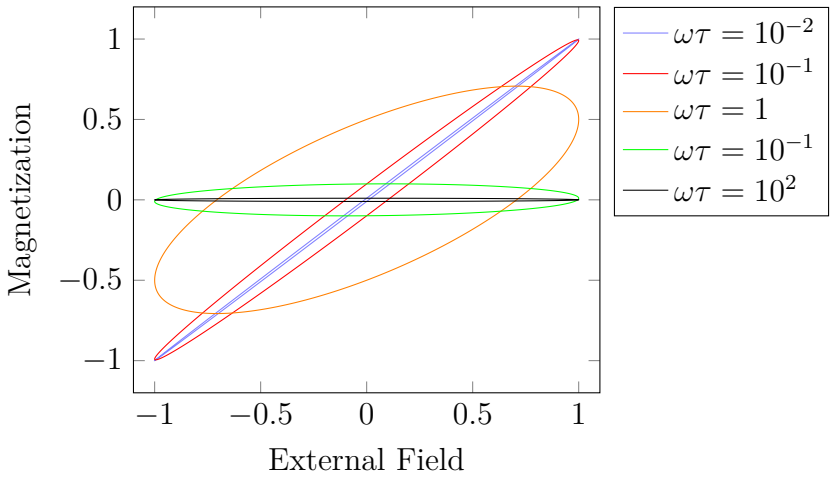

(b) Hysteresis loops resulting from the ACS shown in a) for different values of $\omega\tau$.

Figure 2.3: Exemplary ACS and hysteresis loops according to Rosensweig's linear response theory.

As mentioned at the beginning of this chapter, the linear response theory does have flaws. The most obvious is that it states that the energy dissipated can be increased endlessly by increasing the external magnetic field. The impossibility of this is evident. To overcome this, the field dependence of the susceptibility, caused by the dependence on the relaxation times [40], is implemented by the Langevin equation

$$L(\xi) = \coth(\xi) - \frac{1}{\xi} = \frac{M}{M_s}$$

and introduced into Equation (2.16). Where $\xi = \mu_0 M_\mathrm{d} H V_\mathrm{m}/k_\mathrm{B}T$, $M\mathrm{s} = \phi M_\mathrm{d}$ is the saturation magnetization with the domain magnetization M_d and ϕ the volume fraction of solids. This results in

$$P = \pi\mu_0 M_\mathrm{s} H_0 L\left(\xi\right) f \frac{2\pi f\tau}{1+\left(2\pi f r\right)^2}. \tag{2.17}$$

This formula is proportional to H_0^2 for low H_0 and a linear dependence for high H_0, causing $L\left(\xi\right)$ to reach saturation. While the ongoing linear dependence of P is H_0 is still impossible, this gives a good representation within the viability of this model.

2.4 Heating and Cooling Formulas

The temperature of an object is mainly influenced by its environment due to the exchange of energy, which strives for equilibrium. Therefore the energy of the object with a higher temperature is transferred to the object with a lower temperature until both objects have the same temperature. It needs to be remembered that the same temperature does not mean the same amount of energy as the temperature change

$$\Delta T = T(0) - T(t) \tag{2.18}$$

of an object is the quotient of supplied energy Q and the heat capacitance C [41]

$$\Delta T(t) = \frac{Q(t)}{C}, \tag{2.19}$$

where ΔT is the temperature difference between the temperature at the beginning of the measurement $T(0)$ and the temperature at a later time point $T(t)$. The energy can be transferred from one object to another by three mechanisms. The first one is thermal conduction which describes the direct transfer of energy from one object to another by lattice vibrations. For electrical conductors the direct transport of thermal energy is also influenced by the movement of electrons, this effect is called Wiedemann–Franz law [42] . The second is convection which describes the transfer of heat inside a fluid or gas by the flow of the fluid or gas caused by thermal differences inside. The third effect is thermal radiation, which describes energy transfer via electromagnetic radiation.

The change in temperature is described by Newton's law of cooling [43, p.13], which states that the temperature change of an object is proportional to the temperature

difference between the object and its surrounding given by

$$\dot{Q}(t) = hA\Delta T(t),$$

with the heat transfer coefficient h and the heat transfer area A. Equation (2.19) enables the formula to be rewritten as

$$\frac{\partial \Delta T}{\partial t} = \frac{hA}{C}\Delta T.$$

This differential equation can be solved by

$$\Delta T = \Delta T_{\max} \mathrm{e}^{\frac{hA}{C}t}.$$

With Equation (2.18), this can be rewritten to

$$T(t) = T_{\mathrm{env}} + \Delta T \mathrm{e}^{-t\frac{hA}{C}}. \tag{2.20}$$

Here $T(0)$ is substituted with the environmental temperature T_{env}, which is possible if the sample is given enough time to reach thermal equilibrium with its environment prior to the measurement. Therefore the cooling can be described with Equation (2.20); the heating, however, does show the inverse behavior with a steep increase at the beginning. The formula can be found via the change in energy, which is

$$\dot{Q}_{\mathrm{eff}} = \dot{Q}_{\mathrm{heat}} - \dot{Q}_{\mathrm{diss}}$$

with the effective energy change $\dot{Q}_{\mathrm{eff}}$, the energy change due to heating $\dot{Q}_{\mathrm{heat}}$, and the energy change due to dissipated energy $\dot{Q}_{\mathrm{diss}}$. The steady temperature reached indicates no net energy change. Therefore the maximum reached dissipated energy $\dot{Q}_{\mathrm{diss,max}}$ must be equal to the energy generated by heating $\dot{Q}_{\mathrm{heat}}$, leading to

$$\dot{Q}_{\mathrm{heat}} = \dot{Q}_{\mathrm{diss,max}} = hA\Delta T_{\max}. \tag{2.21}$$

Utilizing the temporal derivative of Equation (2.19) and the equality of the derivative of temperature and temperature difference, Equation (2.21) can be rewritten as

$$\frac{\partial T}{\partial t} = \frac{C}{hA}\Delta T_{\max} - \frac{C}{hA}\Delta T.$$

This differential equation is solved by

$$\begin{aligned}\Delta T(t) &= \Delta T_{\max} + \Delta T_{\max} \mathrm{e}^{-t\frac{hA}{C}} \\ &= \Delta T_{max}\left(1 - \mathrm{e}^{-t\frac{hA}{C}}\right),\end{aligned}$$

where the boundary conditions lead to the constant in front of the exponential. The boundary conditions are

$$\Delta T(0) = 0$$

and

$$\Delta T(\infty) = \Delta T_{\max}.$$

Just like above, this can be converted using Equation (2.18) to

$$T(t) = \Delta T_{\max}\left(1 - \mathrm{e}^{-t\frac{hA}{C}}\right) + T_{\mathrm{env}}. \tag{2.22}$$

Utilizing the fit results, the maximum temperature reached can be calculated by

$$T_{\max} = \Delta T_{\max} + T_{\mathrm{env}}. \tag{2.23}$$

3 Methods

The aim of this chapter is to introduce the standard methods used in this project ranging from **D**ynamic **L**ight **S**cattering (DLS), **E**lectrophoretic **L**ight **S**cattering (ELS), **T**ransmission **E**lectron **M**icroscopy (TEM), and **A**lternating **C**urrent **S**usceptibility (ACS) measurements which were used for particle characterization, to thermal imaging for the hyperthermia measurements. The methods will be introduced in the different sections, and the limitations and problems concerning their use in this work will be discussed.

3.1 Particle Characterization

For particle characterization, multiple techniques have been used in order to achieve a comprehensive understanding of the particles. For this purpose, the core radius and structure, the hydrodynamic size, the ζ-potential, and the AC-susceptibility have been determined.

3.1.1 Dynamic Light Scattering

DLS is a technique used to determine the hydrodynamic radius of a particle. The hydrodynamic radius, or more precisely, Stokes radius, is the radius of a solid sphere that would exhibit the same diffusive behavior as the measured particle. The radius does not necessarily represent the physical radius of the particle, as the diffusive behavior is influenced by the shape and hydration shell of said particle. The underlying principle of DLS is the scattering of light. If light is shone on a solution with particles and the particles are small compared to the wavelength of the incident light, the dominating effect is Raleigh scattering. It describes the elastic scattering of electromagnetic radiation on particles that are considerably smaller than the wavelength of the scattered radiation. The intensity of the light being scattered is dependent on the particle size, as described in

$$I = I_0 \frac{1 + \cos^2(\theta)}{2R^2} \left(\frac{2\pi}{\lambda}\right)^4 \left(\frac{n^2 - 1}{n^2 + 2}\right) r^6, \tag{3.1}$$

with I_0 being the intensity of the incident light, R being the distance between the path of the incident photon and a parallel line through the particle center, θ being the scattering angle, λ being the wavelength of the light, n being the refractive index of the particle and r being the radius of the particle. The geometric parameters are shown in Figure 3.1b. Due to the fixed angle of the detector, the intensity is solely dependent on the particle size. Moving scattering centers result in a temporarily changing intensity distribution. This is due to a particle's spatially changing scattering pattern when moving. The change rate depends on the particle velocity and can be quantified by the $g^{(1)}$ autocorrelation function. Which is given by [44]

$$g^{(1)}(\tau) = \frac{\langle E^*(t)E(t+\tau)\rangle}{\langle |E(t)^2| \rangle}. \tag{3.2}$$

$g^{(1)}$ is a measure for the self-similarity of the electric field E of the signal [44]. With a changing measurement signal, the self-similarity decays. The decay is exponential and correlated to the motion of the particles; the faster the particles, the faster the decay. In its simplest form, the diffusion constant can be extracted via

$$g(q, \tau) = \exp(-\Gamma\tau), \tag{3.3}$$

where Γ is the decay rate which relates to D via [44]

$$\Gamma = K^2 D \tag{3.4}$$

with

$$K = \frac{4\pi n_\mathrm{s}}{\lambda} \sin\left(\frac{\alpha}{2}\right), \tag{3.5}$$

where n_s is the refractive index of the particle solution, λ is the laser wavelength, and α is the detector angle [45, p.15], as depicted in Figure 3.1a.

While this holds true for strictly monodisperse samples, for polydisperse samples, the autocorrelation function is a superposition of the exponential decays caused by different monodisperse samples. The method of cumulants is used to determine the distribution function of decay rates [44]. The system used in this project (Zetasizer, Malvern Panalytical, Malvern UK) performs the method of cumulants by fitting a polynomial to the logarithmized $g^{(1)}$-correlation function. Outgoing from the linear component,

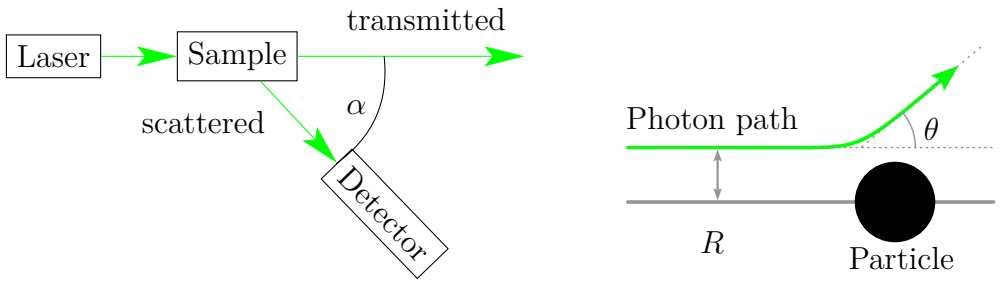

(a) Schematic of a DLS-Setup, with indicated transmitted beam path, scattered beam bath, and detector angle α.

(b) Schematic showing the geometrical parameters used in Equation (3.1). R is the distance between the path of the incident photon and a parallel line through the particle center, and θ is the scattering angle.

Figure 3.1: Schematics for the DLS setup and the geometry of RaYleigh scattering.

the size distribution is extracted using instrument parameters and the viscosity of the dispersion medium. [46] A different method is to determine the size distribution by comparing the measured data to a DLS-measurements database to assess the underlying size distribution [47]. From Equation (3.1), it is visible that the intensity is dependent on the particle radius to the power of six, which means that larger particles contribute more to the reflected intensity. The measured distribution is an intensity distribution, not giving easily understandable insight into the distribution of particle sizes. It can be recalculated into a number distribution, as the intensity scattered for each particle is known by Equation (3.1). The size distribution represents the amount of particles with a certain size in the solution. The particle radius r used in Equation (3.1) is only well defined for spherical particles, which in turn indicates that these measurements for non-spherical particles need to be interpreted with this limitation in mind. The used system can determine the size of particles in the range of 0.3 nm up to 10 µm [46].

The samples for DLS have been prepared for measurements by diluting the particles in HEPES[3] buffer (0.2 mol/L, pH 7.0). For magnetosomes, the measurements have been performed up to a concentration of 0.2 mg/mL and for Synomag® 70 , and BNF up to a concentration of 0.1 mg/mL. The concentration for magnetosomes is given in terms of iron content, while the concentration for Synomag® 70 and BNF is given in terms of particles. For further information, refer to Table 4.1. All samples have been filtered with a 200 nm **P**oly**t**etra**f**luoro**e**thylene (PTFE) filter (514-0068, VWR, Radnor, USA). DLS measurements are performed with a Zetasizer Nano ZS (Malvern Panalytical, Malvern, UK). The measurement procedure was started with a waiting

[3] 4-(2-hydroxyethyl)-1-piperazineethanesulfonic acid

period of 100 s to allow the sample to reach a fixed measurement temperature of 25 °C. Afterwards, five measurements with 15 sub-runs were performed. Each sub-run had a duration of 10 s. The hydrodynamic radius was then calculated via the Zetasizer software from the mean value of the number distribution and averaged over five runs. The given error is the standard deviation.

3.1.2 Electrophoretic Light Scattering

Charged particles in a colloidal dispersion form a hydration shell of ions present in the dispersion medium bound by Coulomb forces. The first layer of the dispersion medium is firmly bound to the surface layer of the dispersed particle, forming a Stern layer. Combined with a more loosely bound diffuse layer, the Stern layer builds up an **E**lectric **D**ouble **L**ayer (EDL). As a result of the dispersion medium shielding the particle's charge, the particle seems to be electrically neutral to the surroundings. If the particle is moving through the medium, the drag of the surrounding medium causes the outer part of the diffuse layer to be removed - The so-called slipping plane forms. The potential at this distance from the particle is called ζ-potential (Figure 3.2). To measure this potential, a Zetasizer is used. It uses **L**aser **D**oppler **V**elocimetry (LDV), a commonly used technique to determine the speed of particles capable of scattering light. The Zetasizer uses the **M**ixed **M**ode **M**easurement-**P**hase **A**nalysis **L**ight **S**cattering (3M-PALS), an improved measurement technique compared to standard DLS. Mixed mode refers to a mixture of **S**low **F**ield **R**eversal (SFR) and **F**ast **F**ield **R**eversal (FFR). SFR is a standard in LDV measurement devices; slow switching enables a steady flow of dispersion medium due to an effect known as electroosmosis. Electroosmosis describes the flow of a liquid due to an applied electric field. In contrast, the FFR is a rapid switching of the applied field, suppressing electroosmosis due to the inertia of the fluid. FFR gives the opportunity to determine the mean of the velocity of the particle motion caused by the applied electric field but provides a low resolution on the distribution. The distribution can be determined with SFR measurement. The distribution mean, however, is shifted by the electroosmosis. Due to the possibility of measuring under the influence of electroosmosis, the measurement position can be everywhere in the cell, which gives rise to robustness concerning the cell placement in the machine.

PALS refers to the signal processing. The frequency shift of the scattered light caused by moving particles is comparably insensitive to slow-moving particles. However, the change in phase of the compared frequencies increases steadily even for minimal wavelength differences and is, therefore, better measurable. With this setup, it is possible to measure the ζ-potential for particles in the size range of 3.8 nm to 100 µm [46].

The samples for ζ-potential measurement are prepared in the same way as described in Section 3.1.1. Five runs with 15 sub-runs for 10 s each are performed for data acquisition. The waiting time between runs was 50 s. The ζ-potential is averaged over all runs. Given as a result are the mean value and the standard deviation.

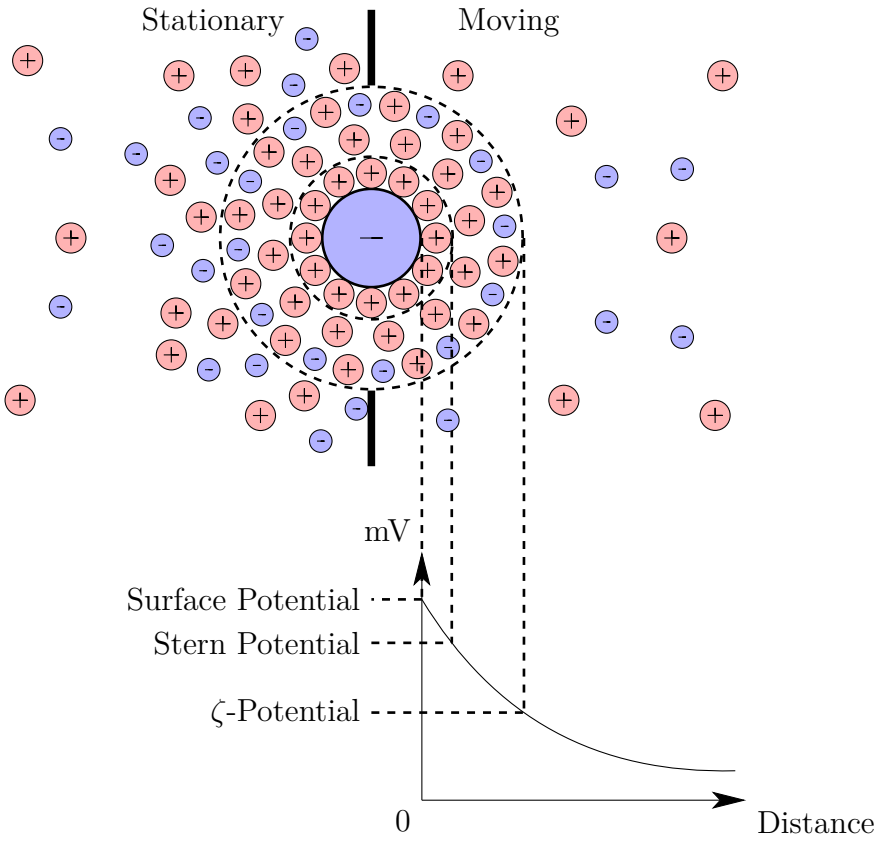

Figure 3.2: Schematic of the ζ-potential comparing the charge distribution around a charged particle while stationary and while in motion.

3.1.3 Transmission Electron Microscopy

Transmission **E**lectron **M**icroscopy (TEM) is a technique for electron microscopy that is based on accelerated electrons surpassing a thin layer of the material in question. As a result of the wave-particle duality, electrons have a wavelength associated. The de Broglie wavelength λ_{dB} which can be calculated by

$$\lambda_{\mathrm{dB}} = \frac{h}{p} = \frac{h}{\gamma m v}, \tag{3.6}$$

where h is the Planck constant, p is the particle momentum, γ is the Lorentz factor, m is the particle mass, and v is the particle velocity [48]. Due to the comparably small wavelength of electrons in contrast to light, resolutions of up to 45 pm are possible,

dependent on the acceleration voltage [49]. The acceleration voltage is the maximum potential difference of the electric acceleration field surpassed by the electrons. For the imaging in this work, acceleration voltages of below 100 kV were used. Just like light in conventional microscopy, the electrons get scattered or absorbed by the sample. Electrons that leave the sample under the same angle are focused at the same spot in the back focal plane of the TEM; therefore, it is possible to use an aperture to block all scattered electrons. Due to this approach, the areas where the electrons are scattered appear darker in the resulting image. As stated above, it is possible to image thin layers; the maximum thickness is determined by the atomic number of the atoms in the sample and the acceleration voltage. The higher/lower the atomic number/acceleration voltage, the thinner the samples need to be. In biological samples, the contained elements are typically lighter. To overcome this, staining agents are used which contain heavy metals. Due to the use of different heavy metals, it is possible to enhance the contrast of the image, even selectively, when the binding preferences of heavy metals to biological molecules are known and if they bind with different specificities at different sites.

The TEM samples are prepared in different ways for Synomag® 70 /BNF and magnetosomes. For Synomag® 70 and BNF, the stock solution is diluted in **P**hosphate-**b**uffered **s**aline (PBS) until a concentration of 0.125 mg/mL is reached. The solution is sonicated for 10 min in an ultrasonic bath (Elmasonic S 60 H, Elma, Singen, Germany) and filtered using a syringe filter (Filtropur S, membrane: Polyethersulfone, filtration area 6.2 cm, pore size 200 nm, Sarstedt AG&Co. KG, Nümbrecht Germany). From the prepared solution, 7 µL is given onto a Formvar-Ni-Grid and left to sediment for 2 min. The supernatant is removed with filter paper, and the grids are left to dry on air. The imaging process is performed with a Joel JEM-2100Plus (Akishima, Tokyo, Japan) in brightfield mode at an acceleration voltage of 80 kV. The magnetosomes are diluted 1:20. A concentration is not determined. The sample is then given onto a Carbon-Cu-Grid. The sample is left for 1 min to sediment, and the supernatant is removed with filter paper. The sample is left to dry on air. The imaging process is done with a Zeiss TEM 902 (Carl Zeiss Microscopy GmbH, Jena, Germany) at an acceleration voltage of 80 kV.

3.1.4 AC Susceptometer

As stated in Section 2.3, the susceptibility of a material is dependent on the frequency of the magnetizing field. To be able to measure the susceptibility, a Dynomag ™Susceptometer (RISE Research Institutes of Sweden, Sweden) is used. The working principle is to measure the sample's magnetization caused by an applied AMF. The

sample magnetization is determined with an excitation coil pair, where the response is measured by a pickup coil pair. To gain information about the AC-magnetization, the current generated by the magnetic field in a pickup coil with the sample inside is compared to the current generated by a magnetic field in an empty pickup coil. In reality, the two pickup coils won't be identical; therefore, the sample is measured alternating in both coils. This enables the correction for errors caused by differences of the coils. A sketch of the setup is shown in Figure 3.3.

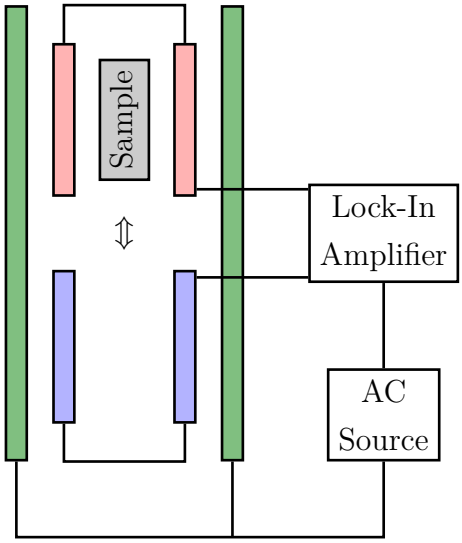

Figure 3.3: Schematic of the AC-Susceptometer setup with a pair of excitation coils (green), first pair of pickup coils (red), and second pair of pickup coils (blue).

For AC-susceptometer measurements, 200 µL of the sample solution is given into a measurement vial. For each sample, one run is performed, which consists of several individual measurements. The AC-susceptometer software gives the possibility to extract relaxation times by applying a fit to the measured susceptibility. In the scope of this work, the so-called extended multi-core model is used. The fit function is given by

$$\chi(\omega) = \chi_{0_\mathrm{B}} \int \frac{1}{(1 + \mathrm{i}\omega\tau_\mathrm{B}(r_\mathrm{H}))} f(r_\mathrm{H})\,\mathrm{d}r_\mathrm{H} + \frac{\chi_{0_\mathrm{N}}}{1 + (\mathrm{i}\omega\tau_\mathrm{N})^\alpha}, \tag{3.7}$$

with the AC Susceptibility χ, the hydrodynamic radius r_H, the angular frequency ω, the Brownian/Néel Relaxation times $\tau_{\mathrm{B/N}}$, the hydrodynamic distribution function $f(r_\mathrm{H})$, the DC susceptibility due to the Brownian/Néel relaxation $\chi_{0_{\mathrm{B/N}}}$ and the distribution degree of the single cores α. α describes a stretched relaxation covering a larger range in ω as described by the Cole-Cole model [50].

3.2 Thermal Imaging

Temperature measurements of small volumes face the challenge that the sample temperature would be influenced by a temperature probe. To overcome this, the usage of contact-free measurement techniques is favorable. One approach is to utilize the thermal radiation emitted by every object with a temperature above 0 K. While thermal radiation is visible to the naked eye for temperatures around 400 °C and above, the emission of objects at room temperature lies in the infrared spectrum. The simplest approach to measuring thermal radiation is using an infrared thermometer. This method is simple, and the needed devices are cheap. While for large and homogeneous sample surfaces, the exact measurement point and the area averaged for the measurement is secondary. For small samples which might exhibit temperature gradients, a well-defined measurement area and a spatially resolved measurement is needed. A thermal imager, also known as a thermographic camera, meets these requirements.

The working principle is based on black-body radiation. The emission spectrum of a black body is described by Planck's law, which is given by

$$L_{\mathrm{BB}}(\nu, T) = \frac{2h\nu^3}{c^2} \frac{1}{\mathrm{e}^{\frac{h\nu}{k_{\mathrm{B}}T}} - 1},$$

where L is the spectral radiance, h is the Planck constant, ν is the frequency of the electromagnetic radiation, c is the speed of light, k_{B} is the Boltzmann constant, and T is the absolute temperature of the black body [51]. A black body is an idealized concept that absorbs all incident radiation indifferent of wavelength and incidence angle [52]. According to Kirchhoff's law of thermal radiation, perfect absorbance implies "perfect" emission meaning that the emitted radiation is solely dependent on the temperature of the emitter. To adapt the concept to real objects, the emissivity ϵ is defined by

$$\epsilon(\nu, \delta, \phi, T) = \frac{L(\nu, \delta, \phi, T)}{L_{\mathrm{BB}}(\nu, T)}, \tag{3.8}$$

where $L(\lambda, \delta, \phi, T)$ is the spectral radiance of the real object [53]. As visible from Equation (3.8), the emissivity is a function of temperature T and frequency ν and the polar and azimuthal angles δ, ϕ. If ϵ is smaller than one but constant for all frequencies, the radiating body is called gray body, while other objects are called selective emitter [54]. The emittance of an object is corrected for by the evaluation software. For this purpose correction areas are used. These define the emission factor for parts of the image and need to be set manually. Due to the absence of perfect black bodies, and more importantly due to the fact that even if perfect black bodies exist, most objects

in question of thermal imaging are no black bodies, the radiation "emitted" from a surface is a mixture of actually emitted, reflected, and transmitted radiation.

While the most decisive factor influencing an object's emittance is its material, the surface structure and the viewing angle also influence the effective emissivity of an object, similar to the interaction with visible light [54]. Today to adapt the imaging process and the evaluation towards the spectral properties of certain materials (e.g. glass) in a way that measurements of the surface as well as of secondary objects behind the first material are possible under certain preconditions [55]. The samples used in this work are dispersed or submersed in water to mimic the normal environment inside a cell. Therefore, the transmitted part of the radiation can be neglected due to the absorbance of **I**nfra**r**ed radiation (IR radiation) in water [54]. Consequently, the measured radiation is a mixture of emitted and reflected radiation originating from the sample's surface. The influence of the reflected radiation is compensated for by the evaluation software by taking the so-called reflected temperature into account. This temperature is in good approximation for inside measurements given by the room temperature. A major benefit of thermal imaging is the ease with which it is possible to monitor the temperature of a large area. To enable the possibility for a fast first impression of thermal data, the use of false color images is common, where the temperature is correlated to the image defined by a color bar. This technique, however, also poses the risk of false interpretation since the appearance is strongly dependent on the used color bar and the limits chosen. Due to the rather large temperature changes in this work, the color map range is chosen to cover the temperature range of the image in question. Therefore, it is of utmost importance to check the color bar for each image.

On the technical side, the detection of thermal radiation is in the case of the used VarioCAM HD (Infratec, Dresden, Germany) realized with microbolometers. These detectors measure the electric resistance of a resistor that is heated by incident thermal radiation. To be able to determine the temperature, the heat capacitance, the initial temperature, and the thermal connection to its surroundings need to be known. This approach does not need any cooling at room temperature, although it is at risk of a slow drift in measured temperature as the temperature of the thermal imager itself can drift. This drift, however, is corrected by the camera periodically. Due to the indirect measurement of IR radiation, the microbolometer is also limited in terms of frame rates as the temperature rise in the detector element is not instantaneous. The used camera has a detector size of 640×480 pixels with an instantaneous field of view of 0.8 mrad and a total field of view angle of $30° \times 23°$. In combination with the camera magnet distance of 40 cm, this gives a resolution of 300 µm per pixel. The object of interest must be larger than this to be correctly measured. If the object is smaller,

the corresponding pixel will display a temperature which is a mixture of the targeted object and the surroundings, which are imaged onto the same pixel.

The samples for thermography imaging are diluted to the concentration given for the corresponding measurement. A cuvette (Semi-micro cuvette, 67.742, Sarstaed AG&Co. KG, Nümbrecht, Germany) is filled with 200 µL of the sample. The measurement process is described in Section 4.3.

4 Experimental Setup and Results

The aim of this project is to develop an efficient multi-purpose magnetic hyperthermia setup and to characterize it concerning the electromagnetic properties and the resulting heating capacity. The latter is done by probing the system with three different MNPs. In the following, the experimental results will be discussed. At first, the developed hyperthermia setup will be introduced; afterwards, the used magnetic MNPs will be characterized. The physical core size and structure of the MNPs are determined via transmission-electron-microscope images. The hydrodynamic radius is determined via dynamic-light-scattering measurements. Further, the ζ potential has been determined by Zetasizer measurements. For magnetic heating, the before-mentioned alternating-current-susceptibility Section 2.3 is an important factor and has been examined utilizing an AC-suceptometer. Afterwards, the heating behavior of the particle systems is compared and evaluated with the formulas introduced in Section 2.4. The parameters extracted from this model will be discussed, regarding the usability for magnetic hyperthermia, showing that the proposed setup enables well-controlled hyperthermia measurements up to equilibrium temperatures.

4.1 Experimental Realization of an AMF Setup

In this section, the development of the experimental setup used for the hyperthermia measurements will be discussed in terms of the requirements and characterization parameters. The goal for this setup was to generate a magnetic field with a flux density of 40 to 50 mT at around 100 kHz. The operation time of the setup shall be long enough to reach equilibrium between the supplied energy by hyperthermic heating and dissipated energy. In order to achieve these goals, special attention was paid to the setup design and challenges arising from underlying physical phenomena which are specific to the given use-case of high-frequency electromagnetic apparatuses. Also, the requirements are discussed with respect to their influences on the design of the setup.

4.1.1 Basic Principle

The basic principle of the setup is a resonant transformer with a cored electromagnet. The setup is based on [56], which was refined in the here reported study. In the following, the reasoning for the setup will be given to enable the understanding of the chosen setup, also following [56]. There are different construction options to achieve a magnetic flux density of ∼45 mT at the sample position. The easiest construction-wise is a coil wound around the sample. The magnetic field strength inside a coil, where the length is much larger than the diameter, can be calculated by

$$\vec{B} = \mu_0 \mu_\mathrm{r} \frac{I \cdot N}{L} \cdot \vec{e}_\mathrm{z}. \tag{4.1}$$

With the magnetic field constant $\mu_0 \approx 4\pi \cdot 10^{-7}\mathrm{N} \cdot \mathrm{A}^{-2}$, the material constant of the core material μ_r, the amount of windings N, the current running through the coil I, and the length of the coil L. This setup, however, has to fulfill several constraints, the first being the particular size and position of the coil. Due to the planned observation via thermal imaging, the symmetry axis of the coil needs to be aligned with the optical axis of the setup. Otherwise, the coil would block the view of the sample. To generate a homogeneous field at the sample position, the coil must be longer along the optical axis than the sample. Another method to generate a homogeneous field is using a Helmholtz coil. While this method generates a homogeneous field around the central axis of the coil pairs, it would require an even larger setup. This is due to the requirement that the radius of the coils is equal to the distance of the coils. The magnetic field inside the Helmholtz coil can be calculated using

$$\vec{B} = \frac{8}{\sqrt{125}} \mu_0 \mu_\mathrm{r} \frac{I \cdot N}{R} \cdot \vec{e}_\mathrm{z}, \tag{4.2}$$

with R being the radius of the coils. By comparison of Equation (4.1) and Equation (4.2), it is clear that the generation of the same flux density at the coil center (and otherwise identical parameters) would require a ~ 1.4 times higher current.

Another method often used with electromagnets is the use of a core. As stated in Equation (4.1), the magnetic flux density depends on the core material and its relative permeability μ_r. While μ_r is ~ 1 for air, it can reach much higher values in matter (Section 2.2.1). Thus, the magnetic flux is substantially increased by the core. To be able to place the sample in the magnetic field, the simplest method is to use a toroidal core with a gap in the dimension of the sample. If the gap is small compared to the

overall length of the toroid, the magnetic field can be approximated using

$$B \approx \frac{N \cdot I}{w}, \tag{4.3}$$

where N is the number of turns, I is the current running through the coil, and w is the gap width. As stated before, an air coil must be larger than the sample to generate a reasonably homogeneous field distribution. In contrast, the gap in the magnet core needs to be only marginally larger than the sample. By comparing formulas 4.1 and 4.3, it is visible that for $w < L$, the magnetic field inside the gap is larger than in the air coil. As efficient setups are desirable, the building type used is a toroidal electromagnet with a gap.

For the generation of the AC-current, a resonant transformer is used as done before [57]. A resonant transformer is the combination of a transformer and a resonant circuit on the secondary side of the transformer. Therefore, the current for generating the AMF is limited by the impedance of the secondary side components. In the case of a resonant transformer, the secondary side forms a resonant RLC circuit[4] constituted by a capacitor C and an inductor L. In the case of the combination of a resonant circuit and a transformer, the total inductance is a combination of the magnet inductance and the inductance of the transformer. The resistor R is normally not a component used in the circuit but appears as the effective internal resistance of the capacitor, inductor, and the used wire and connections.

A reactance is an electrical component that stores energy rather than dissipating it as heat. These types of components are capacitors and inductors. By combining an inductive reactance, and a capacitive reactance, a resonance circuit is formed (Appendix A.1). The resulting circuit diagram of the used resonant transformer can be seen in Figure 4.1.

As with every resonant system, an RLC circuit does possess a resonance frequency. If the excitation frequency matches the resonance frequency, the impedances of the reactances cancel each other out. In this case, the current running through the system is only limited by the real part of the impedance, namely the ohmic resistance of the used components. The needed capacitance to achieve the wanted working frequency for a given inductance can be calculated utilizing the formula for the resonance frequency

$$f_\mathrm{r} = \frac{1}{2\pi}\sqrt{\frac{1}{LC} - \frac{R^2}{2L^2}} \tag{4.4}$$

[4] R:Resistor, C:Capacitor, L:Inductor While R and C seem to be obvious choices of abbreviations L is not quite intuitive. It was chosen in honor of Heinrich Friedrich Emil Lenz [58].

(Appendix A.1), where R, L, and C are the resulting resistance, inductance, and capacitance of all components in the setup.

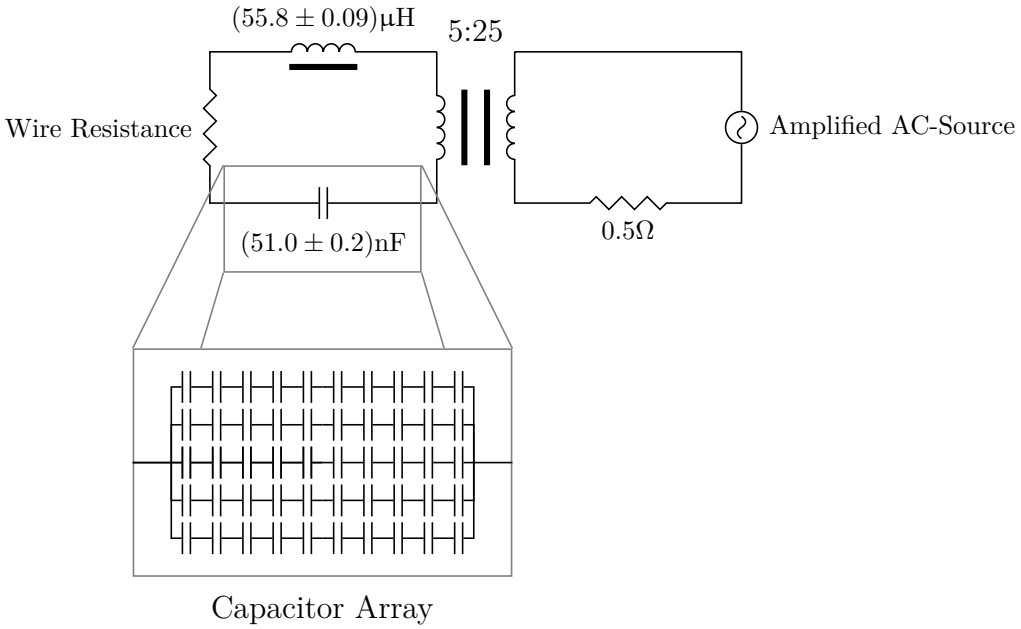

Figure 4.1: Schematic of the used electrical setup with the RLC circuit on the left-hand side with indicated R, L, and C coupled to an amplified AC-source by a 5:25 transformer. The actual composition of the capacitor is shown in the zoom box "Capacitor Array".

The use of this system also has a safety aspect. The power that needs to be supplied to the circuit is small compared to the power stored in the circuit. Thus, the danger posed by the power source in the case of a malfunctioning is reduced compared to a high-power source. The source signal is firstly generated by a function generator (Agilent 33220A, Agilent Technologies, Santa Clara CA, USA) and afterwards amplified by (53.0 ± 1.5) dB using a radio frequency power amplifier (1020L, Electronics and Innovations LTD., Rochester NY, USA).

4.1.2 Ferrite Core

The key component of the AMF generation is the electromagnet, which is constituted of a toroidal core and a wire wound around it. The core greatly increases the magnetic flux density following Equation (2.12). A common material for the use as magnet cores is soft iron, which, while well suited for **D**irected **C**urrent(DC) applications, it is not readily suitable for high frequency AC applications. The main problem are eddy-currents which are a direct consequence of Equation (2.3). Eddy-currents are

circular currents around temporally changing magnetic fields in conducting materials, like iron, due to the arising electric fields. These currents cause Joule heating of the core. An engineering method to reduce the loss is to use a layered core which increases the resistance and therefore reduces the power loss.

A different approach using the same effect is to increase the resistance by changing the core material. In the frequency range of 100 kHz, ferrites are the best choice [57]. In the scope of this project, three different suitable toroidal cores have been investigated. While other core geometries may be more suitable for the application [57], toroidal cores are readily available and cost-efficient. As a simple method of comparing ferrite cores, the coupling factor of a transformer has been chosen. This method provides the opportunity to compare the cores without the need to cut a gap into the core to measure the generated field. As a measure of the core performance, the coupling factor k is chosen. It quantifies the amount of flux coupled from the primary coil into the secondary coil. It can be calculated using

$$k = \sqrt{1 - \frac{L_{\mathrm{sc}}}{L_{\mathrm{oc}}}}$$

with L_{sc} the short-circuit inductance and L_{oc} the open-circuit inductance. A short-circuited secondary side represents the maximum load possible, while an open secondary side yields no load (Appendix A.1).

The effect of the core on the coupling frequency was determined in detail. The results for different cores with a winding ratio of 25:5 and a stranded wire are shown in Figure 4.2. It is visible that the coupling factors differ significantly. The maximum deviation is about 0.8 % of the transferred magnetic flux. Since the energy of the magnetic field energy is quadratically dependent on the flux density, this leads to an energy loss during the transfer of about 1.6 %. The derivation of the coupling coefficient for the different directions is deemed to be caused by the different form factors of the coils. While for the 25-winding coil, the toroidal shape is followed by the winding, thus aiding the coupling to the core, the five-winding coil is comparably straight. This effect decreases as the coupling gets better.

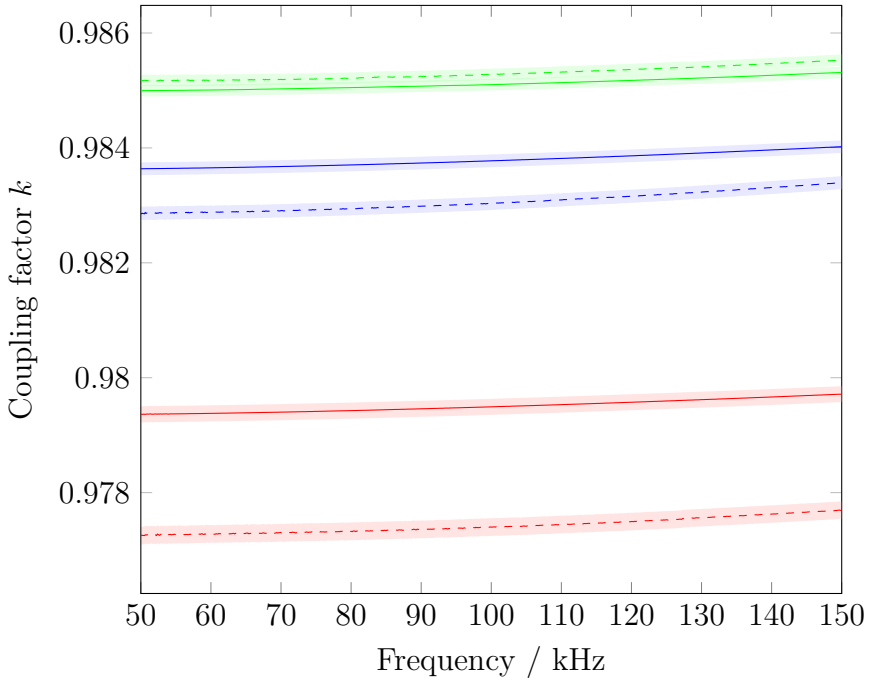

Figure 4.2: Coupling factor k of a transformer with 25:5 windings for different ferrite cores. N87 (green), 3F3 (red), and 3C90 (blue). The winding ratio is 25:5 for solid lines and 5:25 for dashed lines. The shaded areas represent the measurement error.

A good coupling factor also indicates low energy loss. Due to the same wire used in all measurements, the difference in loss is, except for a small deviation due to manual winding, only caused by the cores.

As a result of the N87 core having the best coupling factor, it was used as a magnet and transformer core.

4.1.3 Litz wire

While the reduction of dissipated power can be achieved for low frequencies by simply increasing the cross-sectional area of the used conductor, this hold not true for high frequencies. This is the case since the current flowing through the conductor is confined to the outer layer by the frequency-dependent skin effect. It originates from the limited penetration depth δ of the electric fields causing the current flow, which can be calculated using

$$\delta = \sqrt{\frac{2}{\omega \mu_\mathrm{r} \mu_0 \sigma}},$$

with the vacuum permeability μ_0, the relative permeability μ_r, the conductivity σ and the angular frequency of the electric field ω [59, p.137]. Due to the confinement to the outer part of the conductor, the inner part of the conductor does not contribute greatly to the conductivity. As a result, the material below the penetration depth can be removed either by using a tube or by decreasing the wire diameter.

The most used conductor in cable production is copper. Figure 4.3 illustrates the penetration depth of copper. For a frequency of 100 kHz it is ∼212 µm, which leads to a usable diameter of ∼424 µm for a copper conductor. While the conductivity of a wire adjusted for the penetration depth is not limited by the skin effect, it is limited by the size of the conductor itself. The DC resistance of a skin effect adjusted cable with a cross-sectional area of 0.14 mm^2 wire is 0.099 Ω/m compared to the 0.011 Ω/m of a standard 1.5 mm^2 installation cable. This shows that even if the wire is adapted to the skin effect, its resistance is increased solely due to the reduced diameter.

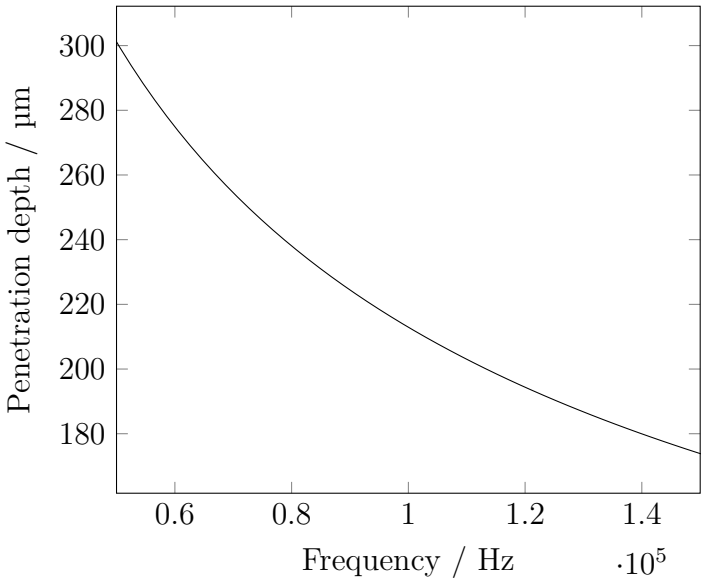

Figure 4.3: Calculated penetration depth of electric fields into a copper conductor. The resistivity of copper is 0.0179 Ω mm^2/m [60]. The unit Ωmm^2/m is chosen to emphasize that for the calculation of the resistance, it is not sufficient to divide by the length of the cable but rather to divide by the cross-sectional area and multiply with the length of the cable.

To increase the conductivity, multiple individually insulated wires are combined as in stranded wire, which gives rise to the proximity effect. If a temporal changing current flows through a conductor, it forms a temporal changing magnetic field around said conductor. If other conductors are placed around the first conductor, this alternating magnetic field causes temporally changing electric fields in the surrounding conductors, which alters the current distribution asymmetrically. If the observed conductor is not

surrounded symmetrically by other conductors, as is the case at the border of wires, this causes a smaller effective area of the conductor; hence the effective resistance increases.

In the scope of this project, two different cables have been investigated for their usability as windings of the electromagnet. The first wire tested is a stranded wire with 510 individual copper strands with a diameter of (0.050 ± 0.005) mm. These strands are not individually insulated and are parallel oriented (Figure 4.4).

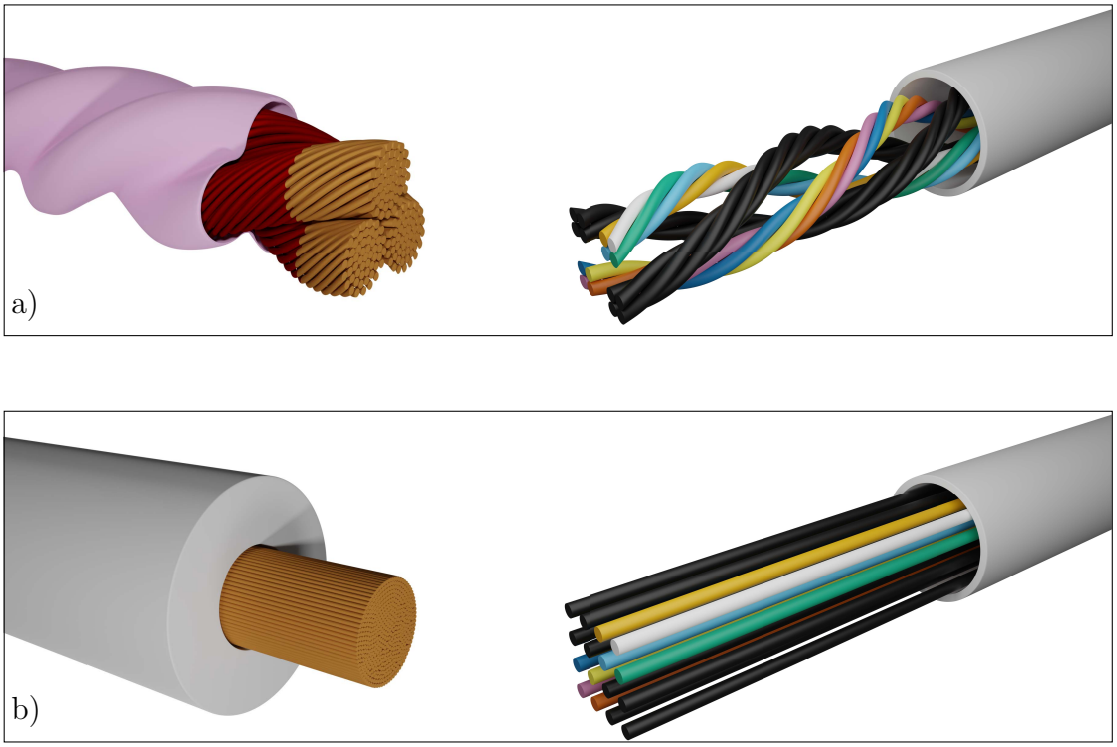

Figure 4.4: Rendered images of the wire composition on the left side. Schematics illustration with a reduced strand count of the wire alignment inside the different wire types. a) Left side: rendered image of the Litz wire as used in the setup showing the three strands of 54 individually insulated wires. The individual insulation is depicted in burgundy; the outer insulation is depicted in pink. Right side: schematic illustration of the winding used in the Litz wire. b) Left side: rendered image of the stranded wire as used in the setup showing 510 wires. The outer insulation is depicted in white. Right side: schematic of the wire alignment in the stranded wire.

Due to the splitting of a solid wire into separate smaller wires without insulation, the calculation for the penetration depth is no longer correct. The reason is that the contact resistance is not infinite; therefore, the current is not confined to the individual wires. The second cable tested is a specially designed Litz wire, which is optimized for a frequency range from 50 kHz to 100 kHz [61]. The wire is made up of three strands of 54 individually insulated **A**merican **W**ire **G**auge(AWG) 38 wires. The diameter of

AWG 38 wires is 0.1007 mm, which is well below the penetration depth. The internal composition of Litz wire is different from the stranded wire as the wires are individually insulated and are wound around each other. Three strands are then combined into the final wire.

For both cables, the impedance has been measured with an E44990A impedance analyzer (Keysight Technologies Inc., Santa Rosa, CA, USA). For all impedance measurements, the 4-point probe method in the range of 50 kHz to 150 kHz is used. Since the impedance of a cable strongly depends on the cable positioning, the cables are positioned on a circle jig with a diameter of 1 m for the measurement. This way, the cable can be measured in a fixed, restorable position. The resulting data is shown in Figure 4.5 and Figure 4.6.

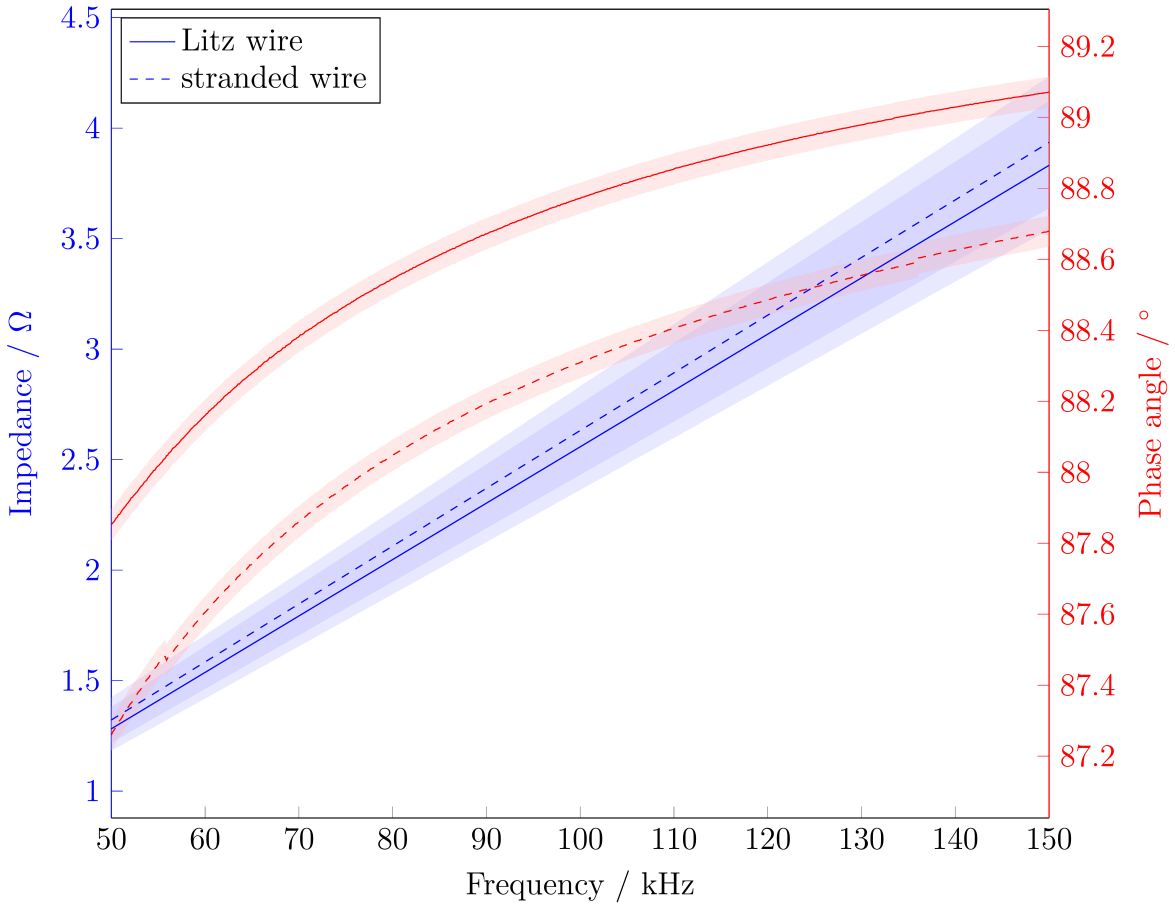

Figure 4.5: Absolute value of the impedance and phase angle of stranded and Litz wires. The errors are depicted as shaded areas around the measurement values.

In Figure 4.5, the absolute impedance and the phase angle are shown. As expected, the impedance increases with the frequency. The increase in phase angle indicates that the inductance increases faster than the ohmic resistance. Although the circular arrangement does increase the measured inductivity, it should not influence the

ohmic resistance of the cable. When interpreting the data, it needs to be considered that the measurement was done with low currents compared to the ones in the AMF-Setup, which will lead to increased heating of the wire and thus alter the overall impedance. This being said, the relative comparison of resistivity gives an estimate of the performance at higher loads, as the wire with higher resistivity will lead to a more pronounced temperature rise, which in turn will increase the resistivity. The result of the impedance measurement is shown in Figure 4.5 where no significant difference in absolute impedance is measurable between the stranded wire and the Litz wire. As expected, both wires show clear inductive behavior. Figure 4.6 shows the real part of the impedance for the different wires. For 100 kHz, an increase of $\sim 30\,\%$ is visible for the stranded wire. Thus the dissipated power would differ by the same amount. Although the measurement values are compatible with the errors, the Litz wire is chosen due to the lower absolute value of the ohmic resistance.

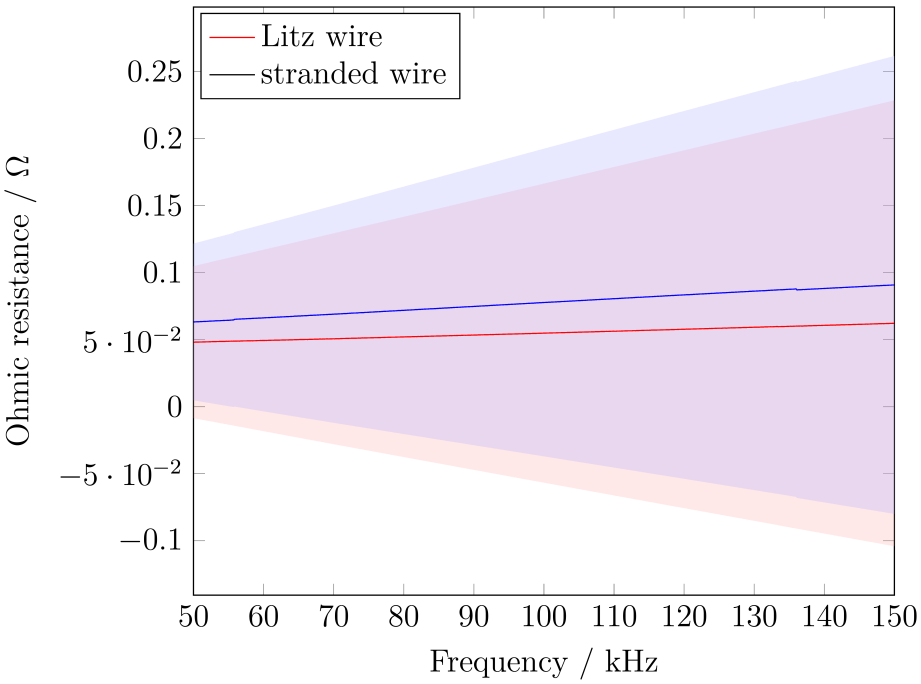

Figure 4.6: Real part of the wire impedance representing the ohmic resistance. The errors are depicted as shaded areas around the measurement values.

4.1.4 Magnet

The magnet used to generate the AMF is built from an N87 ferrite core and 21 turns of Litz wire. In this chapter, only the electromagnetic properties of the magnet, in the context of the resonance circuit, are discussed. The cooling properties are discussed in section 4.1.7, and the magnetic field generated is discussed in section 4.1.9. The core is equipped with cooling, which will be introduced in Section 4.1.7. The individual properties of the core and the wire are discussed in Section 4.1.2 and Section 4.1.3, respectively. In this chapter, the reactive behavior of the magnet is discussed. The impedance measurement[5] of the magnet is given in Figure 4.7. The measurement shows an inductance of $(59.45 \pm 0.31)\,\mu H$.

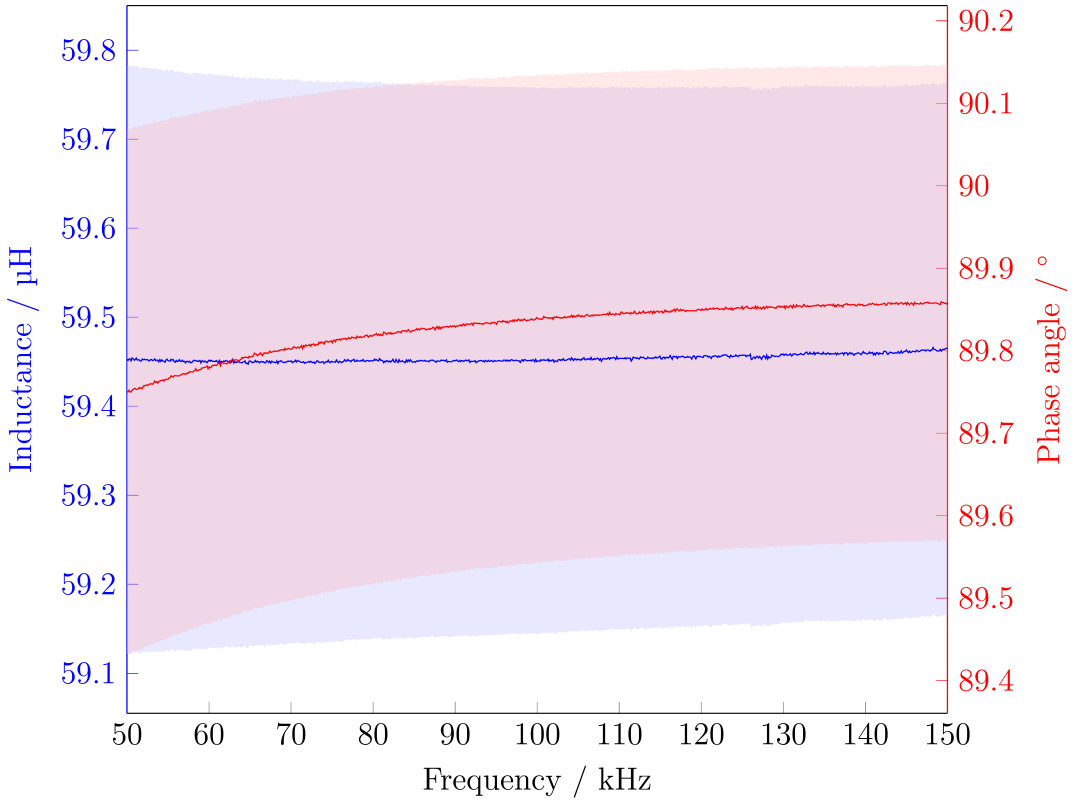

Figure 4.7: Inductance and phase angle for the magnet with an N87 ferrite core and Litz wire windings. The errors are depicted as shaded areas around the measurement values.

Phase angle and inductance are shown to be nearly constant over the whole frequency range (Figure 4.7). Since the imaginary part of the impedance is proportional to the frequency, the constancy of the phase angle indicates that the Ohmic resistance also increases linearly. This coincides with the linear increase of the wire resistance as

[5]The impedance measurements are performed with the same instrument and parameters as the ones described in Section 4.1.3.

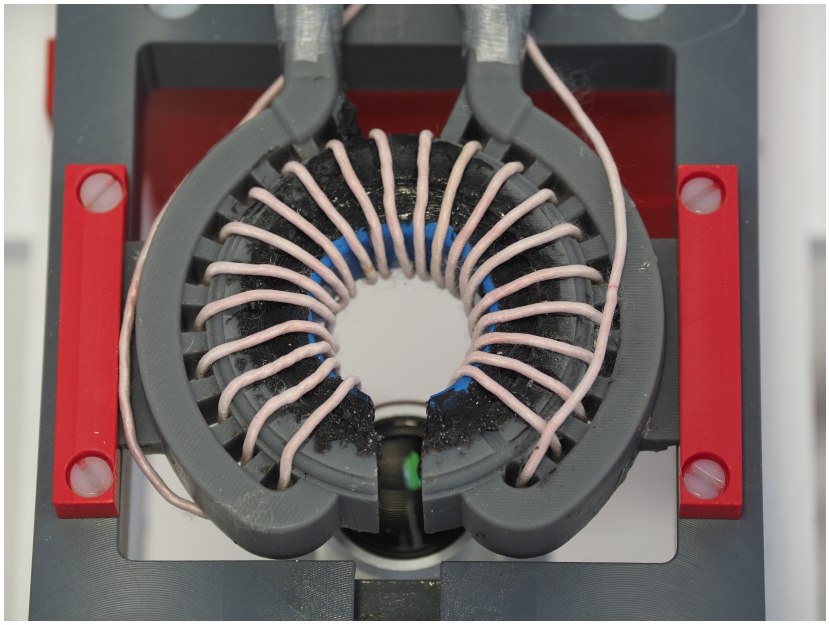

Figure 4.8: Photographic image of the designed magnet assembly. The blue-coated core is visible in the middle, mostly covered by black high-temperature silicone used to establish the seal between the core and light gray cooling case. The used wire is a Litz wire with fabric insulation in pink.

discussed in Section 4.1.3. The finished electromagnet assembly, as used during the measurements, can be seen in Figure 4.8.

4.1.5 Capacitor

The counterpart of the electromagnet is the capacitor. Just as for the other components, the high frequency combined with the high current set special requirements for the capacitors. While capacitors can withstand voltages within the kV regime in DC, this value drops for AC voltages. While there are capacitors that can withstand the required load, they are comparably expensive and rare. An easier method to achieve the required performance is to use a capacitor array. But even with a capacitor array, the use of **R**adio **F**requency (RF) capacitors is difficult since most available RF-capacitors are **S**urface **M**ountable **D**evices (SMDs). The integration of SMDs into this wire-based circuits is complicated. This is due to the high current, which circuit boards are not necessarily designed for. The production of a specialized circuit board would be time-consuming and resource intensive.
The next problem would be the connection of the circuit board and transfer wires. The normal method for connecting wires to a circuit board is the use of connectors. While this is convenient in terms of serviceability, and there are connector systems fit for the purpose, these are rare, expensive, and often require special tools to be assem-

bled. As an alternative to SMD capacitors, film capacitors are chosen for the setup. These are comparably cheap, and while designed to be soldered onto circuit boards, it is also possible to connect them with wire. This is done by soldering wire directly to the connection rods. The used capacitors are FKP1 0.1 µF (WIMA, Mannheim, Germany) and are rated at 6 kV for DC currents. As mentioned before, this does drop for a higher frequency, in this case to 130 V and 8 A for 100 kHz [62]. In an array of 5×10 capacitors the overall achievable voltage is $I_{\mathrm{RMS}} = 1300\,\mathrm{kV}$ and a current of $A_{\mathrm{RMS}} = 40\,\mathrm{A}$, where RMS indicates the **R**oot **M**ean **S**quare value. This translates to **P**eak to **P**eak (PP) values of $U_{\mathrm{PP}} = 1838\,\mathrm{V}$ and $I_{\mathrm{PP}} = 57\,\mathrm{A}$. The increased number of capacitors in an array and the larger dimensions of the capacitors compared to SMDs also enables more efficient heat dissipation. Figure 4.9 shows a photo of the finished capacitance array inside the setup. Visible are the 50 capacitors (red blocks) connected by stranded wires. Here, the use of stranded wire is reasonable as the current is split between the branches of the capacitor, and the minor advantage of the Litz wire is not justifiable by the increased effort in terms of price and processing.

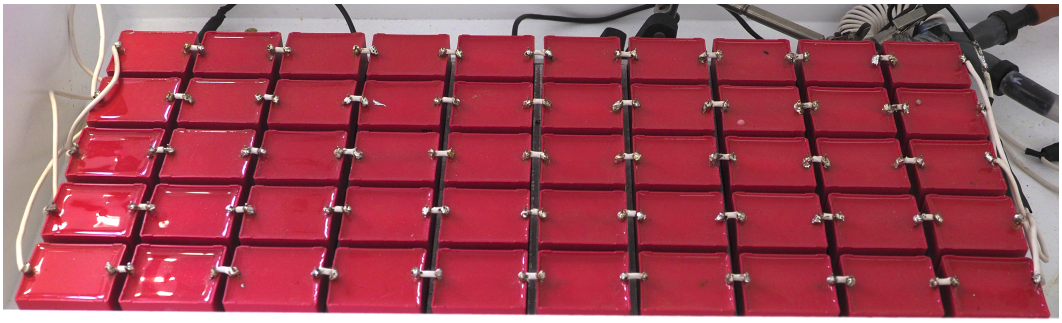

Figure 4.9: Photographic image of the capacitance array. Visible are the capacitors in red and the connections made up of small sections of stranded wire. The size of a single capacitor is 41.5 mm × 35 mm × 50 mm (l × w × h).

Figure 4.10 shows the capacitance and the phase angle as a function of the frequency. The capacitance array shows a capacitance of $(51.2 \pm 0.3)\,\mathrm{nF}$ at a frequency of 100 kHz. The frequency dependence for the measured interval is about 3.2 %. The increase in capacitance, in combination with the slight decrease in the absolute value of the phase angle, indicates that the Ohmic resistance increases with increasing frequency. This is in line with the observed change in the resistance of the used cables.

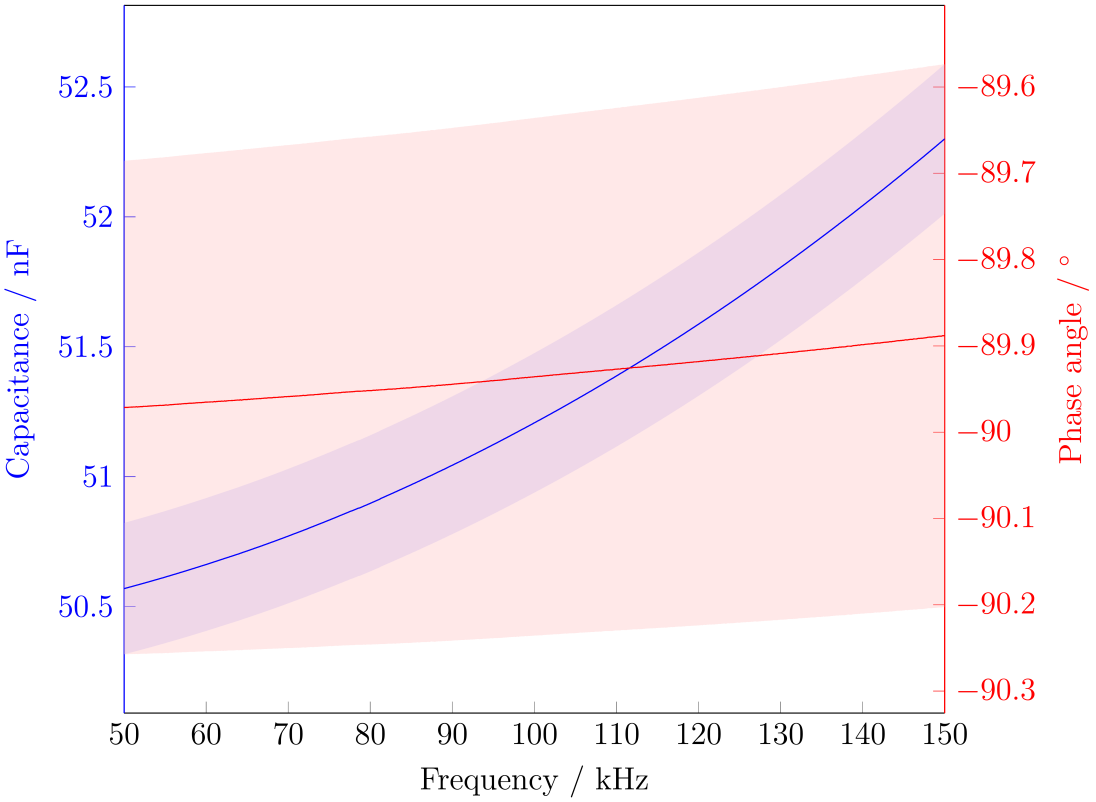

Figure 4.10: Capacitance and phase angle for the capacitance array. For the impedance measurement, the 4-point probe method in the range of 50 kHz to 150 kHz is used. The errors are shown as shaded areas.

4.1.6 Transformer

The primary and secondary parts of the circuit are coupled by a transformer with an N87 core and a winding ratio of 5:1. This serves the purpose of enabling the resonance in the secondary side of the circuit. If the magnet and the capacitor were connected directly to a power supply, the maximum current in the resonant circuit would be limited by the maximum current the power supply can withstand. The winding ratio has the purpose of increasing the maximum possible current in the secondary side of the circuit. It is counterintuitive to lower the voltage applied to a resistor to increase the possible current. This approach is due to the limited power supplied by the power source. The used amplifier is capable of supplying 200 W if the output voltage is 10 V. This means the maximum current running through the circuit is 20 A, but in the case of a load resistance of 0.03 Ω, the current running at a voltage of 10 V would be ∼333 A. The power dissipated in the resistor would then be ∼3.3 kW, which would shut off the power supply. If the voltage, however, is reduced by a transformer to one-fifth of its original value, the current is also fifths. Therefore the power dissipated by a 0.03 Ω resistor would be ∼133 W at 2 V and ∼66 A.

As discussed in Section 4.1.2, the best coupling factor can be reached by utilizing an N87 core. In Section 4.1.3, it is shown that the Litz wire has a lower resistivity compared to the stranded wire. Therefore the question arises if using a different wire would increase the coupling further. Figure 4.11 shows the measured coupling factor for Litz and stranded wire. For each wire combination, there are 25 windings on the primary side and five on the secondary side. These numbers are a result of the maximum possible amount of windings fitting on the core without turn overlapping.

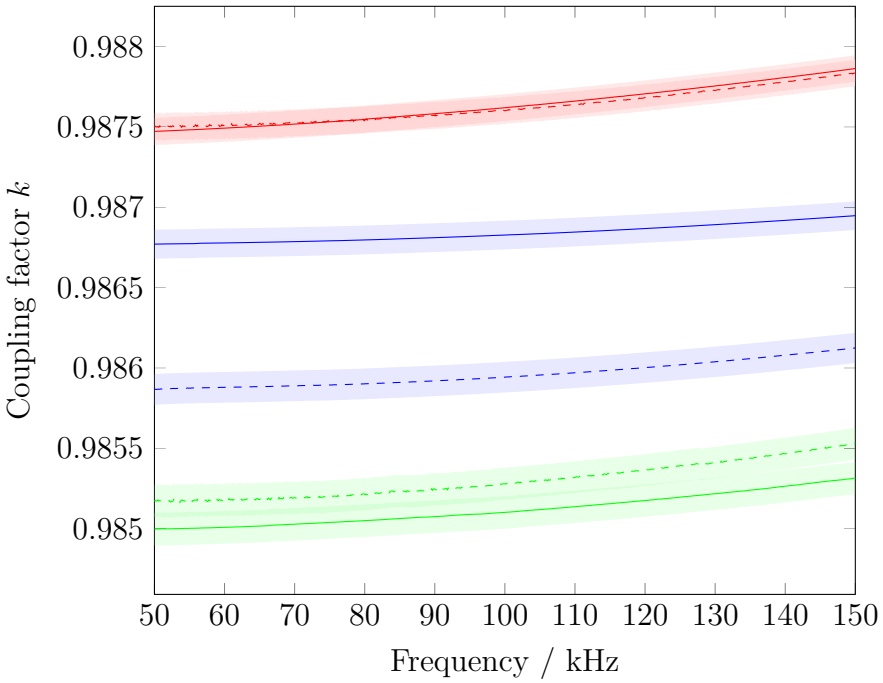

Figure 4.11: Coupling factor comparison for a transformer with an N87 core in combination with different wires. The winding ratio is 25:5 for solid lines and 5:25 for dashed lines. The colors represent the usage of Litz wire(red), stranded wire (green), and a mixture of 5 windings of Litz wire and 25 windings of control wire (blue).

As visible, the use of Litz wire increases the coupling factor. While all coupling factors are well above 98 %, the differences in coupling efficiency for the wires is attributed to the different construction types of the cables, where the Litz wire, which is, as mentioned, optimized for the use with alternating currents in the frequency regime of 50 kHz to 100 kHz is better suited for electrical field caused by the alternating magnetic flux inside the core to establish electric currents inside the conductor. As discussed in Section 4.1.2, there are differences of the coupling factor dependent on the direction of measurement (winding ratios of 25:5 and 5:25). In this measurement the differences are increased by the frequency adaption of the used cable on the secondary side, indicating less efficient coupling to stranded wire.

Due to the overall good performance in terms of coupling factor, the mixture of 5 windings Litz wire and 25 windings stranded wire is chosen. With this combination, the Litz wire is used in the secondary high-current part of the resonant circuit, and stranded wire, which is cheaper, is used in the primary part. Thus the cost of the circuit is kept low while maintaining a high coupling factor.

4.1.7 Cooling System

In the system, heat is generated by all components but in different amounts. All the previously discussed components have been tested for efficiency in reducing dissipated heat. Nevertheless, an efficient cooling system is needed. While for the capacitors, there is no measurable heat increase, the shunt resistor, the magnet, the transformer, and the cables are heating up. In the case of the transformer and the magnet, the heating seems to be caused by the cables in a non-negligible amount, as they exhibit the highest temperatures.

The simplest way for cooling would be a fan. This method, while simple, is not applicable to the present system because the airflow inside the safety box would affect the sample temperature. In previous work, a water-filled hose has been proposed as a cooling system [56]. The usage of tubes, however, introduces an insulating material between the cooling water and the core. To overcome this problem, a novel approach for cooling lines has been tested. To enable the best possible heat transfer between core and water, 3D-printed cooling shells have been developed which enable the direct[6] contact between core material and water. The direct cooling of the wires is not possible since the cable is not waterproof. This poses the problem that the wire needs to be wound around the cooling since the inclusion of the cooling into the magnet coil reduces the effective permeability due to the lowered percentage of the coil being filled with the ferrite core. To minimize this effect, the cooling needs to be compact in size while still enabling sufficient flow rates to effectively cool the magnet core. To fulfill these requirements, a cooling shell covering the outside of the magnet has been developed. Additionally to the cooling, it also introduces a guiding system for the winding to be more uniform. The CAD design is shown in Figure 4.12.

[6] Direct means that the core is only separated from the water by a thin («1 mm) coating which is on the core in delivery condition.

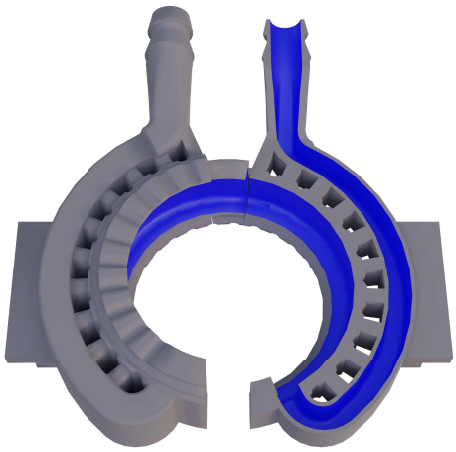

Figure 4.12: 3D CAD model of the cooling cases. The right side of the schematic has a cross-section of the case showing the water channels, which are indicated in blue. The gap width is 1 cm.

A two-part construction is needed since the integration of the magnetic core is not possible during the production process of the cooling shells. While the basic idea is simple, the main problem is establishing a watertight connection between the cooling shells and the core. The obvious choice is a sealant. The limited space around the sample, in combination with the space needed for the magnet winding, makes establishing a form-fit impossible. Therefore the sealant also needs to fulfill the requirement of a material bond. While the obvious choice of glue as a sealant connector combination seems straightforward, the implementation of this idea poses some difficulties. Here, the permanent contact with water and the temperature value and gradients reached in different parts of the magnets are to be mentioned as the supposedly main problems. The first tested material was a two-component adhesive which proved to be not suitable, as the seal was difficult to establish and also was not permanently watertight. The second tested material was high-temperature silicone (UHU GmbH, Bühl, Germany), establishing a permanently water-tight bond. A thermographic image taken during the operation of the magnet can be seen in Figure 4.13.

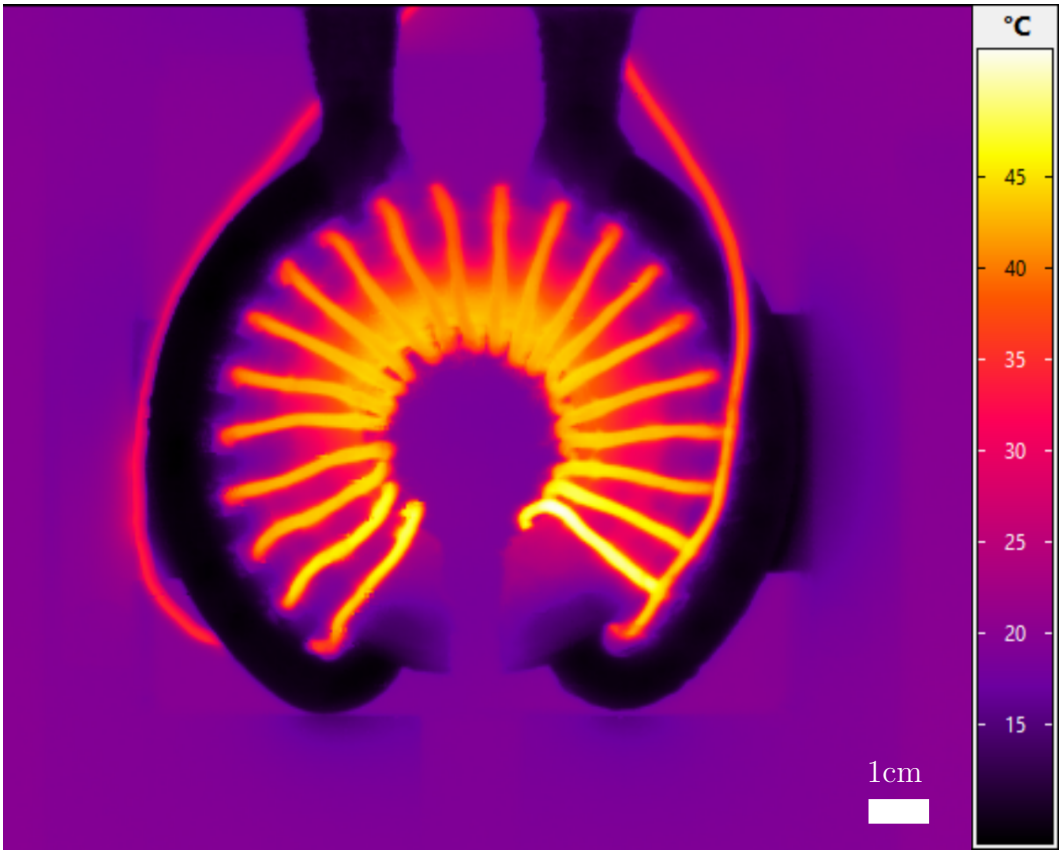

Figure 4.13: Exemplary thermographic image of the magnet after heating for 15 min. Visible are the heated wires in bright yellow. The cooling feed lines are depicted in black. In between the wires, the core is visible in orange, and the cooling is visible in purple. Around the setup, the magnet holder can be seen schematically. The poor visibility of the holder is caused by the small temperature difference between the holder and the background. Visible are the areas where the spatial proximity of the holder and cooling lines lower the temperatures of the holder. Please note that the emissivity of the image is at $\epsilon = 1$. An image covering correction of the emissivity is not possible, as the emissivity is dependent on multiple factors which are unknown for wide ranges of the image.

The resulting magnet cooling system limits the temperature to $\sim$1 °C above room temperature as shown in Figure 4.14b.

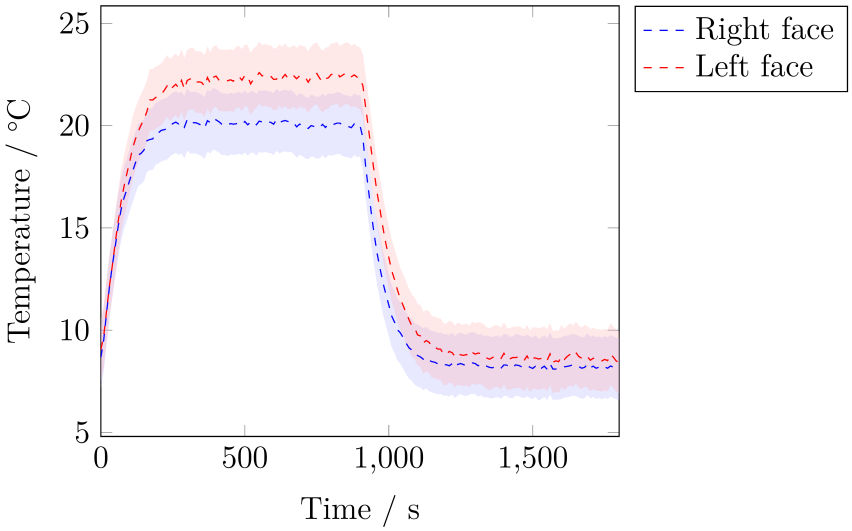

(a) Temperature of the magnet at both magnet faces next to the sample. While the measured values are seemingly compatible with their respective errors, this is not the case since the depicted errors are the errors for the absolute temperature. The error for relative deviation in one image is in the mK regime (too small to be depicted). The relative difference in temperature is attributed to the different distances of the measured areas to the last winding of the coil (Figure 4.13).

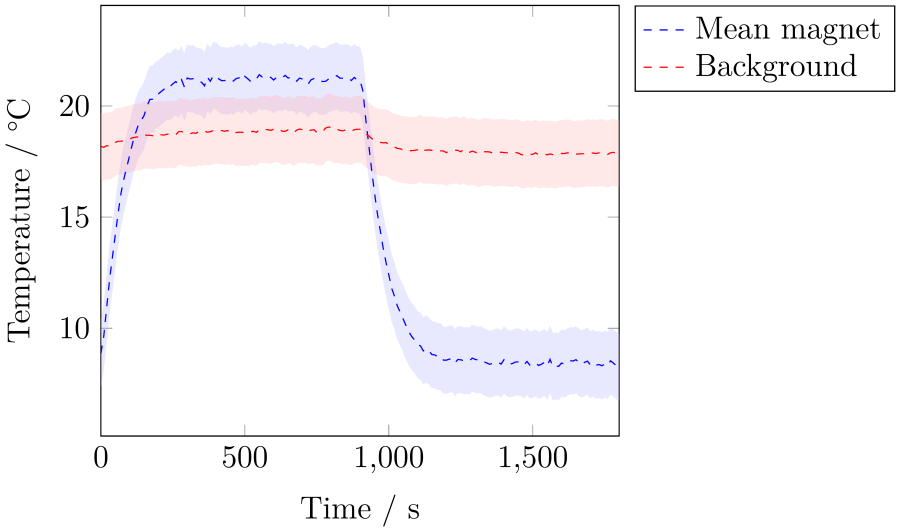

(b) Mean temperature of the magnet faces compared to the background temperature measured on the bottom of the safety box. The slight deviation in background temperature is caused by the diffuse reflection of the heated magnet.

Figure 4.14: Measurements for comparing the magnet temperature to the environmental temperature of the measurement room, and for comparing the magnet face temperatures. The temperature is measured from the top with the thermal imager.

Although the cooling limits the maximum temperature of the magnet, it does not keep the temperature temporally constant. As visible in Figure 4.13, the holder of

the magnet gets colder in the direct vicinity of the cooling lines. This behavior is also expected to be visible for the sample in the gap, meaning that the temperature of the sample is influenced by the temperature change of the magnet. To be able to take this effect into account, reference measurements are performed with water, which is expected to show no heating effect. The results of the measurements are discussed in Section 4.3.

While this setup has been used for the measurements discussed in Section 4.3, the cooling has later been altered to be able to keep the magnet temperature within at $(21 \pm 1)\,°C$. To achieve this, the water cooling is equipped with a switching valve which enables the change of the connected thermostat while in operation. To be able to switch the thermostats during operation, a custom build switching valve was developed, including six individual valves. This is necessary since the thermostats constantly pump water during operation, which the valve needs to accommodate. The six valves are modified ball valves that enable the simultaneous switching of all six valves to prevent any switching errors. A schematic illustration of the working principle, as well as a photograph of the finished assembly, can be seen in Figure 4.15

One of the thermostats supplies cooling water with a set temperature of 8 °C and the other warm water with a set temperature of 20.5 °C. While the basic idea of switching the connected water basin to the setup is simple, the resulting temperature change is dependent on many different aspects. Thus the determination of the influences to their full extent is not purposeful. These influences include, but are not limited to, the amount of water stored in the water cooling circuit, the amount of water stored in the thermostat, the cooling power of the thermostat, the temperature difference of the water basins, and the thermal energy stored in the electrical components. To achieve a stabilized magnet temperature, the influences of these factors need to be taken into account. Thus the switching of the cooling needs to happen at different time points than the switching of the AMF. For the measurements shown in Figure 4.16, the cooling was switched from warm to cold water 5 s before the AMF and from cooling to warming 10 s before the AMF. Notable are the erratic temperature changes at the switching of the cooling and the slow decrease of the magnet temperature during operation. The slow temporal decrease of the magnet temperature is linked to the temporal change in cooling water temperature. When the cooling supply is switched, the water which is in the system is flushed into the other thermostat. For the warm water thermostat, the compensation of the cool water is simple due to the ease of heating water. In contrast, the cool water supply needs more time to cool the water back to the set temperature. Causing a slow decrease in cooling water temperature and, thus, the magnet temperature. For the erratic changes during the switching, the process itself is

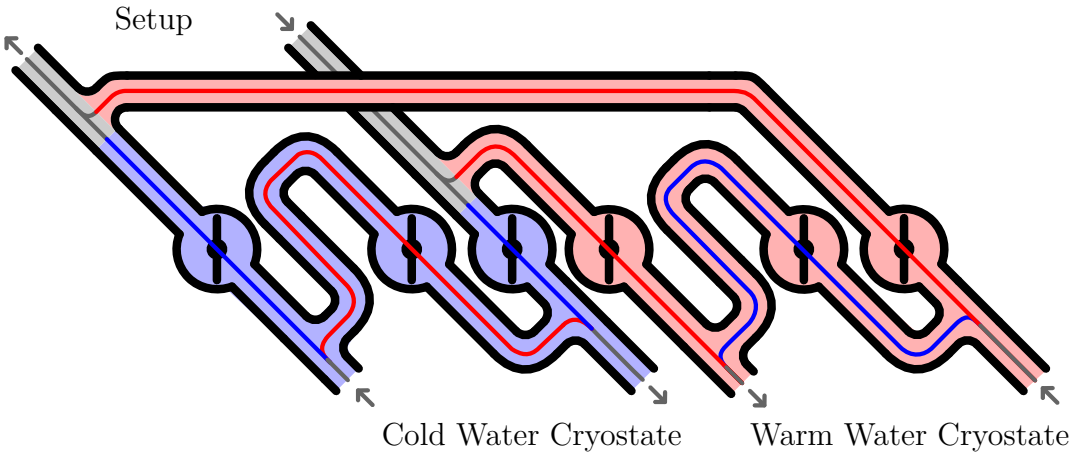

(a) Schematic of the switching valve. To visualize the function principle, the temperature of the water flowing through the pipes is depicted as light red/blue in the background of the pipes. Red background indicates water of 20.5 °C, blue indicates water with a temperature of 8 °C, and gray is dependent on the operational state. The solid lines indicate the paths of water flow for cold water (blue lines) and warm water being supplied (red lines) to the setup.

(b) Photographic image of the switching valve. Please note that the ball valves used in the assembly have been modified, so the handle does not indicate the switching direction correctly.

Figure 4.15: Schematic illustration and photo of the switching valve apparatus developed to stabilize the magnet temperature.

the cause, as the switching introduces a mixture of warm and cold water, which does not perfectly match the momentary cooling requirements of the system.

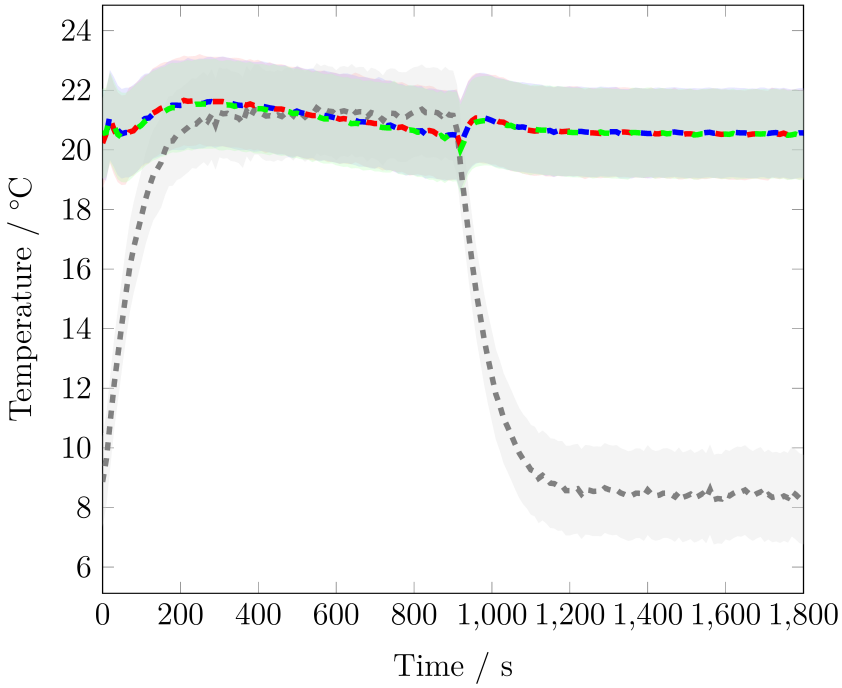

Figure 4.16: Temperature of the magnet stabilized with interchangeable cooling water reservoirs. Depicted are three separate measurements in blue, red, and green with errors as shaded areas. The measurements are almost identical. In the background, the temporal temperature changes of the magnet face temperature, with constant 5 °C cooling installed, are shown in gray, with the error as shaded area.

4.1.8 Microscope

The visual observation of processes is a key concept in science. To be able to observe cells during the operation of the AMF, a microscope was fitted to the setup. The microscope is fitted to be able to adapt the microscope to the hyperthermia use case as much as possible. Traditional microscopes are, like most appliances, made of metal and nowadays incorporate electric components. Metal parts influence the magnetic field, and electronics are at risk of being destroyed. To reduce the influence of the field, the magnet holder, as well as an X-Y-table, are entirely manufactured out of plastic. This leaves the objective as the only component made from metal in the vicinity of the magnet. The microscope frame is, however, made from metal, as plastic would not give the required rigidity. Due to the metal in the objective housing, it is favorable for the objective to exhibit a large working distance. The larger the working distance, the smaller the magnification. This is due to the relation of numerical aperture and focal length. The chosen objective has a working distance of 31.1 mm and a design

magnification of 20× if combined with an imaging lens with a focal length of 200 mm. A schematic representation of the microscope setup is shown in Figure 4.17.

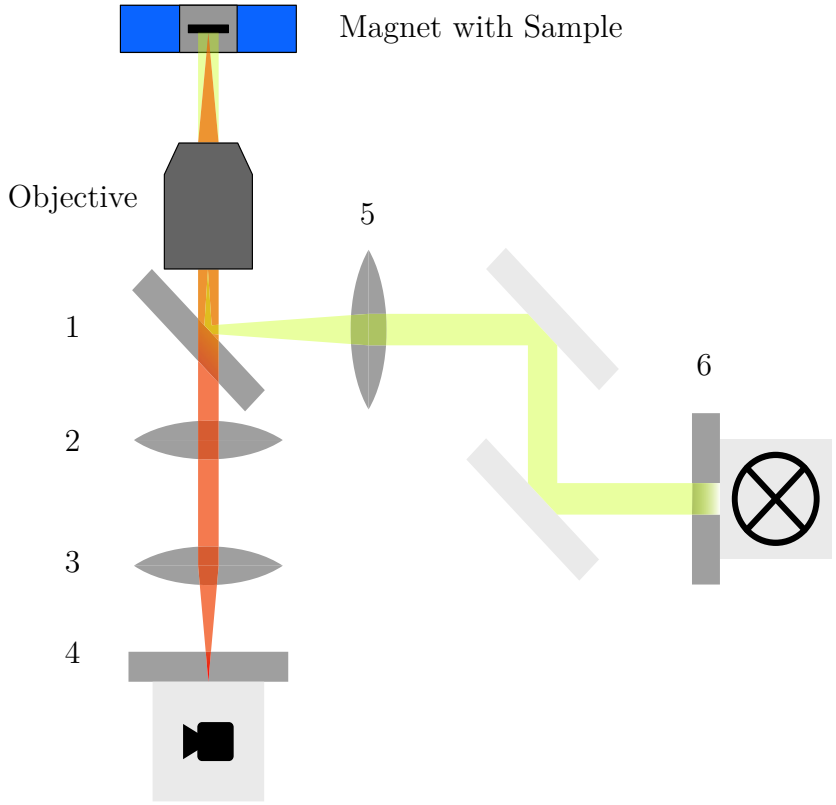

Figure 4.17: Schematic of the microscope fitted to the hyperthermia setup. The components used are: Objective) Plan Apo L 20x (Optosigma, Santa Ana, CA, United States); 1) Semrock FF436/514/604-DI01(IDEX Health & Science, LLC, Rochester, New York, USA); 2) Generic lens with focal length of 150 mm; 3) Generic lens with focal length of 200 mm; 4) BrightLine® Fluorescence Filter 575/25 (IDEX Health & Science, LLC, Rochester, New York, USA); 5) Generic lens with focal length of 80 mm; 6) BrightLine® Multiband Filter 457-530-628 (IDEX Health & Science, LLC, Rochester, New York, USA). The fluorescence lamp used is an INTENSILIGHT C-HGFI (Nikon Corporation, Tokyo, Japan); The camera used is a DMK 31BU03 (The Imaging Source Europe GmbH, Hamburg, Germany).

To determine the effective magnification of the setup, a stage micrometer is used. This amounts to a magnification of 4.92 ± 0.24. The image can be seen in Figure 4.18b. During this project, the camera used (DMK 31BU03) was not designed to be used for fluorescence imaging. Nevertheless the fluorescence image of a standard cell sample (FluoCells™ #2, invitrogen, Thermo Fisher Scientific, Waltham, Massachusetts, USA) shows cell fluorescence at a wavelength of 628 nm (Figure 4.18a) proving that the established setup is capable of performing fluorescence microscopy of samples placed inside the magnet. Since the standard cell sample does not fit inside the magnet gap, the magnet has been removed for this measurement. The rest of the setup has not been

altered. The sample is placed at the same position a sample would be placed inside the magnet gap.

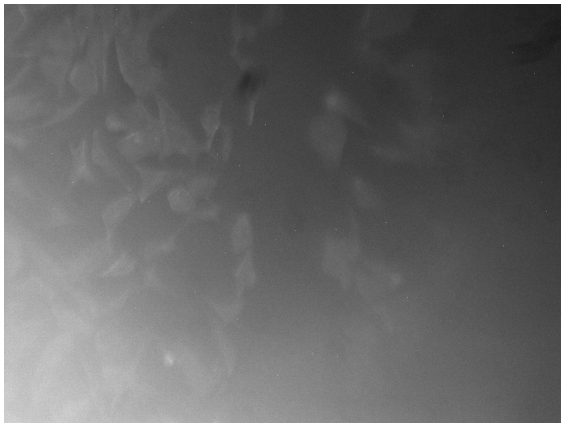

(a) Fluorescence image of a standard cell sample (FluoCells™ #2, invitrogen, Thermo Fisher Scientific, Waltham, Massachusetts, USA). The excitation wavelength is $(575.0 \pm 12.5)\,\mathrm{nm}$. Detected is fluorescence with a wavelength of 457 nm, 530 nm, and 628 nm. Mainly visible are actin filaments, stained with Texas Red™-X Phalloidin.

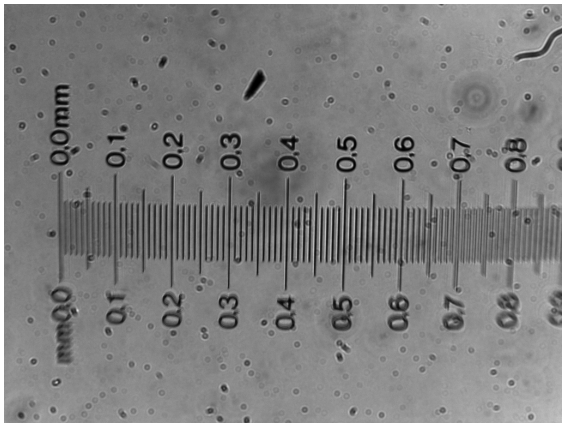

(b) Bright field image of a stage micrometer. In the image, dust particles can be seen; this is due to the limited accessibility, which prohibits frequent cleaning.

Figure 4.18: The scale of both images is the same. An additional scale bar is not given since Figure 4.18b is the image of a physical scale bar. The contrast is enhanced For both images due to better visibility, the original images can be seen in Appendix A.2.

4.1.9 Electrical and Magnetic Characterization

During the assembly process of the circuit are influences that cannot be determined beforehand, such as environmental influences on the setup and alterations of the components due to the assembly and relative positioning. Therefore it is of utmost importance to determine the resulting characteristics of the completed system. As the basic principle of the setup is a resonant circuit (cf. Section 4.1.1), the efficiency can be analyzed by the quality factor. This can be determined utilizing the resonance curve, from which the quality factor Q can be determined via

$$Q = \frac{\omega_{\max}}{\Delta\omega},$$

with the angular frequency of the maximum value $\omega_{\max}$ and the 3dB-Bandwidth $\Delta\omega$, which is where the amplitude is dropped by $\frac{1}{\sqrt{2}}$. This value is chosen since it is also

the frequency where the power has dropped by a factor of $\frac{1}{2}$. Please note that there are different definitions for the quality factor, which do not necessarily give the same result [63]. For the resonance curve, the capacitor voltage U_c has been measured as a function of the excitation frequency ω. Therefore the curve can be fitted with

$$U_{\mathrm{c}}(\omega) = \frac{U_{\mathrm{e}}}{LC\sqrt{\left(\frac{1}{LC} - \omega^2\right)^2 + \left(\omega\frac{R}{L}\right)^2}}, \tag{4.5}$$

with the excitation voltage U_{e}, the capacitance C, the inductance L, the ohmic resistance R and the angular frequency ω (Appendix A.1).

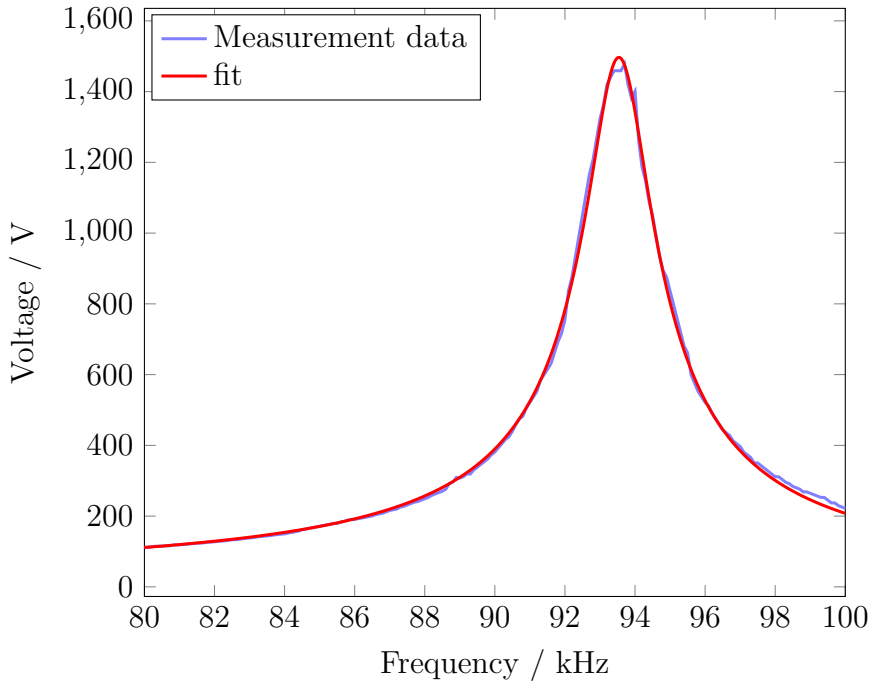

Figure 4.19: Resonance curve of the AMF setup. Calculated from the measured voltage at one capacitor of the array. For better visibility, the errors are not depicted.

For the measurement of the resonance curve, the voltage has been measured at one capacitor due to the maximum measurement capability of the oscilloscope (TDS 2002C, Tektronix, Beaverton, OR, USA) used to determine the peak-to-peak voltage. The overall voltage of the capacitance array U_{arr}has than been calculated via

$$U_{\mathrm{arr}} = U_{\mathrm{meas}}\frac{C_{\mathrm{arr}}}{C_{\mathrm{meas}}},$$

with the measured voltage U_{meas}, the array capacitance C_{arr}, and the capacitance of the measured capacitor C_{meas}. The resulting data with the curve fitted is shown in Figure 4.19. Based on the fitted data, the resonance frequency can be calculated using

Equation (4.4), which amounts to $(93\,540 \pm 10)$ Hz. The bandwidth is (3.2 ± 0.1) kHz. This yields a quality factor of 28 ± 1. As visible from Equation (4.4), the resonance frequency is dependent on the inductance and capacitance[7]. Hence it can be increased/decreased by decreasing/increasing one of these values. Since lowering the inductance would imply a reconstruction of the magnet, increasing the resonance frequency is only feasible by decreasing the capacitance. For the opposite change in frequency, it is possible to increase the inductance by adding a second magnet to the circuit. This, however, would split the energy available for field generation between the magnets. Consequently, it is also preferable to change the capacitance in this case.

From the resonance curve, it is visible that the highest measured peak-to-peak voltage is $U_{pp} = (1473 \pm 20)$ V. This voltage gives rise to a current of $I = (44.4 \pm 0.2)$ A. For the cables and the magnet, the maximum current is mostly determined by the corresponding temperature rise due to Joule heating; these values are unknown and, therefore, would need to be determined by destructive testing, which is not performed due to the single setup available. In contrast to the unknown destruction limit for the cables, the capacitor has a nominal maximum voltage which leads to the failure of the component. For the capacitor array, the nominal voltage is $U_{\mathrm{PP}} = 1838$ V and a nominal current of $I_{\mathrm{PP}} = 57$ A. Since these nominal values are higher than the observed voltages, a linear dependence of magnetic field strength and capacitor voltage is expected. The method chosen to examine if the components are within their operational range is to determine the dependence of magnetic field and voltage. This choice was made since the magnetic field is directly dependent on the current; therefore, it should be directly dependent on the capacitor voltage.

[7]The dependence on the resistance is not used for adjustment as it is tried to keep it as low as possible at all times due to ohmic losses.

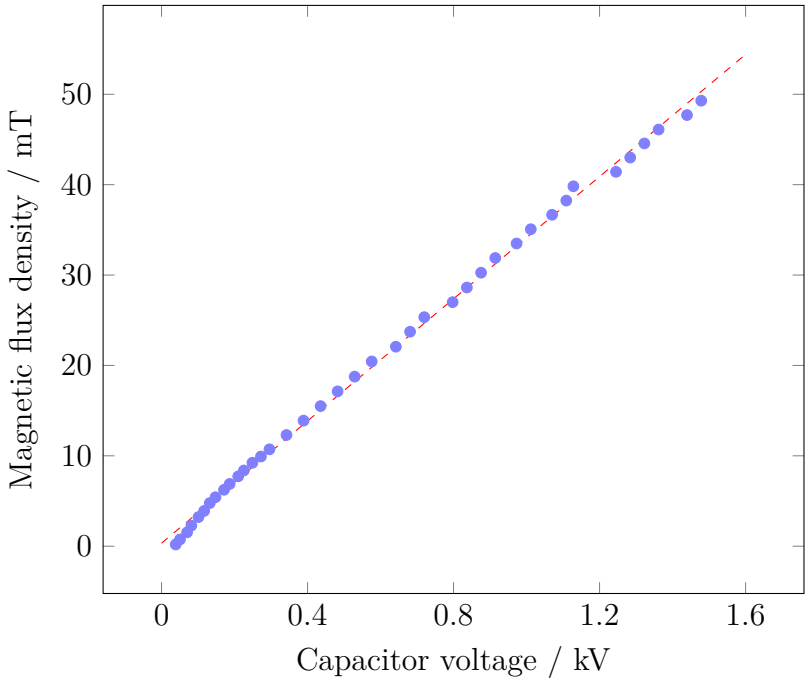

Figure 4.20: Correlation of magnetic field and capacitor voltage showing a linear relation which indicates the load applied to the components does not cause unfavorable effects. The linear fit, shown as red dashed line, follows $B(U) = (0.03378 \pm 0.00049)\mathrm{mT/V} \cdot U + (0.33 \pm 0.37)\mathrm{mT}$. The small jumps at $\sim 800\,\mathrm{V}$ and $\sim 1200\,\mathrm{V}$ are due to switching of the measurement range of the oscilloscope. For better visibility, the errors are not depicted.

As visible in Figure 4.20, the magnetic field shows a linear dependence on the voltage.

As stated in Section 4.1.7, the temperature is not constant over the operation time of the setup. In Figure 4.14a, it is visible that the temperature rises within the first four minutes. The change in temperature is a possible cause for a change in the magnetic flux density, which, therefore, should be monitored, but measuring the magnetic flux density for more than a few seconds would destroy the Tesla meter. To be able to measure for an elongated period of time, the Tesla meter probe is removed from the AMF and inserted into the magnetic field using a rail system. The resulting data is shown in Figure 4.21. It is visible that, at first, there is a rise in magnetic flux density; the maximum is reached below 4 min. For the measurement time of 15 minutes, the magnetic flux density changes within a range of less than 2 %. For times larger than 15 min, the magnetic flux density changes within the margin of 10 %. The decay of magnetic flux density for times larger than half an hour could not be traced back to any source. This is because the system is only fully assembled in the operational state, and there is no option for testing the individual components singled out from the setup. As the decay starts at times larger than the hyperthermia measurement time, it does

not have any influence on the measurement.

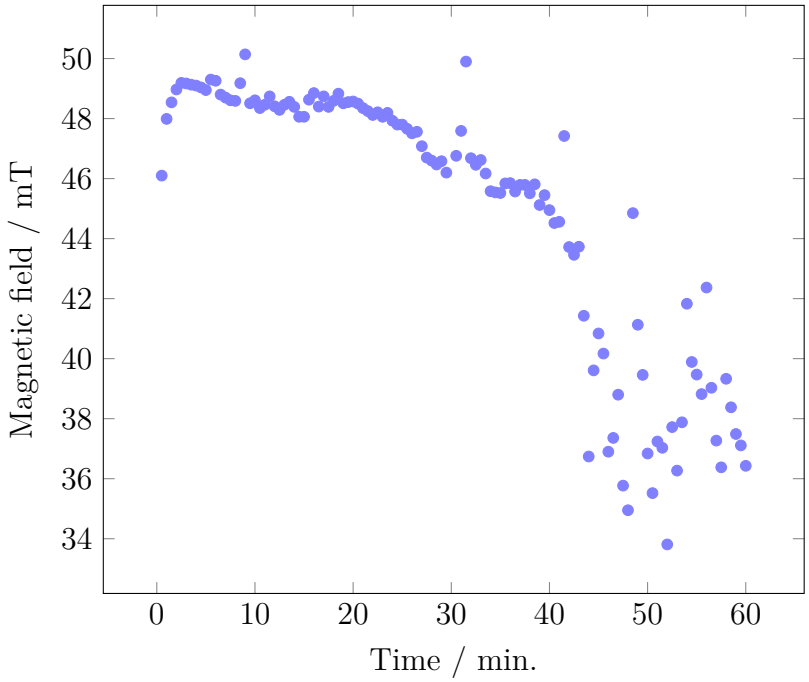

Figure 4.21: Temporal development of the magnetic field. For the typical hyperthermia measurement time of 15 minutes, the magnetic field is changing within 10 % of its maximum value, while measurements for the hyperthermia measurement duration are within an interval of below 5 %. Errors are not shown due to better visibility.

While the temporal resolution is only important for long-term measurements, the spatial variations of the magnetic field influence the measurement from the beginning. The measured spatial distribution is shown in Figure 4.22.

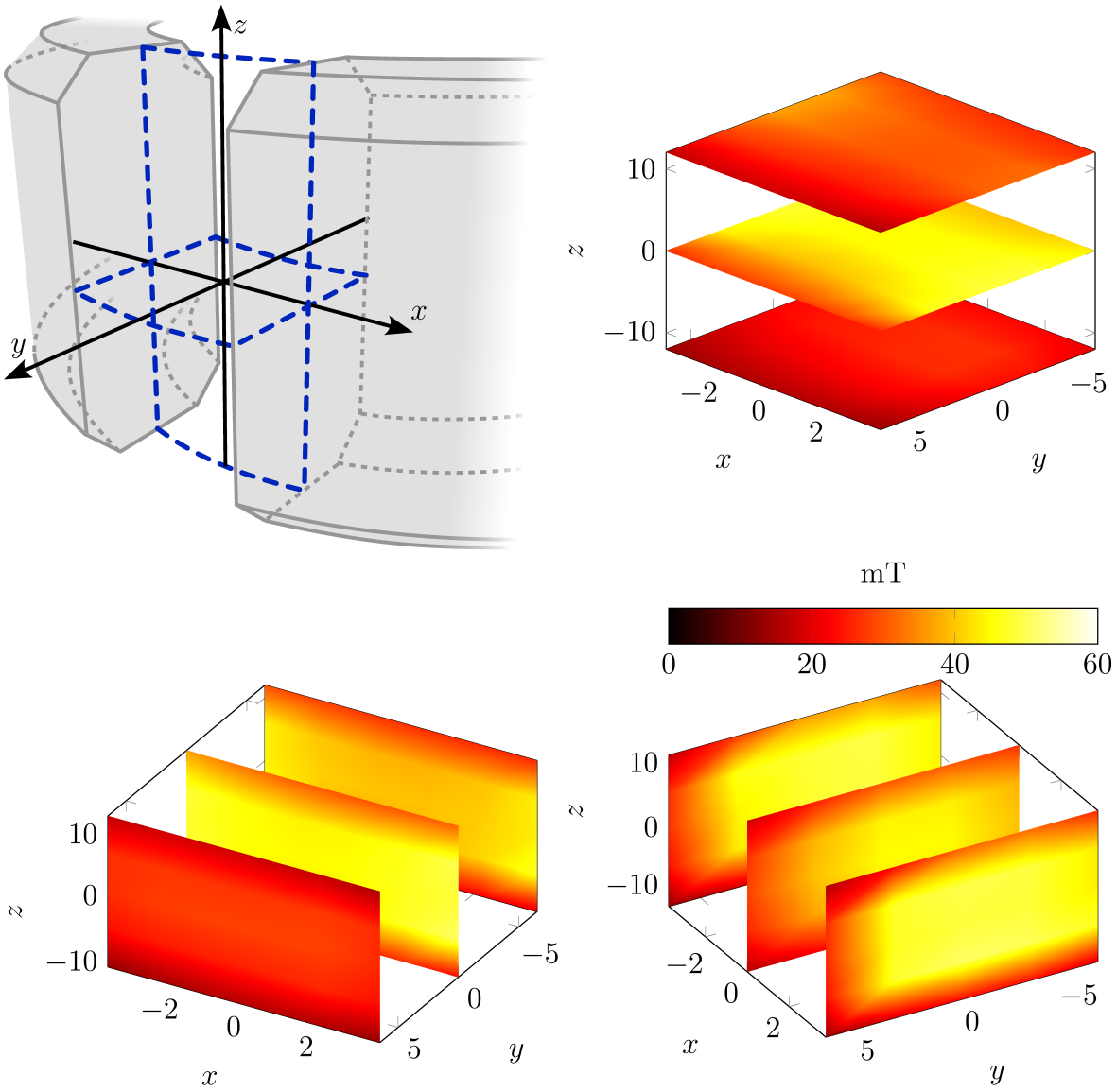

Figure 4.22: Spatial distribution of magnetic flux density in the magnet gap. On the top left, a schematic shows the orientation of the coordinate system in the magnet gap. The field strength is shown interpolated along different cross-sectional planes.

In the spatial plots, it is visible that the magnetic flux density varies in the gap. First of all, it is visible that the magnetic flux density is higher closer to the core faces, which is clear since the stray flux is minimal directly at the core. The magnetic flux density is larger at the inside of the core, which is also explainable by the stray flux, which is larger than at the outside of the gap.

4.2 Magnetic Nanoparticle Characterization

In the scope of this work, three magnetic nanoparticle systems are investigated. The particles used thereby differ in composition, size, and origin. All of the used particle systems consist of a core and a surrounding shell. For the synthetic particle systems Synomag and **B**ionized **N**ano **F**errite(BNF) (micromod Partikeltechnologie GmbH, Rostock, Germany), the core is composed of maghemite and magnetite, respectively. The shell is made from dextran for both of these particles. The third used particle is produced by the bacteria species *Magnetospirillum gryphiswaldense*, which belongs to the group of magnetotactic bacteria. Magnetotactic bacteria are defined by the ability to produce magnetic particles. These particles are called magnetosomes and consist of a magnetite core with a bio-membrane shell. The bacterium uses the particles to align itself with the earth's magnetic field. To achieve this, the bacteria connect multiple magnetosomes to a chain-like structure. The influence of the chain structures on the heating process will also be investigated.

4.2.1 Physical Properties

As discussed in Section 2.2, the magnetic behavior of nanoparticles is mainly defined by the core with only minor influences of the shell, which, in turn, is the main cause of nonmagnetic interactions of the particles. To determine the physical properties of the core, transmission-electron-microscope images have been recorded, giving insight into the cores' size, form, and internal structure. To determine the properties of the shell, dynamic-light-scattering and Zetasizer measurements have been performed, which give information about the outside charge and the hydrodynamic radius of the particles.

Core structure and size

Synomag® 70 particles are nanoflower core-shell particles [64], which means that the core resembles a blossom-, flower- or tree-like shape in electron microscopy images. The corresponding TEM images show substructure in the quasi-spherical morphology of the individual particles (Figure 4.23a). Due to the nanoflower substructure, the particle core is not an individual solid core but rather a structure with multiple segments [65]. A possible core structure 3D drawing is shown in Figure 4.23b. Outgoing from the TEM images, the core diameter has been determined to be $d = (32 \pm 4)\,\mathrm{nm}$. The dextran shell which surrounds the core could not be imaged by the TEM due to insufficient contrast, even when contrast agents are used (Section 3.1.3).

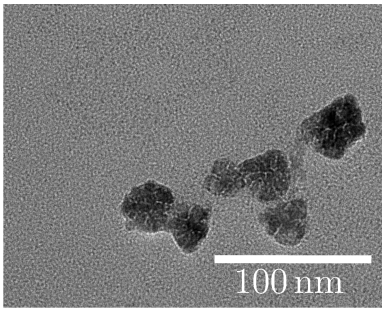

(a) TEM image of Synomag® 70 .

(b) Illustrative representation of Synomag® 70 . The core structure shown does not necessarily resemble the actual core structure.

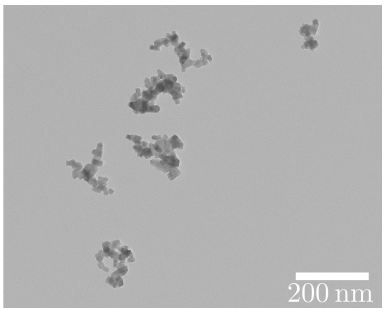

(c) TEM image of BNF 100.

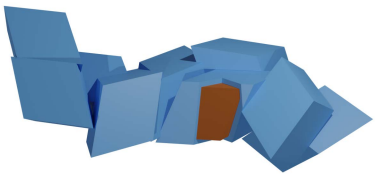

(d) Illustrative representation of BNF 100.

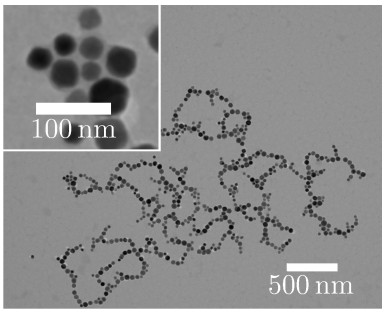

(e) TEM image of magnetosomes.

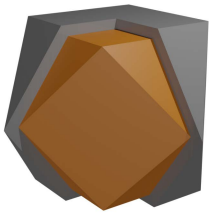

(f) Illustrative representation of magnetosomes.

Figure 4.23: a) TEM image of Synomag® 70 particles. The nanoflower substructure is visible as the granular substructure in the core. The shell could not be imaged. b) Illustrative representation of Synomag® 70 where the nanoflower substructure is indicated. c) TEM image of BNF 100. Visible is the cluster structure where several solid cores are connected. d) Illustrative representation of BNF particles where the parallel piped core structure is shown, as well as the agglomeration in clusters of multiple cores. e) TEM image of magnetosomes chains. The tendency to build chains is visible. In the inset, the cubooctahedral shape is visible. f) Illustrative representation of a magnetosome showing the cubooctahedral shape. For all illustrative representations, the core is shown in orange, while the shell is depicted in green/blue/gray.

BNF particles are cluster-type particles [66]. This means the particle does not possess a single core but is a structure of multiple cores. In contrast to Synomag® 70 particles, however, the cores are more separated and connected by the dextran matrix they are embedded in. As visible in Figure 4.23c, the particles do not resemble a spherical shape. Due to the shape, the definition of a radius is not straightforward. Hence a measure for the size of an effective diameter d_{eff} is introduced, which gives the diameter of a circle that has the same projection area as the BNF imaged. Using this measure, the effective radius has been determined to be $d_{\text{eff}} = (92 \pm 19)\,\text{nm}$. The individual cores were previously determined to exhibit a parallelepiped shape as indicated in Figure 4.23d [67].

The magnetosomes are single-core particles with a biomembrane covering the core. In Figure 4.23e, the individual cores, as well as the chains formed by the bacteria, are visible. Of special note is that the chains are not connected in a web-like structure in the bacteria, as seen in Figure 4.23e; these connections are formed after extracting the chains. The inset shows a magnified image of the cores where the cubooctahedral shape is visible, which is also illustrated in Figure 4.23f. For magnetosomes, the individual cores could be measured by TEM analysis, exhibiting $d = (39 \pm 7)\,\text{nm}$ diameter. The size histograms for BNF particles (Figure 4.24b) and Synomag® 70 particles (Figure 4.24a) show monomodal distributions while the distribution for magnetosomes (Figure 4.24c) has bimodal character. This is attributed to the fact that BNF and Synomag® 70 are synthetically produced particles where the synthesis process is finalized. In contrast, magnetotactic bacteria are disrupted during the production process in order to extract the magnetosomes. The bimodal distribution indicates that there are multiple stages where the growing process is slowed or comes to a temporary stop.

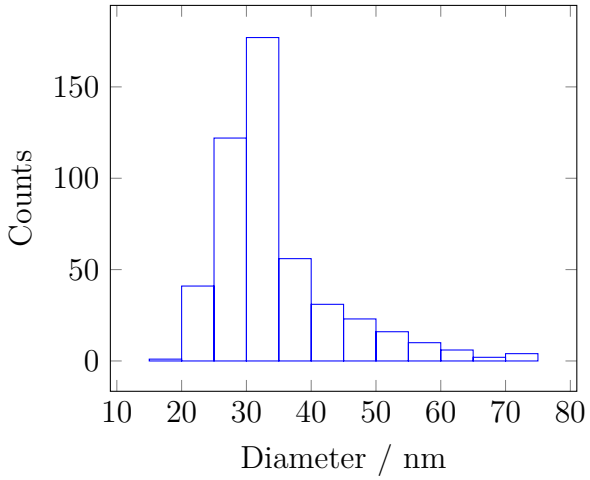

(a) Size distribution of Synomag® with bin size 5 nm $N = 491$.

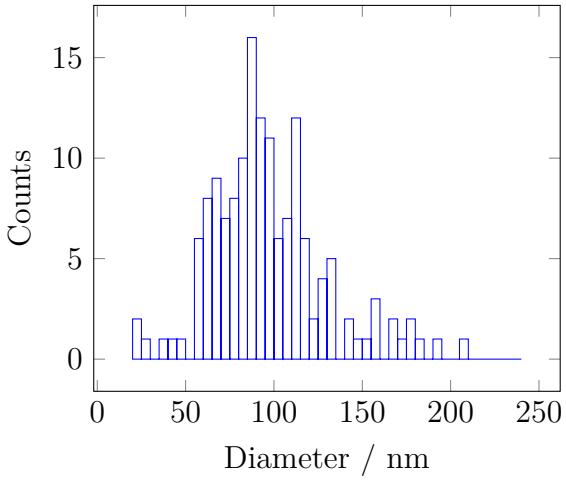

(b) Size distribution of BNF with bin size 5 nm $N = 152$.

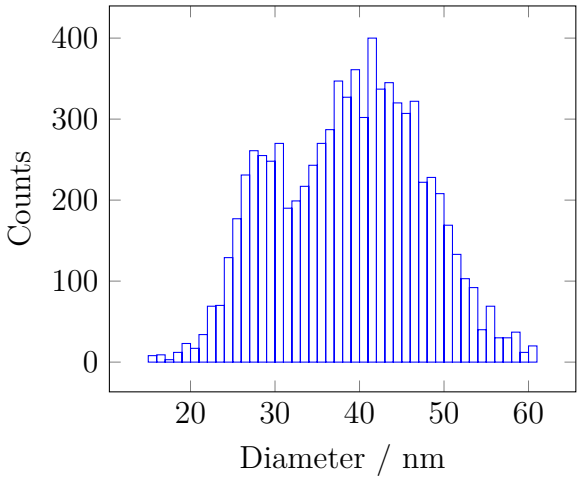

(c) Size distribution of magnetosomes with bin size 1 nm $N = 8006$.

Figure 4.24: Core size distributions of the investigated nanoparticles, determined from TEM images.

Hydrodynamic Radius and ζ-Potential

The hydrodynamic radius, in combination with the ζ-potential, are important properties of the nanoparticle with regard to the interaction with the surrounding. While the chemical surface groups are the determining factor for chemical bindings, the hydrodynamic radius is important for the diffusion properties. The ζ-potential is a measure for the affinity of a particle to form a coulomb bond with a particle of opposing charge and, more importantly, for the aversion to agglomerate with particles of the same charge. As described in Section 3.1.1, there are number and intensity distributions from DLS

measurements to determine the hydrodynamic radius. The resulting data is shown in Figure 4.25. For all particles, it is visible that the intensity distribution indicates higher values than the number distribution, which is easily understandable due to the dependency of the scattered intensity on the diameter to the power of six (Equation (3.1)). For most applications, the intensity number distribution is of interest as it represents the actual size distribution. For Synomag® 70 the number-based average diameter is $d_{\mathrm{N}} = (46.8 \pm 0.6)\,\mathrm{nm}$ which is substantially smaller than the intensity-based value of $d_{\mathrm{I}} = (64.0 \pm 0.4)\,\mathrm{nm}$. For BNF the number distribution diameter $d_{\mathrm{N}} = (103 \pm 2)\,\mathrm{nm}$ which is again substantially smaller than the intensity based-value of $d_{\mathrm{I}} = (132 \pm 2)\,\mathrm{nm}$. Magnetosomes exhibit a number-based mean diameter of $d_{\mathrm{N}} = (23 \pm 9)\,\mathrm{nm}$ which is only $\sim 11\,\%$ of the intensity-based diameter of $d_{\mathrm{I}} = (202 \pm 35)\,\mathrm{nm}$. When comparing the intensity distributions of the particles shown in Figure 4.25 for Synomag® 70 (Figure 4.25a), and BNF (Figure 4.25c), the distribution resembles a normal distribution. The distributions resemble the shape of a normal distribution on a linear x-scale, while the plot is on a log x-scale. The intensity distribution for magnetosomes exhibits a tail towards lower diameters. This indicates that the sample is not mono-disperse, which is underpinned by the measured polydispersity index of the samples. At the same time, it is close to zero for Synomag® 70 and BNF with values of 0.048 ± 0.006 and 0.04 ± 0.01, respectively, the value for magnetosomes is larger at 0.295 ± 0.004. The higher poly-dispersity index also indicates a broader distribution that accounts for the biological origin of the particles. Due to the high polydispersity of the sample, the evaluation method, DLS, is not well suited for the sample; therefore, the resulting diameters need to be treated with caution.

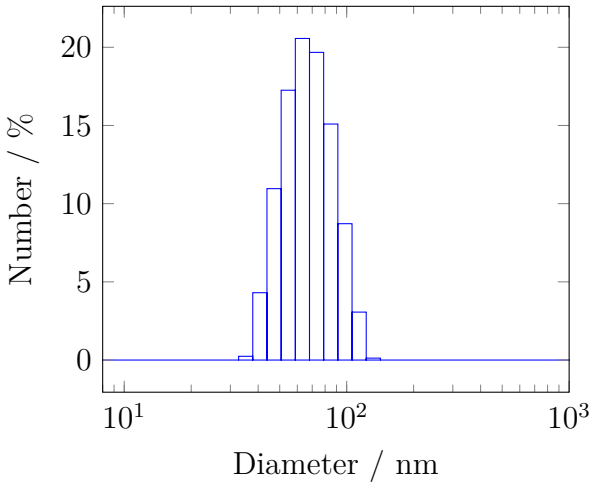

(a) Average DLS Intensity Distribution for Synomag® 70 .

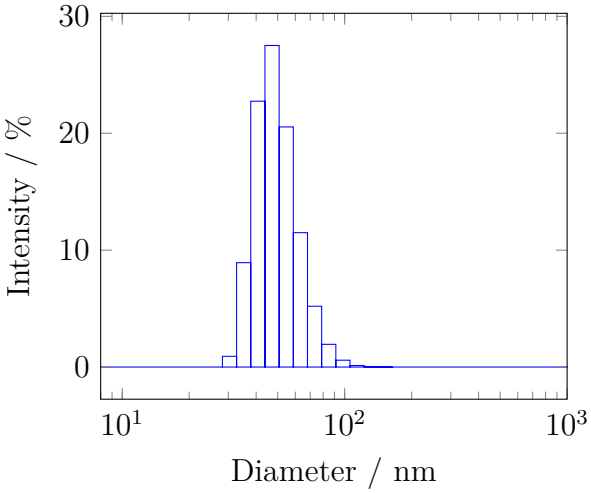

(b) Average DLS Number Distribution for Synomag® 70 .

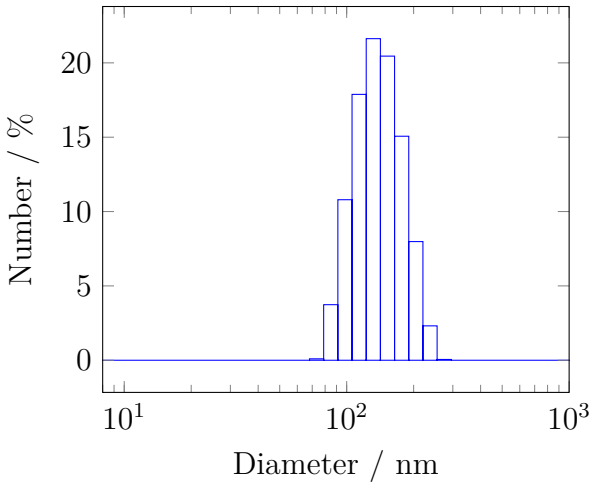

(c) Average DLS Intensity Distribution for BNF 100.

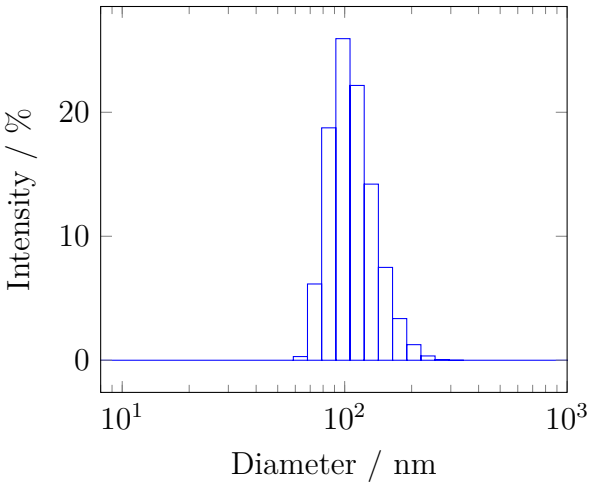

(d) Average DLS Number Distribution for BNF 100.

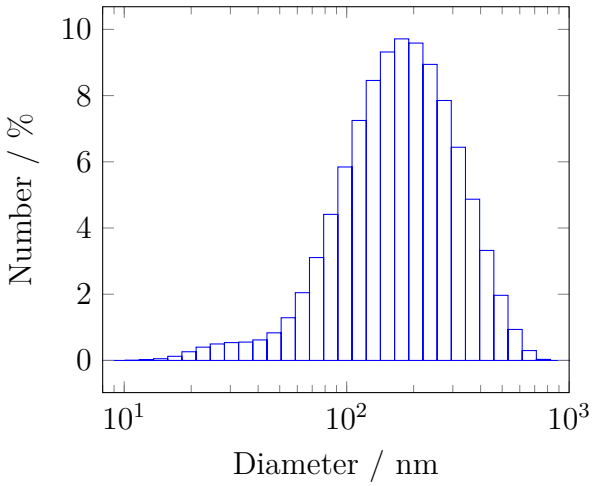

(e) Average DLS Intensity Distribution for Magnetosomes.

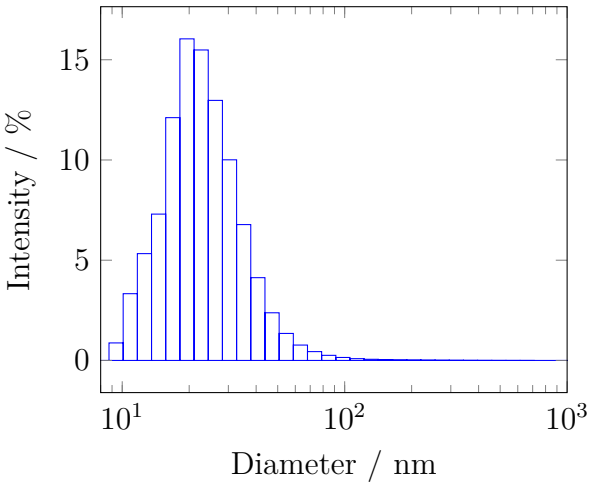

(f) Average DLS Number Distribution for Magnetosomes.

Figure 4.25: DLS intensity and number distributions for the investigated particles. For the magnetosome measurements, diameters larger than 1000 nm are not shown due to the negligible amount.

The ζ-potential of the particles is $\zeta = (-1.8 \pm 0.9)\,\mathrm{mV}$ for Synomag® 70 and $\zeta = (-0.8 \pm 0.4)\,\mathrm{mV}$ for BNF nanoparticles which is both comparably close to the isoelectric point. For magnetosomes in contrast the ζ-potential is $\zeta = (-31 \pm 2)\,\mathrm{mV}$. The considerably negative ζ-potential is beneficial for the biocompatibility of the magnetosome particles as it was shown to decrease unspecific interactions inside cells [68, 69]. Please note that the ζ-potential and the hydrodynamic diameter are dependent on the surrounding media, its pH value, and the concentration. Therefore the results here are valid only for the dispersion media described in Section 3.1.1 and Section 3.1.2.

4.2.2 Magnetic Properties

All properties discussed until now are common for all types of nanoparticles. In this chapter, the unique feature of the used particles, namely the magnetic behavior, will be discussed.

AC-Susceptibility

As described in Section 2.3, the power dissipated by superparamagnetic nanoparticles can be calculated using the linear response theory by utilizing the out-of-phase/ imaginary component of the AC-susceptibility. For the used particles, the response to alternating magnetic fields has been determined using a Dynomag AC-Susceptometer (RISE, Sweden).

For Synomag® 70 (Figure 4.26), the magnetization starts off mostly in phase as the imaginary part of the AC-Susceptibility is at its minimum, and the real part is at its maximum. The imaginary part exhibits a maximum at 3.8 kHz before and after the course is strictly monotonic. The real part, in contrast, is strictly monotonic falling. The comparably broad peak of the imaginary part and the slow decrease of the real part is a result of the multiple core parts and indicate the relaxation of internal disordered spins [70]. As described in Section 3.1.4, the Néel and Brownian relaxation times have been extracted from these data via Equation (3.7) and amount to $\tau_\mathrm{N} = 1.0 \times 10^{-6}\,\mathrm{s}$ and $\tau_\mathrm{B} = 9.6 \times 10^{-5}\,\mathrm{s}$.

In the case of BNF particles, the imaginary part exhibits a maximum at 84 Hz, three orders of magnitude lower than Synomag® 70 . The real part of the magnetization decreases quickly; starting from a frequency-wise low maximum, the magnetization vanishes quickly towards higher frequencies (Figure 4.26). This behavior is similar to single domain particles, although the magnetization is phase lagging compared to the external field already at lower frequencies. The relaxation times extracted from the

fits, performed by the Dynomag software, are $\tau_N = 6.5 \times 10^{-6}$ s and $\tau_B = 1.7 \times 10^{-3}$ s. For both particles, the Néel relaxation times are lower, thus dominating the relaxation processes. This behavior was already shown for maghemite particles [71].

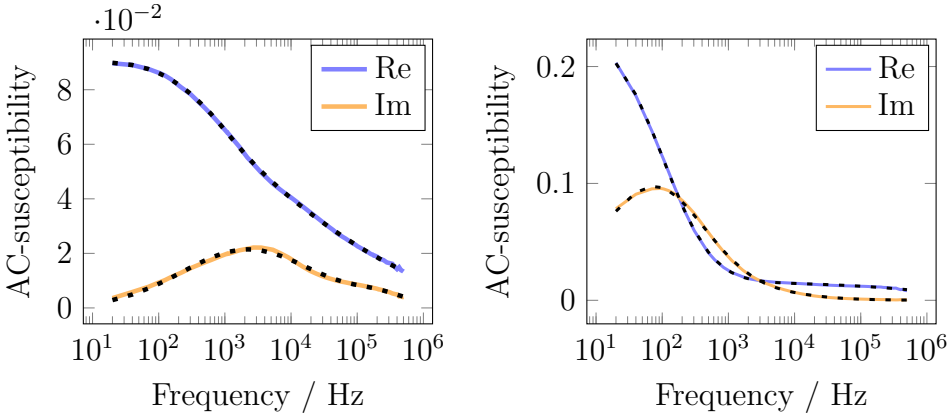

(a) AC-suseptibility of Synomag® nanoparticles

(b) AC-suseptibility of BNF nanoparticles

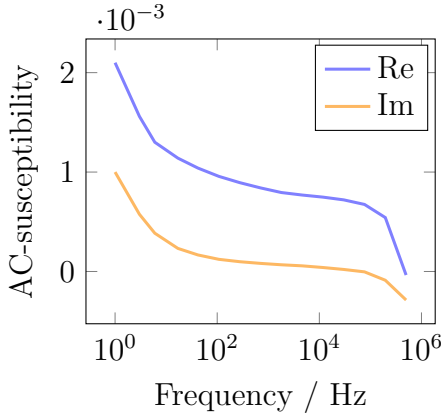

(c) AC-suseptibility of Magnetosomes

Figure 4.26: AC-susceptibility measurements of the used nanoparticle systems measured with the Dynomag System. Displayed is the real (Re) and imaginary (Im) part. The corresponding fits performed by the susceptometer are shown as dashed lines Please note the different amount of frequency points taken due to technical reasons.

Magnetosomes behave vastly differently as the real and imaginary both decrease strictly monotonic with absolute values in the order of 10^{-3} for the lower end of measured frequencies, which with increasing frequency lowers to negative values. While the measurement values at lower-end frequencies are two orders of magnitudes above the susceptometer resolution limit of 10^{-5}, they vanish towards higher frequencies. The low values indicate that magnetosomes are not substantially magnetized by the 0.5 mT

the susceptometer. The decrease, however, indicates that the magnetosomes are in a blocked state. A determination of the relaxation times was not possible because the field magnitude of the susceptometer is small compared to the field amplitude in the hyperthermia setup. Thus it should be noted that it has been reported that the relaxation times are dependent on the field strength [40], although Néel and Brownian relaxation times are often determined in the zero field limit.

Table 4.1 summarizes all measurement results, supplemented with data about iron concentration and particle number from the data sheets [65, 66]. By comparing the TEM diameter with the hydrodynamic diameter of the particle, it can be observed that the hydrodynamic diameter is larger for Synomag® 70 and BNF but smaller for magnetosomes. This larger hydrodynamic diameter is expected due to the hydration shell. The smaller diameter for the magnetosomes is explained by the preparation process of the sample, where an additional filtering step is introduced, causing mostly small particles to be in the solution. The filtering effect of magnetosome cores which are still smaller than the filter size but are apparently missing in the DLS measurement, is attributed to the increased likelihood of chain formation for particles with larger magnetic moments. The build chains are then also removed from the sample.

Parameter	Synomag® 70	BNF	Magnetosomes
d_{TEM} / nm	32 ± 4	92 ± 19	39 ± 7
d_{N} / nm	46.8 ± 0.6	103 ± 2	23 ± 9
d_{I} / nm	64.0 ± 0.4	132 ± 2	202 ± 35
PDI	0.048 ± 0.006	0.04 ± 0.01	0.295 ± 0.004
ζ-Potential / mV	-1.8 ± 0.9	-0.8 ± 0.4	-31 ± 2
f_{max} / Hz	3.8×10^3	84	NA
τ_{N} / s	1.0×10^{-6}	6.5×10^{-6}	NA
τ_{B} / s	9.6×10^{-5}	1.7×10^{-3}	NA
c_{Fe} / mg/ml	0.6	0.6	0.72
particles / #	2.2×10^{12}	6.0×10^{11}	5.7×10^{15}

Table 4.1: Summary of the particle characterization results. Iron concentration and a number of particles are given for a concentration of 1 mg/ml. For Synomag®70 and BNF, the iron concentration and particle number are taken from the data sheets [65, 66]. The Néel and Brownian relaxation times are measured at 0.5 mT using the Dynomag.

4.3 Magnetic Hyperthermia Results

In this chapter, the response of the characterized particle systems to being subjected to an alternating magnetic field will be evaluated regarding the heat generated by the particles in solution. By thermal imaging (Section 3.2), the surface temperature of the particle solution sample and the bulk heating properties of the systems are determined. The surface temperature evolution is monitored with a thermal imager (Infratec, Dresden, Germany) which images the whole electromagnet every 10 s. Outgoing from the thermal image, the mean temperature of the sample's upper surface is determined utilizing the *Irbis3* software (Infratec, Dresden, Germany). The results will be described, utilizing the heating and cooling functions introduced in Section 2.4. The temporal evolution of the sample temperature is of major interest for the hyperthermia application. Figure 4.27a shows an exemplary image of a magnetosome sample shortly before the AMF is switched off. The yellow surrounding areas depict measurement areas. The blue areas are called correction areas, where the ambient temperature and the emission coefficient can be set. The corresponding extracted values are shown in Figure 4.27b. The sample measurement area represents the pixels that are averaged to obtain the sample measurement value. The background temperature does not determine a reference for the case where no sample is present. Still, rather it represents the room temperature with slight influences by the reflected radiation of the setup. This measurement is performed to be able to monitor the room temperature during the whole measurement, as drastic changes would influence the measurements. The magnet's temperature is measured to determine if the AMF is working during the whole measurement period, as variations of the AMF directly influence the magnet temperature. The magnet temperature is measured between the windings far away from the sample itself. Thus, it is not usable for the determination of the temperature in the vicinity of the magnet.

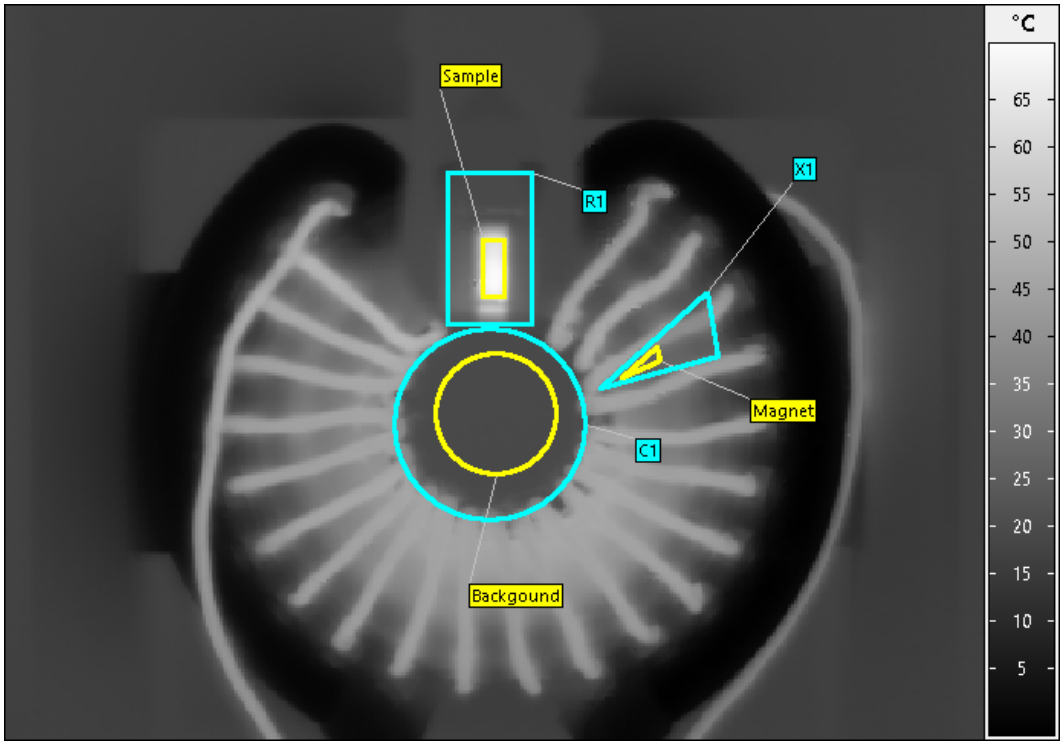

(a) Examplary image of the magnet with measurement areas indicated. The correction areas for the epsilon values are indicated in blue, the measurement areas are indicated in yellow. For visibility reasons, the line width has been increased.

ID	mean/°C	min/°C	max/°C	σ	ϵ	**Pixel Area**
Sample	66.03	57.45	70.99	3.41	**0.95**	**198**
Background	18.88	18.65	19.30	0.64	**0.94**	**1685**
Magnet	28.50	25.47	36.55	2.45	**0.94**	**55**

(b) Measurement results from the image shown in a). The values set by the experimentalist are bold, with set emission coefficient ϵ and standard deviation σ of the temperatures measured in the corresponding area.

Figure 4.27: Exemplary image of a heated magnet with measurement results and set values. The measurement shown is performed with magnetosomes. The particles were measured at 93.75 kHz.

In Figure 4.28, the temporal temperature evolution is shown for the same measurement shown in Figure 4.27a. The shaded areas show the maximum and minimum temperatures. While the background exhibits close to no temperature spread, the sample and the magnet show a considerable standard deviation. For the magnet, this is understandable; as the measurement area is situated between the windings of the coil, the temperature is increased in the direct vicinity of the wire. As the magnet

temperature is only used for control of the operational status, this does not need any further investigation. For the sample, however, the spatial temperature distribution is an insight-granting feature. Figure 4.29 shows the spatial temperature spread for the sample measurement at three different times from shortly before switching off the AMF up to two minutes later. Figure 4.29a, which is shortly before switching the AMF, shows a clear hot spot towards the back of the magnet's gap. This does coincide with the increase in magnetic field strength towards the back of the magnet's gap. In the direction of the sample edges, the measured temperatures drop. While this is attributed to the colder surrounding of the sample, it contrasts with the increasing magnetic field strength towards the magnet faces. Another possible influence that needs to be kept in mind is the angular dependence of the IR emission. This cannot be determined at the edges of the sample due to the formation of menisci at the edges.

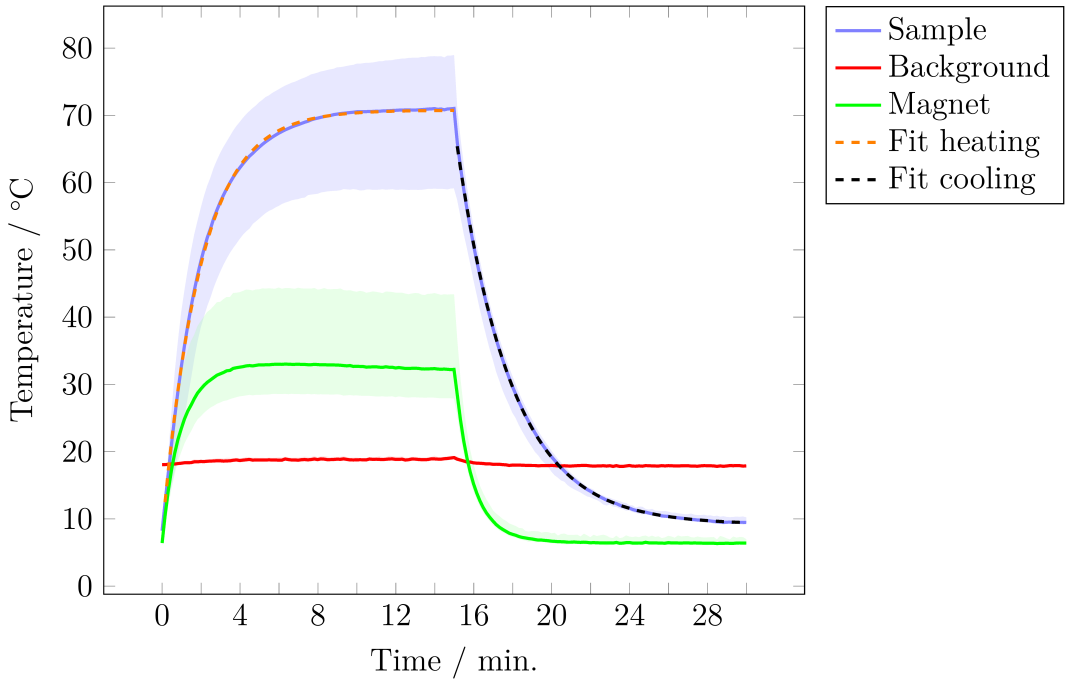

Figure 4.28: Example measurement from the measurement shown in Figure 4.27b. The areas with reduced opacity represent the minimum and maximum values for each measurement area. The shown data is recorded with a magnetosome sample. The particles were measured at 93.75 kHz

Figure 4.29b and Figure 4.29c show the spatial temperature 1 min and 2 min after the AMF is switched off. It is visible that the hotspot vanishes, and the temperature of the sample becomes more uniform with time while the edges remain colder. It is important to notice that the temperature scales are not the same for all images. The lowest value of Figure 4.29a is higher than the highest temperature of Figure 4.29b (the same holds true for Figure 4.29b and Figure 4.29c). The different scales are chosen

because, with a uniform colormap, temperature differences would not be visible. This is especially important as the false impression that the outer part of the sample is getting hotter could arise. From these observations, the important aspect that the temperature cannot be deemed to be consistent for the whole sample can be taken. The temperature differences are similar to the differences in field strength shown in Figure 4.22. While the temperature differences do not necessarily align perfectly, this can be caused by the field dependence of the relaxation process and the corresponding change in dissipated heat.

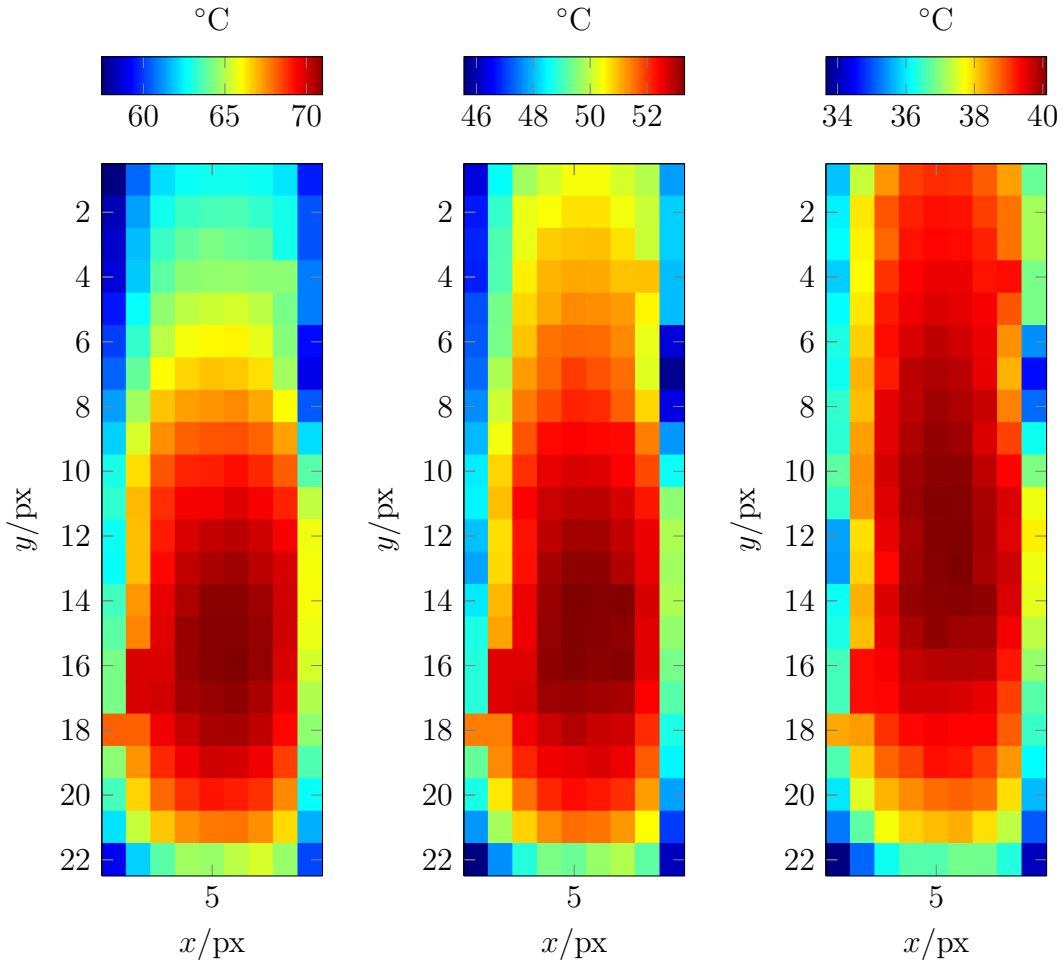

(a) Shortly before switching off the AMF. **(b)** 1 min after switching of the AMF. **(c)** 2 min after switching of the AMF.

Figure 4.29: Temporal evolution of the spatial heat distribution at three different times, showing the cooling process. Please note the different color maps for each plot. The particles were measured at 93.75 kHz.

A major drawback of the spatial temperature differences, in combination with the uncertainty of the sample placement, is the difficulty in determining the sample area. As the sample starts with a temperature close to the ambient temperature, the repeatable

positioning of the sample area is not possible. To overcome this problem, the sample area is determined at the moment when the sample is at its maximum temperature. However, due to the unclear borders of the sample, combined with the not perfectly repeatable placement of the sample, the determination of the borders introduces a bias. Automation of this process is due to the ongoing development of the setup, however not purposeful, as it would introduce restrictions. Therefore the sample area is determined manually for every measurement by selecting a considerably homogeneous area as the measurement area. This criterion was chosen as the temperature change at the border of the sample is attributed to interaction with the sample environment and changes in the emissivity, as mentioned before.

The exemplary data shown in Figure 4.28 in combination with the spatial data shown in Figure 4.29 is clear proof that the heating of the sample is not caused by the magnet, as the magnet is constantly below the sample temperature and the hot spot of the sample is in its center. This is especially remarkable as the magnet temperature is measured not at the gap faces but between the windings where the temperatures are even higher than at the faces (Section 4.3.6).

In this section multiple comparisons of measurements concerning different parameters are done. Due to the measurements being performed during the ongoing development of the setup, the measurement frequency varies. Therefore the measurements from one subsection are not necessarily comparable to measurements from another subsection. The frequency of the measurements is given in the caption of the data figures.

4.3.1 Magnetic Field Dependence of the Sample Temperature

Since the magnetic field strength is adjustable as discussed in Section 4.1.9, this poses the possibility of changing the temperature. This is even then the case if the concentration cannot be changed, as is the case in biological samples after incubation or with samples where the heating is influenced by other aspects which have not been known before the experiment.

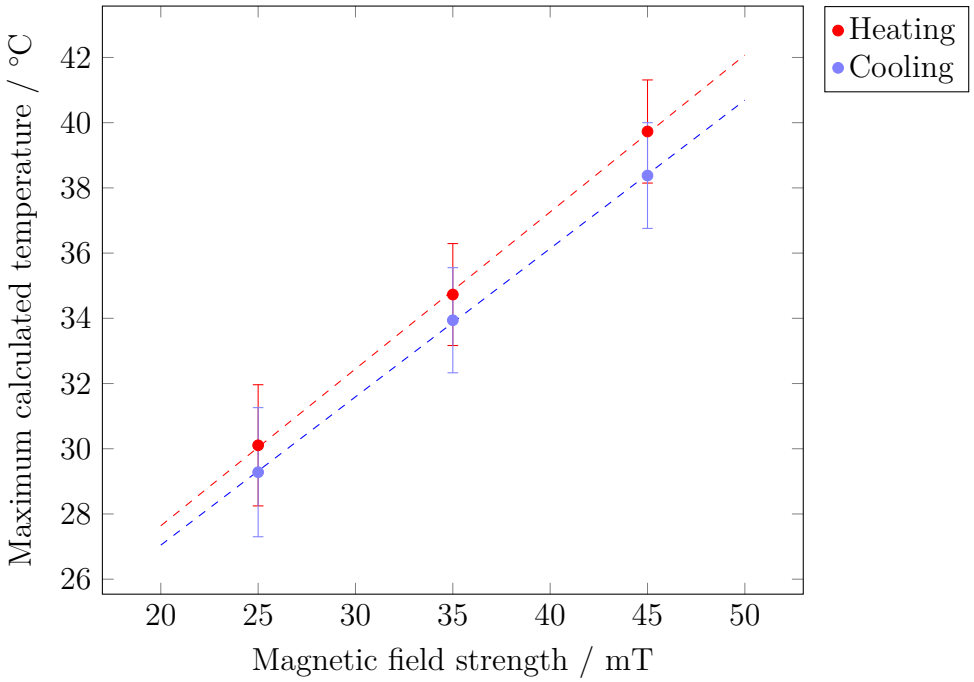

Figure 4.30: Maximum temperature field dependence. Values are calculated using the fit for heating and cooling (Equation (2.23)). Both data sets show linear behavior as indicated by the corresponding fits depicted as dashed lines in the same color as the data points. The particles were measured at 98.10 kHz

Figure 4.30 shows how the maximum measured temperature depends on the magnetic field strength. The temperature data is extracted as described in Section 2.4. It is visible that the maximum temperature can be described by a linear dependence on the magnetic field strength in the determined range. While it is possible to extrapolate this behavior to a certain degree, it must be clear that the dependence is limited. The maximum extent of this range is from room temperature up to $\sim$ 100 °C. In this maximal possible range, the lower limit is due to the impossibility of cooling via magnetic hyperthermia, and the upper limit is given by the energy needed to boil the water. The actual limit of the linear regression is lower, at least for bulk samples, as

the evaporation of water will extract an increased amount of energy from the sample.

The linear dependence observed shows that the magnetic fields applied to the sample are high enough to cause the saturation of Equation (2.17).

4.3.2 Concentration Dependence of the Sample Temperature

In this section, the dependence of concentration and reached sample temperature will be investigated. The measurement results of the relation of dissipated power and particle concentration c of Synomag® 70 are shown in Figure 4.31.

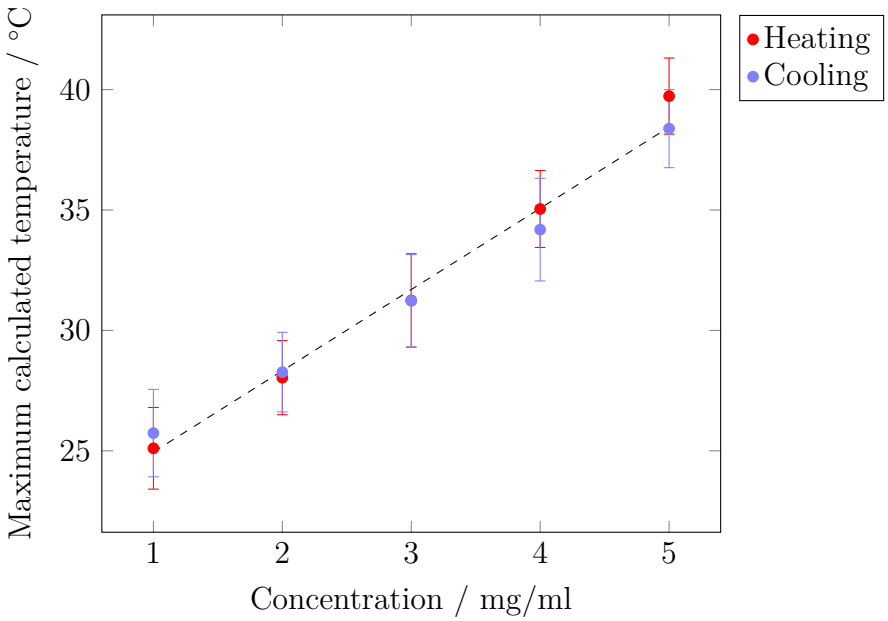

(a) Calculated maximum temperature from the fit data for heating and cooling curves (Equation (2.23)). The linear dependence on the concentration is fitted with overheating and cooling points combined and depicted as a dotted black line.

Slope/ °C ml/mg	Vertical intercept / °C
3.37 ± 0.35	21.6 ± 1.1

(b) Fit parameters from the linear fits with fit errors

Figure 4.31: Maximum temperature concentration dependence. Values are calculated using the fit for heating and cooling (Equation (2.23)). The linear fit is done to both datasets combined and shown as a dotted line. The particles were measured at 98.10 kHz.

For the considered measuring range the temperature follows $T = (3.37 \pm 0.35)\,°\mathrm{C\,ml/mg} \cdot c + (21.6 \pm 1.1)\,°\mathrm{C}$. The concentration of 5 mg/ml represents the stock solution; the rest of the samples are diluted in PBS (**P**hosphate-**b**uffered **s**aline). In Figure 4.31, the heating/cooling results are displayed in red/blue. Here it is evident that the results are compatible with each other. Therefore the fit takes all points into account. The temperature range accessible with concentrations from 1 mg/ml to 5 mg/ml leads to temperatures from about 25 °C to 40 °C which covers the physiological temperature range for humans. While the linear dependence allows for easy adjustment of the achievable temperature, the linear dependence indicates that the setup is not limited in terms of power supplied to the particles by the AMF within the tested concentration range. Please note that the dependence of concentration and temperature will deviate from the linear model for larger concentrations as the temperature reaches saturation. However, this is not relevant for biomedical experiments as the saturation with nano-particles does not pose a reasonable approach.

4.3.3 Solvent Dependence of the Sample Temperature

Heat generation in a cellular environment is of major interest in the usability of magnetic-nano particles for magnetic hyperthermia in biomedical experiments. To gain insight into the heating behavior, Synomag® 70 have been measured in cell lysate and compared to measurements in PBS buffer.

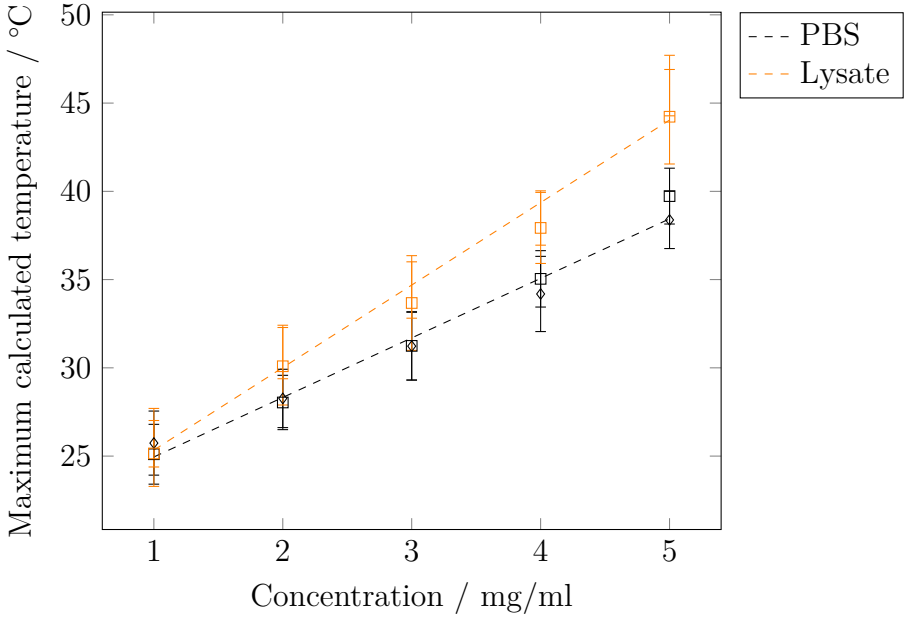

(a) Calculated maximum temperature from the fit data for heating and cooling curves (Equation (2.23)). Dependent on the solvent and particle concentration. Data from cooling curves is depicted as diamond, data from heating curves is depicted as squares.

	Slope/°C ml/mg	Vertical intercept / °C
Water	3.37 ± 0.35	21.6 ± 1.2
Lysate	4.67 ± 0.56	20.7 ± 1.9

(b) Fit parameters from the linear fit with fit errors.

Figure 4.32: Maximum temperature solvent dependence. Values are calculated using the fit for heating and cooling (Equation (2.23)). The linear fit is done to heating and cooling datasets combined and shown as a dotted black line. The particles were measured at 98.60 kHz.

The results shown in Figure 4.32 show a slight difference in heating for particles in cell lysate and PBS. It is also visible that the linear dependence on concentration is still present. The results of this measurement are important for use in biomedical

applications as it underlines that the temperature reached inside tissue can depend on the surrounding solvent. Furthermore, it indicates that the heating response of particles is only comparable if the particles are dissolved in the same solvent.

4.3.4 Particle Dependence of the Sample Temperature

The determining factor for the heating is the used nano-particle. In Figure 4.33, the concentration dependence is measured for Synomag® 70 , BNF and magnetosomes.

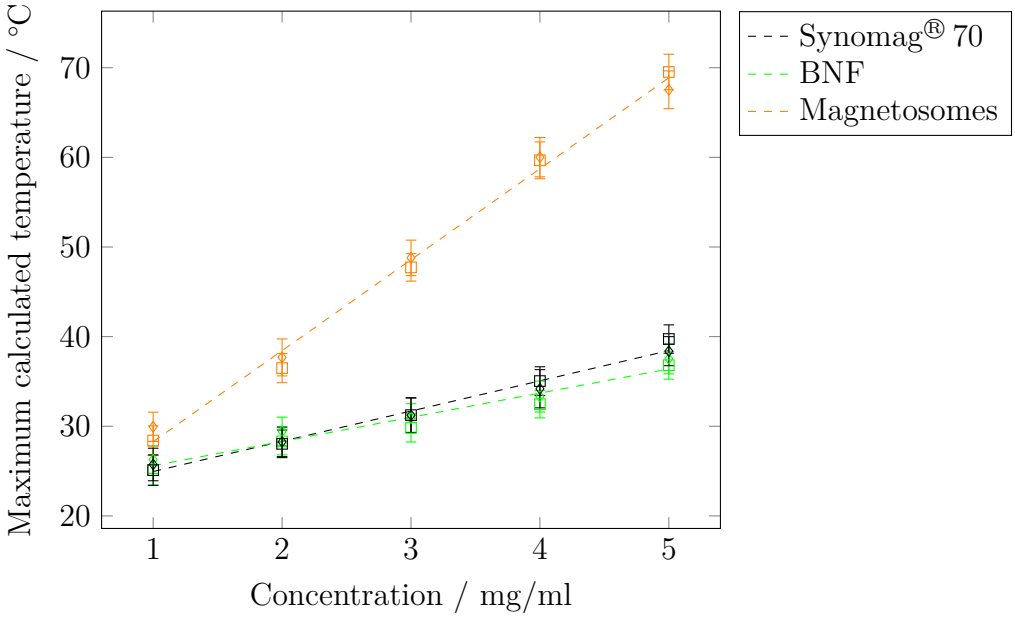

(a) Calculated maximum temperature from the fit data for heating and cooling curves (Equation (2.23)) dependent on the particle.

	slope/°C ml/mg	vertical intercept / °C
Synomag	3.37 ± 0.35	21.6 ± 1.2
BNF	2.70 ± 0.47	22.9 ± 1.6
Magnetosomes	10.14 ± 0.65	18.1 ± 2.2

(b) Fit parameters from the linear fits with fit errors

Figure 4.33: Maximum temperature solvent dependence. Values are calculated using the fit for heating and cooling (Equation (2.23)). The linear fit is done to both datasets combined and shown as a dotted black line. The particles were measured at 98.10 kHz for Synomag® 70 , 91.80 kHz for BNF, and 93.75 kHz for magnetosomes.

It is visible that the maximum temperatures reached, and therefore the energy dissi-

pated is very similar for Synomag® 70 and BNF. For this interpretation, one needs to consider the fact that the magnetosome concentration is given for the iron content while the concentration for Synomag® 70 and BNF are given for the total particle concentration. The iron concentration for Synomag® 70 and BNF is 60 % of the particle concentration. This results in $(5.62 \pm 0.59)\,°\mathrm{C\,mg/ml} + (21.6 \pm 1.2)\,°\mathrm{C}$ for Synomag® 70 and $(4.50 \pm 0.79)\,°\mathrm{C\,mg/ml} + (21.6 \pm 1.2)\,°\mathrm{C}$ for BNF, which is both still considerably lower than the $(10.14 \pm 0.65)\,°\mathrm{C\,mg/ml} + (18.1 \pm 2.2)\,°\mathrm{C}$ for magnetosomes. The use of two different methods to determine the iron concentration is a result of the different handling of the particles. A further limitation to the interpretability is the difference in measurement frequencies. The underlying observation, that different particles show different heating behavior, however is unaffected, as the frequency influence is linear as given by eq. (2.16). The influence of the susceptibility is negligible as the measurement shows a flat slope in the region of 100 kHz (fig. 4.26). The magnetic field has the same amplitude in all measurements.

4.3.5 Conformation Dependence of the Sample Temperature

While Synomag® 70 and BNF exist only in one conformation, magnetosomes exist in multiple conformations during the production process. To investigate the influence, the conformation has on the heating behavior, the magnetosomes have been investigated at different stages of the extraction process. The first investigated state is the magnetosome chains in intact bacteria. The second stat is the magnetosome chains extracted. The third state is denatured magnetosomes. This means that the outer biomembrane is removed from the particles.

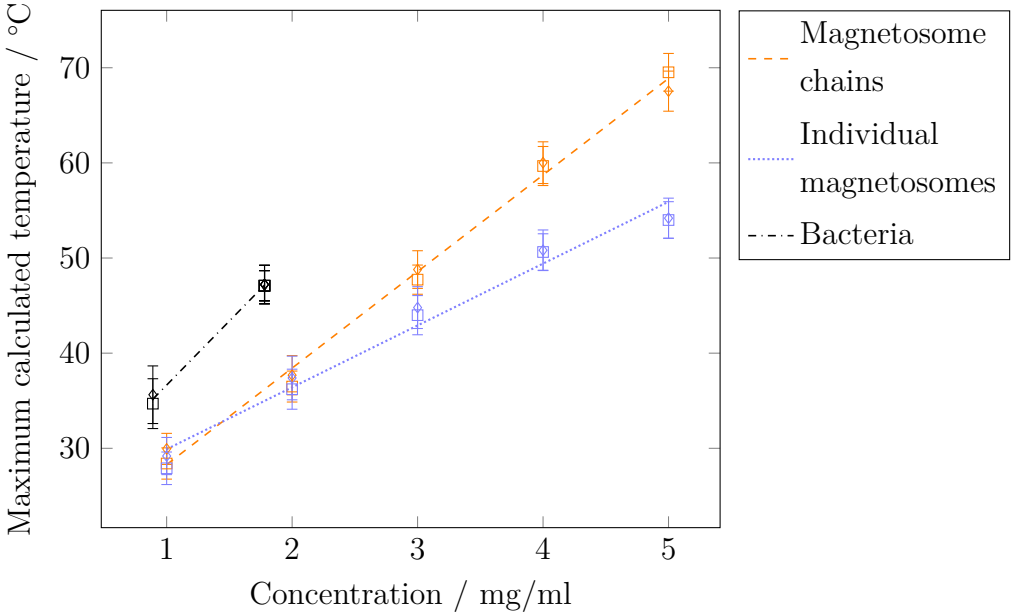

(a) Calculated maximum temperature from the fit data for heating and cooling curves (Equation (2.23)), dependent on the conformation.

	Slope/°C ml/mg	Vertical intercept / °C
Magnetosomes	10.14 ± 0.65	18.1 ± 2.1
Denaturated Magnetosomes	6.50 ± 0.83	23.4 ± 2.8
Bacteria	13.4 ± 2.3	23.1 ± 3.3

(b) Fit parameters from the linear fit with fit errors.

Figure 4.34: Maximum temperature conformation dependence. Values are calculated using the fit for heating and cooling (Equation (2.23)). The linear fit is done for each dataset individually. The particles were measured at 93.75 kHz.

In Figure 4.34, the temperature depending on the magnetosome conformation and iron concentration is given. It is evident that the earlier the stage of the magnetosome extraction, the higher the heating capacity. This is potentially caused by the increased magnetic moment, which originates from the magnetosomes aligning in chains. While for magnetosome chains and individual magnetosomes, the concentration can be chosen, the concentration of the bacteria samples is limited in its adjustable range. As a result, it is only possible to measure the bacteria sample for concentrations of 1.78 mg/ml 0.89 mg/ml, where the latter is diluted from the first.

4.3.6 Cooling Influences of the Sample Temperature

As discussed in Section 4.1.7, the ambient temperature is a crucial factor in the heating process. Since it is not possible to run the hyperthermia setup without cooling, without risking damage to the setup, 5 °C cooling water has been used for all measurements, which have been presented up to this point. Since the needed cooling capacity of the magnet changes during the measurement, the constant cooling water temperature leads to a change in the ambient temperature of the sample. However, the model used to describe the heating process is unsuitable to accommodate a changing ambient temperature; therefore, it does not represent the heating and cooling constants correctly. As the time constants are mainly influenced by the slope of the data, it is attempted to stabilize the temperature of the magnet faces. To achieve this challenging goal, a purpose build switch has been implemented as described in Section 4.1.7.

The resulting change in magnet face temperature has been shown in Figure 4.16 for continuous 5 °C cooling and for switched cooling. Switched means that the cooling water temperature is at 5 °C while the AMF is in operation and at 20 °C while the AMF is not in operation. The use of 20 °C water is required because of the water inside the cooling lines, which would provide cooling, even if not actively exchanged, due to the heat capacity of water. While the features of the magnet face temperature are shown in Section 4.1.7, the resulting sample temperatures are discussed here.

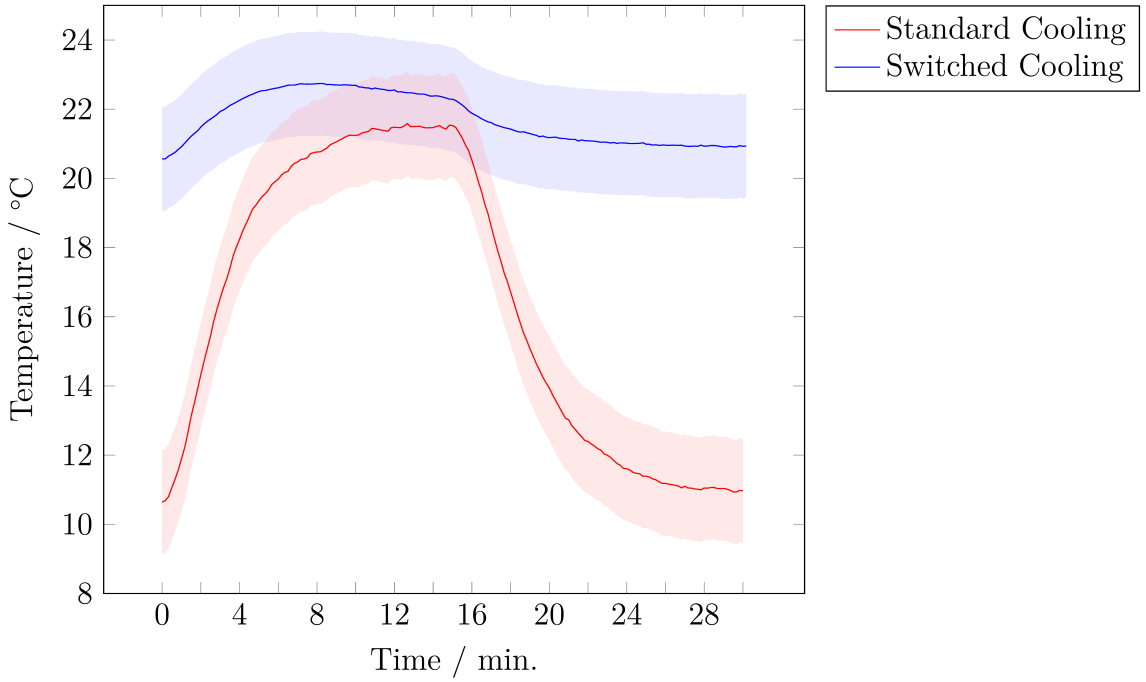

Figure 4.35: Temperature reached in a pure water sample for different cooling setups. Standard cooling is continuous cooling with 5 °C water, switched cooling is 5 °C during AMF operation and 20 °C otherwise. The shaded area represents the error.

In Figure 4.35, the sample temperature for a pure water sample is shown. The temperature for the standard cooling shows a change of $\sim 11\,°C$; in contrast, the sample temperature shows a change of only $\sim 2\,°C$ for the switched cooling. The slight change during the AMF period is in agreement with the change of the magnet face temperature during a measurement cycle.

The effectiveness of the switched cooling approach is verified by comparing the temporal temperature evolution to measurements with constant cooling water temperatures of 5 °C and 20 °C. The maximum temperature reached during the application of the AMF is in accordance with the temperature reached in the standard cooling measurements, while the start-end temperatures are in line with the temperatures for an uncooled magnet. Uncooled, in this case, means that the cooling water supplied is at room temperature (20 °C), as the total lack of cooling poses the risk of damaging the setup. However, cooling with room temperature water does not give rise to any temperature difference to an uncooled magnet in the absence of an AMF while limiting the magnet temperature to nondestructive levels. The results are shown in Figure 4.36.

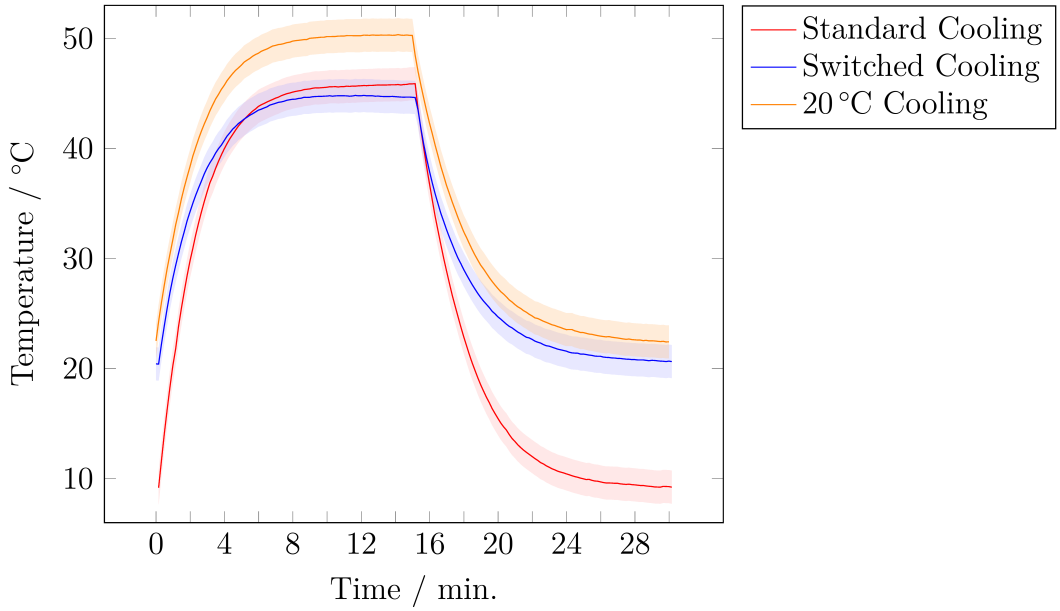

(a) Temperature evolution for Synomag® 70 particles at 5mg/ml, for different types of cooling water supply.

	τ_H / s	τ_C / s
Standard Cooling	(126.9 ± 1.8) s	(170.0 ± 2.6) s
Switched Cooling	(127.3 ± 1.3) s	(161.2 ± 1.2) s
20 °C Cooling	(134.8 ± 2.7) s	(177.4 ± 3.4) s

(b) Heating and cooling time constants extracted from fitting Equation (2.20) and Equation (2.22).

Figure 4.36: Temperature reached in a Synomag® 70 sample at a concentration of 5 mg/ml for different cooling setups. Standard cooling is continuous cooling with 5 °C water, switched cooling is 5 °C during AMF operation and 20 °C otherwise. 20 °C cooling is constant at the given temperature. The shaded area represents the error. The particles were measured at 93.75 kHz.

From Figure 4.36a, it is visible that the resulting heating and cooling curves will have a different heating constant τ for each curve. This is due to the different temperature changes in the same time span. Figure 4.36b contains the heating and cooling constants for the curves depicted in Figure 4.36a.

One approach to determine more precise heating and cooling constants is the subtraction of the magnet influence. This influence is determined by the measurement of ultra-pure water. In Figure 4.37a, the heating and cooling constants are shown for the measurements conducted without the subtraction of the ultra-pure water background

measurement. By comparing these values to the heating and cooling constants with the influence of the AMF on pure water being subtracted, shown in Figure 4.37b, it is visible that the constants lower for concentrations of 2 to 5 mg/mL.

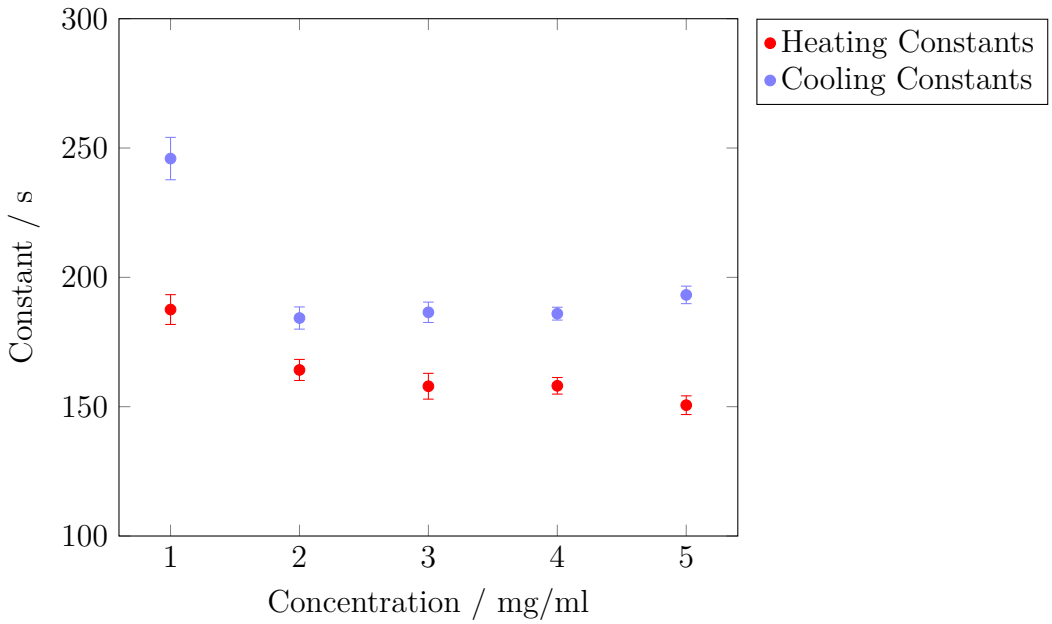

(a) Heating/cooling constant τ for measurements with continuous 5 °C water cooling.

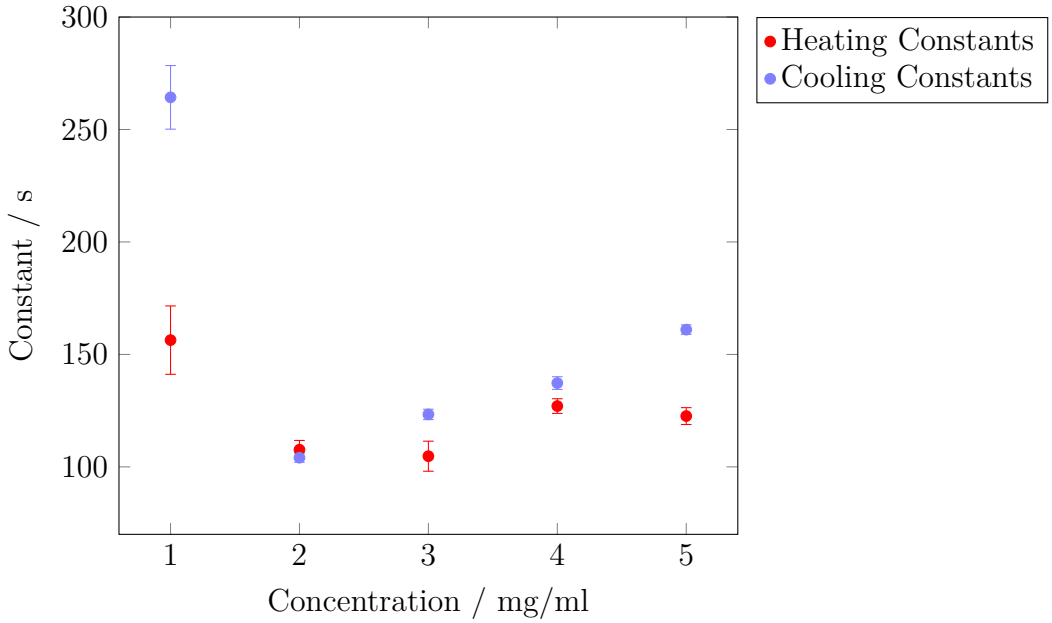

(b) Heating/cooling constant τ for measurements with continuous 5 °C water cooling, corrected with a water background measurement.

Figure 4.37: Comparison of the heating and cooling constants if a background measurement is subtracted before fitting Equation (2.20) or Equation (2.22). The particles were measured at 98.10 kHz, the water reference is measured at 93.75 kHz.

The use of background or reference measurements is common practice in all fields of science and engineering. While it does give the opportunity to measure the heating/-cooling constants for bulk samples, it does not pose a solution to overcome the sample temperature changes for biomedical samples as the temperature needs to be kept in the physiological range to assure that the sample is not influenced by hypothermia. Another weakness of comparing two different measurements with each other is the absolute temperature accuracy of the camera, which is at $\pm 1.5\,\mathrm{K}$. This offset error limits the resolution for low concentrations. This is a possible cause of the irregular change in constants for a concentration of 1 mg/mL. The difference in measurement frequencies does not represent a limitation in the interpretability since the heating of the water sample is solely caused by the temperature rise of the magnet.

The presented approach of switching the cooling water temperature according to the cooling need of the system represents the possibility of overcoming the problem of hypothermia under consideration of biomedical samples. Comparing the heating and cooling constants for the concentration of 5 mg/mL for water subtraction evaluation (index H/C,W) and for the direct switched cooling (index H/C,S)measurement gives values of $\tau_{\mathrm{H,S}} = (127.3 \pm 1.3)\,\mathrm{s}$ and $\tau_{\mathrm{C,S}} = (161.2 \pm 1.2)\,\mathrm{s}$ for the switched cooling and $\tau_{\mathrm{H,W}} = (123.6 \pm 3.8)\,\mathrm{s}$ and $\tau_{\mathrm{C,W}} = (161.0 \pm 2.2)\,\mathrm{s}$. The alignment of the respective heating/cooling constants shows that the use of the cooling switching system is able to diminish the influence of the magnet on the sample.

4.3.7 Fast Heating/Cooling Cycles

One of the biggest advantages of magnetic hyperthermia is the temporal precision with which the heat generation can be controlled. To study the influence of temperature changes on biomedical samples, it is favorable to be able to subdue the sample to reoccurring temperature changes. To be able to do so, the setup needs to be capable of applying the AMF over a prolonged period of time.

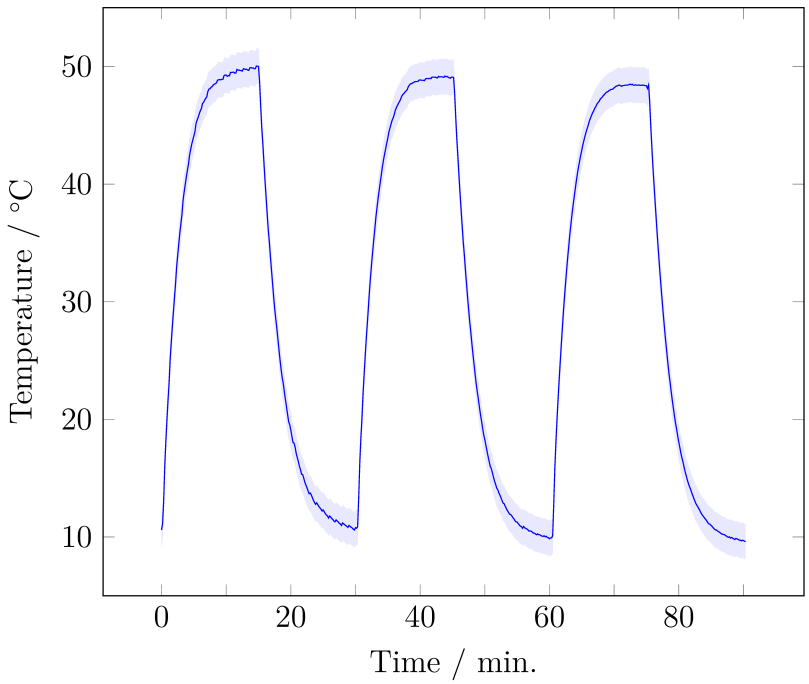

Figure 4.38: Three consecutive measurement cycles, each reaching thermal equilibrium in the heating/cooling period. All measurement cycles consist of 15 min heating followed by 15 min of cooling. The particles were measured at 93.75 kHz.

In Figure 4.38, it is shown that the setup is capable of heating the sample to a steady state, with multiple cycles back to back. While this is clear evidence of the robustness of the setup, the slow cycles and the large temperature range do not represent a suitable use case for biomedical applications due to the aforementioned potential sensitivity of samples to temperatures outside the physiological range.

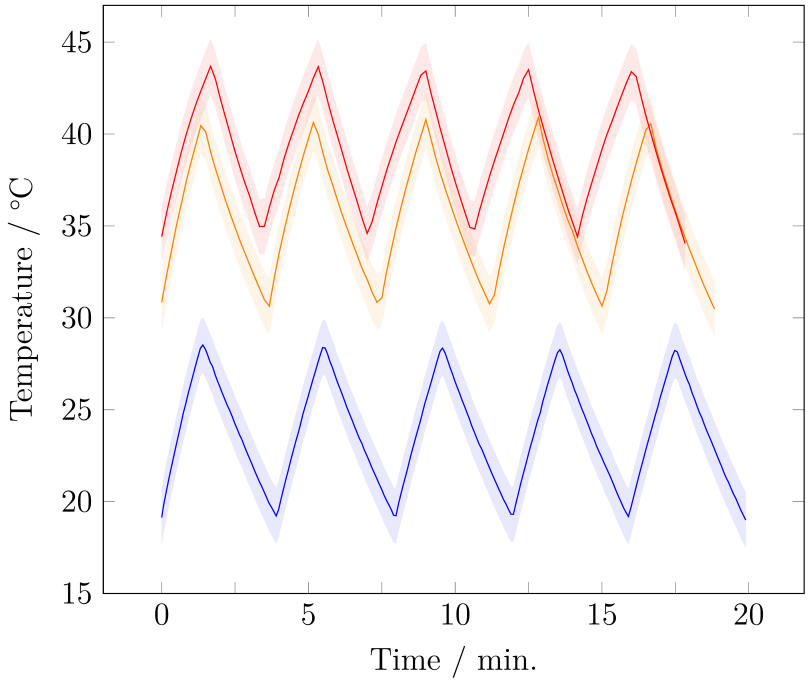

Figure 4.39: Fast heating and cooling cycles of Synomag® 70 particles at 5 mg/ml. Each color represents a cycle covering a different temperature range. The particles were measured at 93.75 kHz.

In Figure 4.39, faster heating-cooling cycles are shown. The shown curves are measured for a particle concentration of 5 mg/ml Synomag® 70 , and show the wide range of possible temperatures for fast heating cooling cycles with an amplitude of 10 °C.

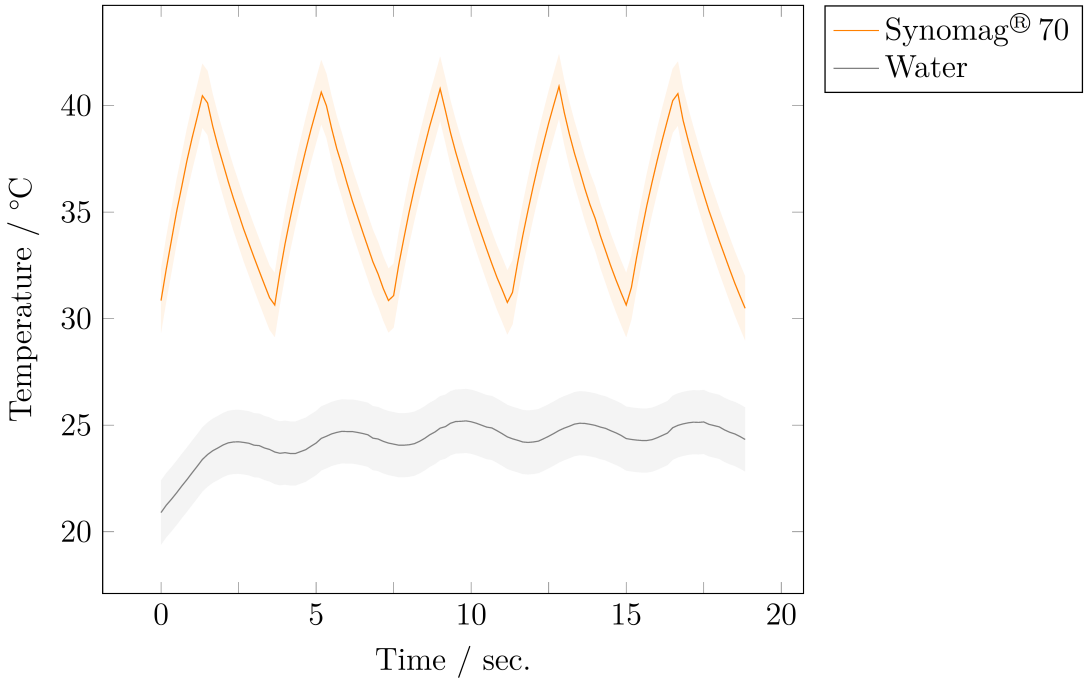

Figure 4.40: Fast heating and cooling cycles of Synomag particles (5 mg/ml) compared to water subjected to the same temporal AMF. The particles were measured at 93.75 kHz.

In Figure 4.40, the temporal temperature evolution of a 5 mg/ml Synomag® 70 sample in comparison to a water sample is shown. Here it is visible that the temperature change caused by the inductive heating of the nanoparticles in a fast switching AMF is ∼15 °C higher than the heating caused by the magnet.

4.3.8 Microscopable Samples Containers

All measurements shown until now were performed on bulk nanoparticle samples in solution. For biomedical samples, it is of major interest to image the behavior of cells in interaction with magnetic nanoparticles while being subjected to the AMF. For this purpose, the magnet setup has been fitted with a custom-built microscope setup. To be able to perform microscopy imaging on a sample, special containers are used. In the following, the usability of these containers for hyperthermia measurements is investigated. In Figure 4.41, a visual representation of the positioning of the microscope-able microfluidic channel is given.

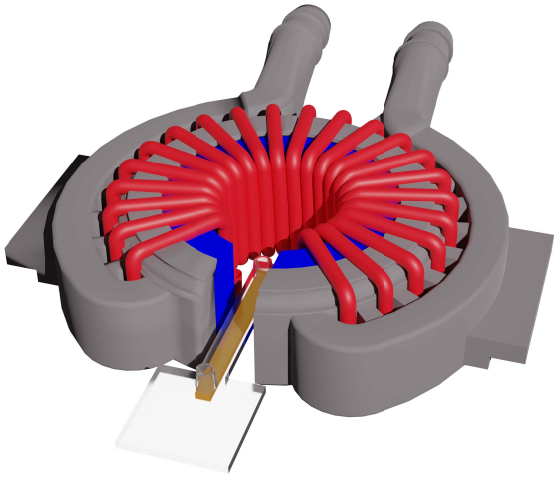

Figure 4.41: Rendered image of the positioning of the microscopy slide inside the electromagnet gap. The width of the gap is 1 cm, and the width of the channel inside the gap is 8 mm.

In Figure 4.42, the temporal temperature evolution of Synomag® 70 and water inside a microscopable microchannel is shown. Of special note is that the temperature measured in this case is not the surface temperature of the fluid itself but the upper cover of the microfluidic channel. Due to the cover between the sample fluid and the camera, the resulting temperature is not usable to determine the absolute temperature reached in the sample. Still, a heating effect can be seen.

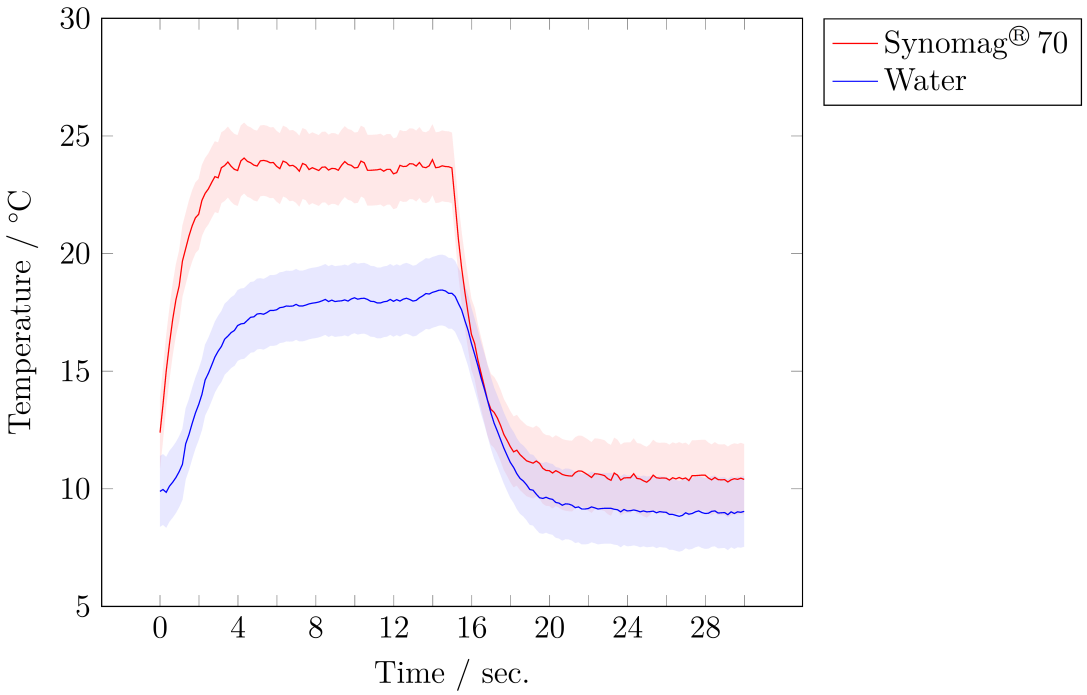

Figure 4.42: Temperature evolution of pure water and Synomag® 70 at 5 mg/ml inside a microscopable microfluidic channel. Measurement errors are shown as shaded areas. The particles were measured at 93.75 kHz.

Since the microchannels are larger than the magnet gap, the spatial heating distribution is of interest. Due to the microchannel housing covering the sample surface, the temperature differences are difficult to see in a thermography image. Therefore Figure 4.43 shows the differences between a channel filled with water and a channel filled with Synomag® 70 at a concentration of 5 mg/ml.

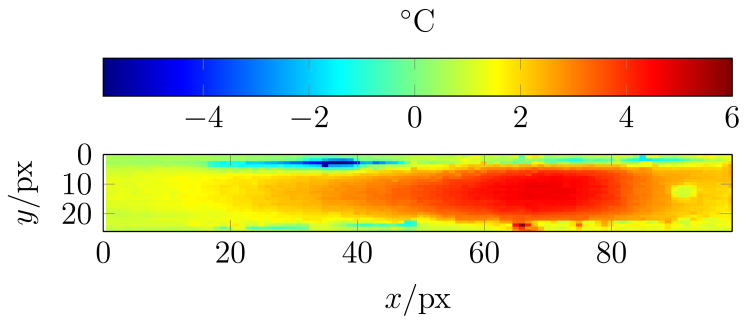

Figure 4.43: Temperature difference of a microscopy channel filed with water and filled with Synomag® 70 at a concentration of 5 mg/ml. The overall width along the y-axis is ∼ 8 mm. The magnet is right and left of the channel at ∼ 55 to ∼ 85 pixel. The particles were measured at 93.75 kHz.

The bright spot at the right side of the image (∼pixel 90) is the filling nozzle of

the channel. The visible correlation of applied AMF and temperature increase in a microscopable sample proves the possibility of observing samples subjected to an AMF with the used microscope inside the here inspected channel slides.

5 Discussion & Conclusion

The goal of this project is to develop a versatile, low-cost magnetic hyperthermia setup that is capable of maintaining a high frequency alternating magnetic field in the order of tens of millitesla over a extended time interval, which is sufficient to reach a steady temperature. Additionally, it needs to be possible to mount the setup onto a microscope, to enable the live imaging of *invitro* samples being subjected to the AMF.

As a basis, a resonant transformer is chosen.

Three different core materials have been tested with regard to their coupling factor. All investigated cores show a coupling factor well above 97 %, with the N87 core exhibiting the best coupling at 98.5 %, thus limiting energy losses.

In the circuitry, two types of wire are examined. The first is a stranded wire the second is a specialized Litz wire. It has been shown that while the ohmic resistance is comparable, the coupling factor is significantly different for the wires, thus leading to the use of specialized Litz wire in the setup.

The capacitors have been chosen based on ease of use. This approach has led to an easily adaptable capacitor array that does not need any active cooling while showing linear behavior in the range of applications.

The heat generated, which would limit the field amplitude as well as the operation time, is dissipated via a custom water cooling system. This system consists of a 3D-printed cooling shell for the magnet enabling direct contact of cooling water and magnet core, thus creating the best possible thermal connection. With its two modes of operation, it is not only proven to be able to limit the maximum temperature of the magnet to room temperature during operation. Still, it is also capable of keeping the magnet temperature constant within the range of $(21 \pm 1)\,°C$ during the whole measurement duration. The possibility of keeping the setup temperature constant is especially important if biomedical samples are to be examined, which are sensitive to low temperatures. Due to the elaborated cooling, it is possible to maintain a magnetic field strength of 48 mT within a working volume of $2\,cm^3$ at a frequency in the 100 kHz regime. While it is comparably easy to achieve magnetic fields of this magnitude, it has been proven that

the proposed setup is capable of maintaining the field over a period longer than the time it takes the sample temperature to reach a steady state (15 min). In addition to the upper limit of temperature, the possibility of keeping the magnet temperature constant over the whole measurement time has also been shown.

By comparing the achieved parameters to other recent works, it is visible that the built setup represents a reasonable base to combine several aspects that have been shown before. With a frequency of about 100 kHz, our setup is situated at the lower end of the frequency range of built setups, which is from 100 kHz to 500 kHz [57]. Due to the combination of a resonant transformer and broadband amplifier, the working frequency can be adjusted by altering the inductance array.

The gap size of 10 mm is at the upper end of demonstrated gap sizes ranging from 400 µm [72] to 11 mm [73]. The magnetic field strength of 48 mT can be maintained for a period of 20 min. In Table 5.1 the gap size, magnetic flux density, and operational time is shown for different setups. By comparing these values, it is evident that there is often a trade-off between these characterizing parameters. In the scope of this project each component has been thoroughly tested to maximize the overall efficiency. The setup has been designed towards the generation of sufficiently strong high frequency fields for biomedical experiments. As a result the reported setup represents a hightech solution at the edge of what is feasible.

Gap Size/mm	Max. Magnetic Flux Density/mT	Frequency/kHz	Operational Time / min.	Reference
10	48	93.75	20	This work
7.5	88 30	100 500	0.25 0.5	[57]
0.37	~ 53	300	120	[72]
11	29 (15.5)	NA	15	[73]
20×15 (air coil)	43.9 27.6	149 >1000	NA	[74]

Table 5.1: Comparison of magnet parameters from different works on magnetic hyperthermia. Flux density values in parentheses are values achieved during measurements, if different from maximum achievable value.

In the scope of this work, three structurally different nanoparticles have been studied concerning the usability in hyperthermia. Here, different substructures could be observed in TEM images, showing nanoflower substructures for Synomag® 70 , parallelepiped shapes for BNF, and cubooctahedral shapes for magnetosomes. For usability in biomedical applications, especially the Stokes diameter and the surface charge are of interest. These have been investigated for all of the particles. All diameters found are comparable with previously reported sizes [67, 75]. For all three particles, the heating power has been investigated, reaching temperatures of up to 70 °C for magnetosomes.

Aside from being able to heat the sample until a steady state temperature is reached, the setup also has been proven to be able to subject samples to heating/cooling cycles, with a period of about 4 min. The ability to produce fast cycles enables the investigation of interval application of localized heat. Thereby the reached temperature range can be adjusted using the cooling system. The interval range enables the setup for the influencing of thermo-responsive peptides [26, 76, 77], and influencing biological signaling [20, 21, 78].

In summary, the setup developed in this project fulfills the requirements set. It represents a simple approach to a well-rounded hyperthermia setup, enabling the imaging of samples subjected to an AMF. In addition, the elaborate cooling system enables steady operation over prolonged periods of time while keeping the magnet temperature constant, thus reducing the thermal strain on a sample. The presented properties show the high potential of the proposed setup to open opportunities in the field of biomedical assays as well as for biosensor applications in nanotechnology.

II

Single-Particle Tracking

6 Introduction

For most everyday interactions, the individual tracking of objects is inevitable. In microscopy, however, the individual tracking of nano-scale objects remained an unsolved challenge until the 1980s. In 1987 gold nanoparticles were used to track cell behavior [79]. From this starting point, the labeling of nano- to microscale objects became a powerful approach to trace the behavior of individual objects, and learn about their (biological) function. Today the most prominent particle labels are fluorescent probes. These probes are of different origins, like quantum dots [80], synthetic dyes [81], and fluorescent proteins [82]. Here the discovery of fluorescent proteins is of special notice, as it is possible to encode them into a plasmid, thus making a cell automatically produce labeled molecules. This is especially important as many dies are toxic to living cells. Due to the high amount of specific markers that have been developed, it is possible to target various biological molecules. These include but are not limited to: Proteins [83, 84], DNA strands [85] and, mRNA [86]. A problem shared by all these markers, although to a different extent, is bleaching.

Based on single molecule tracking, numerous advances in biology were made, since this technique allowed to decipher the spatio-temporal dynamics of numerous subcellular processes [87]. Two prominent discoveries made by single particle tracking experiments could only be made with single particle tracking and underline the importance of this technique. The first is that diffusion inside cells is anomalous [88, 89, 90]. The second discovery is that processes in cells are nonergodic [91, 92]. This discovery is especially important as ergodicity is often assumed in statistical physics. Single-molecule tracking avoids ensemble averaging and thus does not rely on ergodicity. Due to the lack of ensemble averaging also, spatial information is maintained.

Today the labels and microscopes have been improved to a level where tracking with sub-nanometer resolution in three dimensions is possible [93]. On the imaging side, cameras have advanced, enabling frame rates of 100 Hz and above. The evaluation algorithms have been improved to a point where the simultaneous tracking of multiple particles is possible [94]. These advances, however, come at the cost of high volumes of data that need to be saved and evaluated.

6.1 Outline of this Project

This project focuses on a specific problem that arises if a particle changes its motion behavior in a track. Here it is of interest to separate the track into the different types of motion before conducting further analysis. In this work, an approach based on the visual impression is chosen. For this reason, a parameterization is developed. Based on this parameterization and simulated reference tracks, the track is separated.

The seventh chapter introduces the theoretical basics of the mean squared displacement and fluorescence.

The eighth chapter describes the fluorescence setup, which is based on an inverse fluorescence microscope used for the tracking recordings. Additionally, the tracking algorithm used is described.

In the ninth chapter, the developed algorithm is discussed. At first, the main script is introduced. Afterwards, the subroutines are reviewed. The review of subroutines is done in alphabetical order in order to enable the use as a lexicon. At the end of the ninth chapter, the algorithm is tested on actual tracking data of endosomes, and the assignment of motion type is compared to the results from mean square displacement theory.

In the tenth chapter, the overall performance is discussed.

6.2 Contributions and Publications

This project has been conducted in the group for Experimental Medical Physics. As the research is interdisciplinary, I have worked in close collaboration with other group members. Additionally, I have supervised several students during their thesis.

6.2.1 Contributions to this Thesis

- Paolino Salamone has measured the endosome tracks and performed the tracking using u-Track. Additionally, he provided the script for plotting the tracks color-coded atop the cell image.

6.2.2 Publications

Parts of this work have been published in posters on different occasions.

- Poster at DPG Frühjahrstagung Regensburg 2022: *Single Molecule Tracking of Molecular Motors under Different Physiological Conditions*
  Authors: Lentz, Adrian; Blair, Paulina; Kuckla, Daniel; Hagemann, Philipp; Monzel, Cornelia.

Parts of this project are also included in supervised bachelor and master theses and cooperative works.

- Christina Siepe: *Einzelpartikelverfolgung in Zellen* (Bachelor Thesis)
- Anton Sinner: *Single Molecule Tracking* (Bachelor Thesis)
- Adrian Lentz: *Einzelpartikelverfolgung von molekularen Motorproteinen - Mit Fokus auf die Motordynamik Klassifizierung* (Bachelor Thesis)
- Paulina Blair: *Single-Molecule Tracking - Approaches to Kif5C imaging and dynamic analysis* (Bachelor Thesis)

7 Theoretical Basics

In this chapter, the underlying principles of **S**ingle **P**article **T**racking (SPT) experiments will be explained. At first, the motion of microscopic particles in a non-solid medium will be discussed. Afterwards, the principle of fluorescence is explained, which is the basis of fluorescence microscopy.

7.1 Mean Squared Displacement

If the inertial force is negligible microscopic objects are moved by random forces originating from the surrounding media even in the absence of flow. The resulting behavior is called Brownian motion after Robert Brown, who is credited with the discovery of this effect by observing pollen in water [95]. Some of the pollen showed movements that were not explainable by the flow in the surrounding water. Just like all molecules above absolute zero temperature, the observed particles and the surrounding molecules hold thermal energy, which is partially converted to kinetic energy, causing the particles to be in constant motion. The motions observed by Brown are caused by the collisions of observed particles and the dispersion of medium molecules. The erratic character of the movements with random direction changes is therefore influenced by the temperature of the sample. This problem has been addressed by Albert Einstein [96, 97], Marian von Smoluchowski [98] and Paul Langevin [99].

A measure to describe the movement is the **M**ean **S**quared **D**isplacement (MSD). The MSD is defined as

$$MSD(\Delta t) = \left\langle x^2(\Delta t) \right\rangle = \left\langle (x(t+\Delta t) - x(t))^2 \right\rangle,$$

with $x(t)$ the position of a particle at a time t and the time difference Δt, for which the displacement is calculated. For a track of temporal steps with corresponding coordinates of a particle, this can be rewritten to

$$MSD(n\tau) = \frac{1}{N-n} \sum_{m=0}^{N-n} \left(x\left(m\tau\right) - x\left(\left(n+m\right)\tau\right) \right)^2,$$

with the length of the track N and the step duration τ. The time difference Δt can only be a multiple of τ and is parameterized by m. The MSD is often understood to be the area a particle explores within a certain time interval. While this is an intuitive and valid explanation for pure Brownian motion, one needs to remember that this is not always true for all observed particles. Deviation from this intuitive understanding arises if the motion type of the particle is not entirely random. If a particle is influenced by a flow or other means of transport, the transport causes a linear motion which is superimposed by the Brownian motion. In this case, the motion path is a widened line; therefore, the area described by the MSD is much larger than the area actually covered by the motion. Another example is a particle in a circular motion which will have a reduced MSD for all temporal intervals that are close to the time it takes the particle to complete one or multiple full circles. Another example is a particle moving in a straight line, where the actually explored area is much smaller than the MSD.

For a moving particle, the MSD is time-dependent. A basic approach to describe a time-dependent property is

$$f(t) = a \cdot t^b + c, \tag{7.1}$$

where a, b and c are arbitrary factors. These factors carry information about the type of motion which is observed. Since the factors are not time-dependent, this approach is only viable if the type of motion does not change. When investigating the motion, there are distinctive types of motions that take a special role.

The probably best-known type of motion is linear motion. For a strictly linear motion, the displacement can be calculated by

$$d = v\Delta t,$$

with the velocity of the particle v and the time period Δt. The squared displacement for any step width is then given by

$$MSD = v^2\Delta t^2.$$

Compared with Equation (7.1) this is the case with $a = v^2$, $b = 2$, and $c = 0$.

A different type of motion that is often observed in single particle tracking is Brownian motion. Brownian motion is described by the Langevin equation, which describes the evolution of a system where the forces acting on the system can be assigned to be either deterministic or random. The Langevin equation for Brownian motion in one

dimension is given by

$$m\frac{\mathrm{d}v}{\mathrm{d}t} = -\xi v + \eta\left(t\right),$$

with the mass of the particle m, the velocity of the particle v, the drag coefficient ξ, and a random force η. $\eta\left(t\right)$ is a random white noise-like force with a mean of zero

$$\langle \eta\left(t\right) \rangle = 0.$$

The random noise is also required to have a correlation function of the form.

$$\langle \eta\left(t\right) \eta\left(t+\Delta t\right) \rangle = C \cdot \delta\left(\left(t+\Delta t\right) - t\right),$$

where δ is the Dirac delta function and C is a constant. The solution to this formula is given by

$$v\left(t\right) = v\left(0\right) \mathrm{e}^{-\frac{\xi}{m}t} + \frac{1}{m}\int_0^t \eta(s)\mathrm{e}^{-\frac{\xi}{m}(t-t_1)}\mathrm{d}t_1. \tag{7.2}$$

Based on Equation (7.2) an expression for $x(t)$ can be derived (Appendix B.2), which leads to

$$\left\langle x\left(t\right)^2 \right\rangle_t = 2Dt,$$

with the diffusion constant D. This expression is derived from the one-dimensional Langevin equation. As the motion along different dimensions is independent of each other, the displacement generated linearly scales with the amount of dimensions n, finally leading to

$$\left\langle x\left(t\right)^2 \right\rangle = 2nDt. \tag{7.3}$$

Compared to Equation (7.1), this is, for the two-dimensional case ($n = 2$), with $a = 2nD = 4D$, $b = 1$, and $c = 0$.

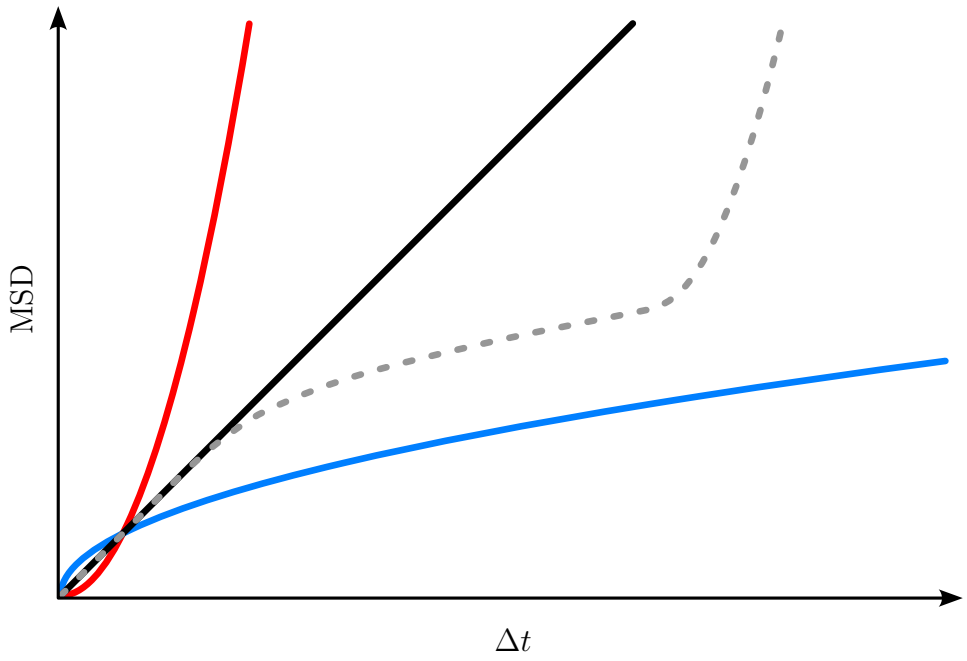

Figure 7.1: MSD for different types of motion. Linear motion (red, $MSD \propto t^2$), diffusive motion (black, $MSD \propto t^1$) and subdiffusive motion (blue, $MSD \propto t^{0.5}$). Additionally shown is a graph for non-uniform motion in gray.

Due to the different evolution of the MSD, it is possible to use the characteristic shape to determine the motion behavior of a particle. In Figure 7.1, exemplary MSD curves are shown. Of special notice is the region for $\Delta t < 1$, as the MSD increases faster for diffusive motion than for directed motion. This is an artifact of the chosen model. For two particles moving at the same speed, the displacement is at its maximum for linear motion. This is due to the fact that the shortest connection between two points is a straight line. Vice versa, this principle shows that with a finite path length, the furthest distance between the start and end is a straight line.

This description of the MSD is commonly used [100]. There are, however, shortcomings that need to be kept in mind. A method often used for visual representation is the α-D-map. Here the exponent is denoted with α. Since the unit for the mean squared displacement is m^2, a changing exponent requires changing units in the prefactor. Thus the illustration in an α-D-map compares numerical values that have different units. Nevertheless, a higher D value indicates a faster-moving particle, and a straighter track is indicated by a higher value of α, thus although comparing values with different units, the α-D-map is an intuitive way to gain an overview of the movement present in a sample.

7.2 Fluorescence

Fluorescence is a type of radiation emission during the relaxation process of excited electrons. If light is shone onto an object capable of fluorescence, an electron can be excited into a higher state. For this to happen, two criteria must be met. The first is the match of energy supplied by the impinging photon and the energy difference between the two system states. The second is the overlap of the wave functions of the energy states in question. These prerequisites are given by the Franck-Condon principle [101][8], which can be visualized by an energy diagram similar to the often used Jabłoński diagram. While the Jabłoński diagram only addresses the energy differences of the possible states, the diagram shown in Figure 7.2 also includes the wave functions.

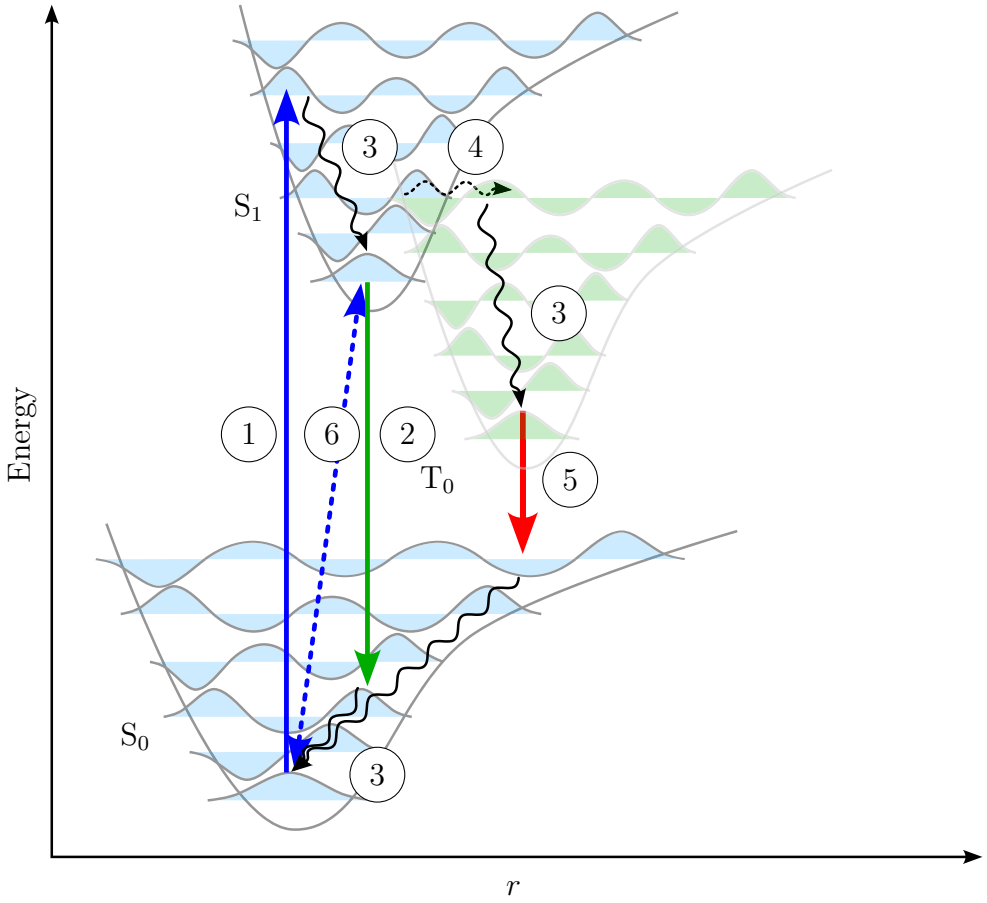

Figure 7.2: Exemplary energy levels for the illustration of fluorescence. Shown are the singlet ground state S_0, the triplet ground state T_0, and the first excited singlet state S_1. For each state, the additional vibrational states are shown with an indicated probability of presence. The arrows indicate absorption (1), fluorescence (2), internal conversion (3), inter-system crossing (4), phosphorescence (5), and suppressed transitions (6). On the x-axis, the spatial coordinate is given.

[8] The principle is named after James Franck and Edward Uhler Condon [101].

Shown are two singlet states, the ground state S_0 and the first excited singlet state S_1. They are represented by the potential well with the corresponding vibrational levels. Additionally, the triplet ground state T_0 is given. The necessary overlap of the wave functions can here be understood visually. If the wave functions are perfectly spatially overlapping, an arrow indicating the transition would be vertical. If an arrow indicating the transition is tilted, the transition is suppressed; however not completely impossible. The different transition probability, in combination with the different energies needed, results in a continuous spectrum of energies that can be absorbed. After the absorption process, the electron can relax via internal energy conversion into the lowest vibrational state in the excited electronic state. From this state, the only possible relaxation is via the emission of an electron into the ground state S_0. For this transition, the wave function overlap of the vibrational ground state of S_1 and any vibrational state of S_0 causes a possible transition. If the vibrational level of S_0 is not the lowest, the electron can relax to the ground state via internal energy conversion. Until now, the triplet state has not been taken into consideration. If an electron is in an excited state and there is an overlap with a triplet state, the electron can undergo inter-system crossing[9]. In the triplet state, the electron can relax into the lowest vibrational state. The energetically lower states are now singlet states. The relaxation into a state with different spin multiplicity, however, is forbidden by the selection rules. A forbidden transition does not indicate an impossible transition but a transition that is far less likely to occur. The process of relaxation from a triplet state into a singlet state is called phosphorescence. Due to the different types of transition of phosphorescence, fluorescence, and internal conversion, the processes occur on different timescales. The fastest process is internal conversion, with a lifetime of tens of femtoseconds, followed by fluorescence, with a lifetime of nanoseconds. The slowest process is phosphorescence, with a lifetime of microseconds up to several seconds [103]. While fluorescence is only observable while excitation the fluorophore is illuminated, phosphorescence can occur long after the excitation light has been removed. This process is often used in safety signs.

Until now, only the energy differences in the electron states have been discussed. Concerning the absorption, the energy is provided by a photon of the excitation light[10]. As visible in Figure 7.2, the electron dissipates energy by internal conversion in the S_1 state as well as after the emission of the photon in the S_0 state to reach the lowest vibrational state. The dissipated energy is consequently not available for the emitted

[9] Under certain conditions, it is also possible for an electron to perform reversed inter-system crossing from a triplet state to a singlet state where the electron relaxes via fluorescence. This process is called delayed fluorescence and is used in organic light-emitting diodes. [102]

[10] There are also processes involving multiple photons, e.g. two-photon absorption in dyes [104].

photon. The energy E_{ph} of a single photon is given by

$$E_{\mathrm{ph}} = \frac{hc}{\lambda}$$

with the Plank constant h, the speed of light c and the wavelength of the photon λ. In combination with the energy difference, due to internal conversion, this results in a wavelength shift between the absorbed photon and emitted photon. This effect is called Stokes shift and enables the imaging process described in Section 8.1.

8 Microscopy Setup and Tracking Software

The goal of this chapter is to introduce the adapted fluorescence microscope setup, as well as the tracking software u-Track, which is used for the tracking of the particles.

8.1 Fluorescence Microscope

As described in Section 7.2, the light emitted by a fluorophore has a longer wavelength than the absorbed light due to the Stokes shift. This wavelength difference is exploited in Fluorescence microscopy, which was discovered by accident in 1904 [105]. The imaging is done with a fluorophore-specific set of two optical filters. The first is the excitation filter which limits the bandwidth of the excitation light. This is necessary as the used light sources are mostly white light sources to be able to use one light for multiple fluorophores. In theory, it is sufficient to exclude the emission wavelength from the excitation spectrum to be able to filter out the fluorescence signal. However, the introduced limitation serves further purposes. These are, firstly, the minimization of the amount of light shone onto the sample, which prevents heating and faster deterioration. Secondly, it enables highly specific imaging of a fluorophore. Without the bandwidth limitation of the excitation light, all fluorophores with the same emission wavelength would be registered by the detector. In contrast, with filtered excitation, fluorophores with the same emission but different excitation wavelengths can be distinguished. For the emission filter, the same principle holds true since fluorophores with a shared excitation spectrum can have different emission spectra. Some specimens enable targeted labeling. In combination with dye-specific filter sets, targeted labeling gives rise to highly specific imaging of individual components.

The used setup is an adapted IX73 fluorescence microscope (Olympus, Tokyo, Japan) shown in Figure 8.1.

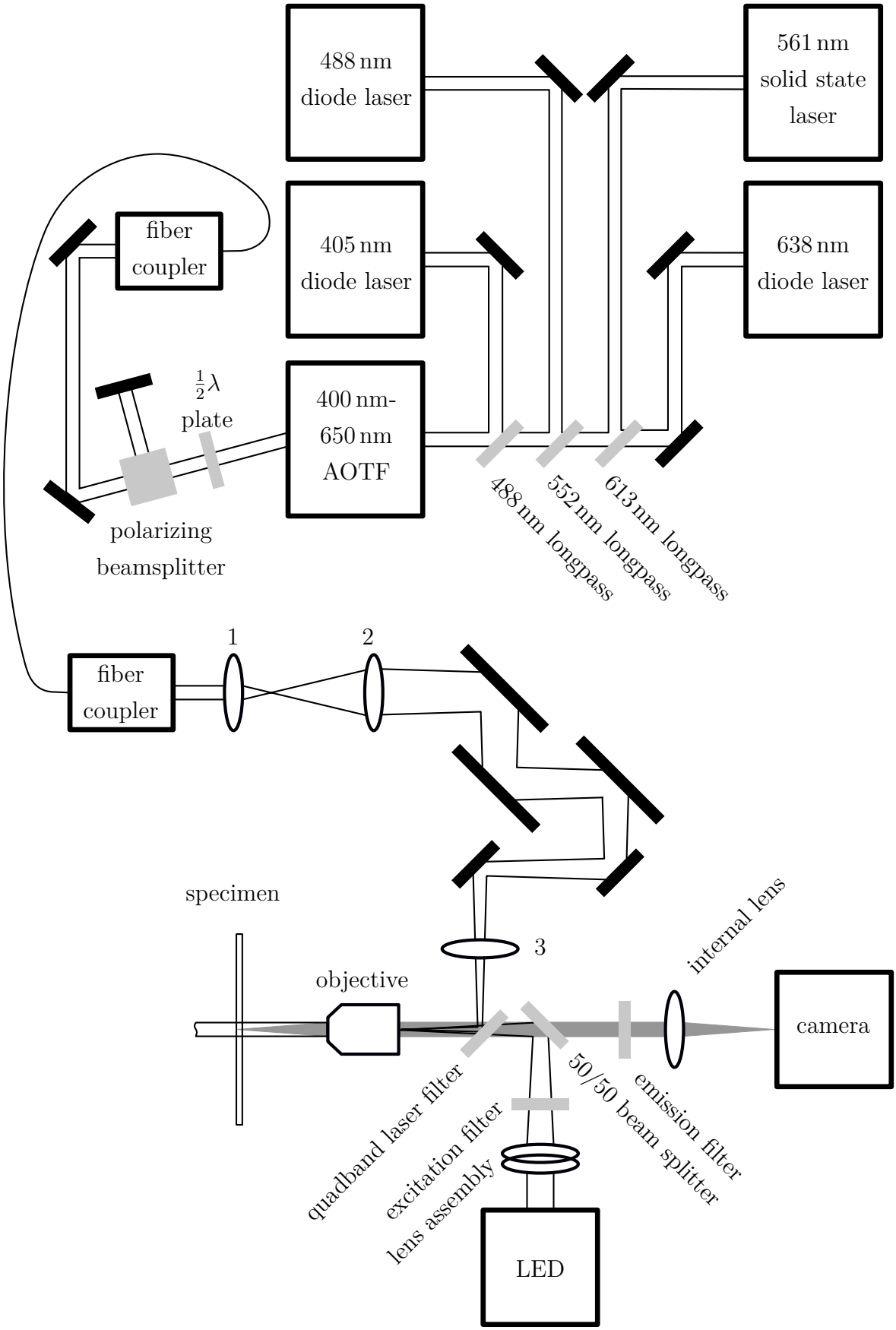

Figure 8.1: Schematic of the used fluorescence microscope. A comprehensive list of parts can be found in Table B.1

The system is equipped with two illumination methods. The first is a **L**ight **E**mitting **D**iode (LED) white light source (SolaSE2, Lumencor, Beaverton, OR, USA)[11]. This light source homogeneously illuminates the whole field of view. The light is filtered by excitation filters to match a selected fluorophore, as described before. For fluorophore-specific filter sets, the use of filter cubes that combine an excitation filter, dichroic mirror, and emission filter is common. The dichroic mirror reflects the excitation light onto the sample while transmitting the fluorescence light onto the camera. The IX73, in contrast, is equipped with a filter wheel for excitation filters and one for emission filters. Additionally, a wavelength-independent 50/50 beam splitter is used [107] in place of a dichroic mirror. While the downside of this filter setup is that $\sim 50\,\%$ of the fluorescence signal is lost, it enables maximum adaptability to different fluorophores.

The second illumination method is realized by a laser setup. The use of lasers enables higher illumination powers, which might be needed for low fluorophore concentrations, as used in single particle tracking. A drawback of this system is the limitation of excitation wavelengths; for each excitation wavelength, a different laser must be installed. In the realized setup, four lasers are used at the wavelengths of 405 nm, 488 nm, 561 nm, and 638 nm. In the first part of the setup, the lasers are aligned to share one beam path. Afterwards, an **A**cousto-**O**ptical **T**unable **F**ilter (AOTF) is used to enable wavelength-dependent transmission. The used lasers are diode lasers (405 nm, 488 nm, and 638 nm) and a solid state laser (561 nm). These lasers are most stable when used at their specified power. To overcome the fixed intensity, a half-wave plate rotates the polarization by a freely adjustable angle. The light is then guided through a polarizing beam splitter. The light intensity which is transmitted I_{trans} can be calculated by Malus's law, given by

$$I_{\text{trans}} = I_0 \cos\left(|\phi_{\text{in}} - \phi_{\text{trans}}|\right)^2 ,$$

where I_0 is the incident intensity and ϕ_{in} and ϕ_{trans} are angles between the polarization vectors of the incoming light and the transmitted light in the same coordinate system.

The intensity-adjusted beam is coupled into a single-mode optical fiber. The use of an optical fiber serves two purposes: The first is the generation of a clean **T**ransverse **E**lectro**M**agnetic modes (TEM) TEM_{00} mode. The second is achieved by rotating the polarization maintaining fiber by 45°. As a result of the rotated mounting, the polarization state of the light is partially revoked, suppressing interference, which would be visible in the image.

[11] While white light implies a continuous spectrum, this is not the case. The overlay of multiple LED emission spectra covers the wavelength needed for fluorescence microscopy, resulting in a spectrum with wavelength-dependent intensity [106].

The beam exiting the fiber is first widened by a telescope, increasing the diameter by a factor of ~ 18. The exact magnification is not determined, as the telescope does not produce a collimated beam. Hence the magnification is position dependent. This putative miss alignment is used in combination with a third lens to achieve the best possible illumination of the sample area. The need to combine a telescope with a lens is due to the limited positions of the lens. The best illumination is achieved if the backside numerical aperture of the objective is matched by the optic placed in front. For the given microscope setup, however, it is not readily achievable, as the possible positions of the last lens are limited, as well as the focal lengths for commercially available lenses. This is adjusted for by creating a lens assembly of the telescope and an additional lens shortly before the objective, which is then adjusted according to the observed illumination. The lasers are coupled into the illumination path of the microscope via a quad-band beam splitter, which reflects the wavelengths of all the used lasers, thus rendering these wavelengths unusable for detection.

8.2 Tracking Algorithm

All known imaging techniques produce temporal distinct momentary snapshots of the continuous movement of particles. The possibility to recover motion from separated images is well known from all sorts of screens like television, computer, and phones. The process of recovering motion from individual images is used in single-particle tracking. For images on screens, the tracking of motion is done by the viewer. While this is also possible for a small amount of particles, for larger amounts, automation is needed to enable efficient data acquisition. The result of the motion recovery is the track of a particle, thus the term tracking. In this project, the tracking software u-track 2.0 [108] developed by K. Jaqaman et al. [94] is used. The following explanation is a short summary of the explanation given in [94] and the corresponding supplementary info. Due to the summarizing character, the source will not be indicated again during this subsection.

The tracking process is divided into three steps. The first step is the detection of the particles in the images. For each detected particle, properties such as position and intensity are determined during this process. This is done by fitting a Gaussian kernel to local maxima. By fitting the kernel, which represents an approximation of the point spread function for a point-like object, sub-pixel localization is achieved. As a measure to increase the sensitivity for particles, there is an option to perform time averaging over several frames. The efficiency of the averaging is dependent on the particle movement. If the particle moves more than the width of the set Gaussian kernel, the image

gets blurred. After the optional averaging step, the local maxima are determined. For a pixel to be recognized as local maxima, it must show the highest intensity in a 3×3 area, and the intensity needs to be higher than 1.3 times the background standard deviation. Based on the detected local maxima, the Gaussian kernel is fitted. Even if the local maxima are determined by averaging several frames, the fitting of the Gaussian kernels is performed on each frame individually. The fitting process first tries to fit a single kernel. In the second step, a second kernel is added to the fit. The process of adding a kernel is done as long as the residuals for fitting $n+1$ kernels are smaller than the residuals for fitting n kernels. This is done to detect particles that are overshadowed by other particles.

The found maxima are then connected between different frames in a second step by minimizing the cost of the overall connection. As a measure for the connecting cost, the distance between two particle positions in two consecutive frames is chosen. To reflect the fact that the particles cannot move at arbitrarily high velocities, an upper limit for the distance $R_{\max}$ is introduced. $R_{\max}$ is the maximum of R' and R''. R' is defined as 3σ where σ is the standard deviation of the step distances found for the particle before. R'' is defined to be half the distance between the particle and the closest particle in the same frame. If the distance between two detected spots in consecutive frames is larger than $R_{\max}$, the cost is set to infinity. In biological samples with three-dimensional cells, it is inevitable that particles leave the focus plane during the measurement and therefore are not detectable anymore. The same applies to particles that have been outside the focus plane in the previous images and are now visible. The cost for linking a particle to no previous particle or for not linking a particle to a following particle is estimated by 1.05 times the maximum of all previously determined costs. In the case of linear motion, the distance between the observed position A in frame n and the observed position B in frame $n+1$ is not a good measure for the likeliness of the particle to be at the given position, as the particle is expected to have moved. To overcome this, the linking cost is no longer the distance between the observed positions but rather the distance between a detected position in frame $n+1$ and the predicted positions of the particles in frame n. The prediction of the particle positions is made by three Kalman filters. The filters cover the motion types linear forward, linear backward, and random motion. These filters allow the particle to switch between linear motion and random motion at any time during the tracking process.

The third and last step of the tracking process contains the linking of track segments which have been built in the second step. The linking is needed if the particle leaves the focal plane and is recognized in a later, non-consecutive frame. The linking is

limited by a temporal window, which describes the maximum amount of frames in which the end of one track segment and the beginning of a second track segment can be separated to be merged. In the same manner, as for the particle position linking to track segments, there is a spatial radius defined for the track start and end. The first is defined by the standard deviation of the track segments as

$$R' = 3\sigma \cdot f(\text{gap}). \tag{8.1}$$

The additional factor $f(\text{gap})$ introduces a frame distance (gap) dependent scaling of the search radius. A second radius $R''_{\text{start/end}}$ is introduced dependent on the local detection point density for the start and end point of the track, as described for the particle frame-to-frame linking. The used radius is the maximum of the two determined radii. Just as with the particles tracking from frame to frame, the possibility of not being linked is given to the track segments. In the case where directed motion is allowed, the cost for linking two directed track segments I and J is given by

$$c_{IJ} = \delta_{IJ}^2 \times \left(1 + \sin\left(\alpha_{IJ}\right)^2\right).$$

Here δ_{IJ} is the distance between the end of track I and the start of J, and α is the angle between the two tracks. To determine whether a track is linear or diffusive, the distribution of detected positions along the individual trajectories is taken into account. Additionally, the search radius for the start and end points of a track segment is altered to accommodate the different motion types. Here the detection radius is split into a short radius

$$R'_{I,\text{short}}\left(\text{gap}\right) = \sigma'_I \cdot f\left(\text{gap}\right),$$

with σ'_I the standard deviation as described before, and a long radius

$$R'_{I,\text{long}}\left(\text{gap}\right) = 3\sigma_I \cdot f\left(\text{gap}\right) + 3\sigma'_I \cdot f\left(\text{gap}\right),$$

with σ_I as the displacement standard deviation along the preferred movement direction. The final search radii for start and end are given by

$$R'_{I,\text{short}} = \max\left(R'_{I,\text{short}}, R''_{\text{start/end}}\right).$$

$R'_{I,\text{long}}$ is not adjusted as it is an expectation value for the directed motion.

In addition to the measures for a single particle track also, the possibility of track seg-

ments merging or splitting is considered. The cost for these connections is determined by the distance of a track start or end to a nearby intermediate point of another track segment. Since it is possible that tracks end or start close to another track, the cost is scaled with a required change in intensity. For all parameters mentioned, there is the possibility for the user to set bounds that are realistic for the evaluated data set. This way, the computational effort can be decreased. The used parameters can be found in B.4.

9 Track Separation Software Structure and Testing

The theory of MSD as described in Section 7.1 is only applicable if the motion type of the particle does not change. However, a constant motion type is seldom the case for particles in a cell. This is because directed motion is often nestled between diffusive motion and vice versa. In order to apply the discussed MSD theory to the data, the data needs to be separated; for this purpose, the software has been developed, which is introduced in this chapter. First, the underlying principle will be discussed. Afterwards, the main algorithm will be explained by following the processes. The chapter closes with a description of the subroutines. While the function of all scripts is discussed in this chapter, the implementation into MATLAB (MATLAB 2020b, The MathWorks, Inc., Natick, MA, USA) can be found in Appendix B.3.

9.1 Underlying Principle

When looking at a particle track, the separation of directed and diffusive parts is quite intuitive. Converting the intuition into software is one of the main challenges. The way we perceive our surroundings is highly personal; therefore, the explanation for the way the intuitive differentiation between the directed and diffusive part is based on one's perception. By eye, the main difference between tracks caused by diffusive behavior and tracks caused by directed behavior is the shape. Directed motion tracks exhibit a narrow shape, and diffusive motion is more smeared out. Determination of the tracks' shape by software, however, is a complex task.

A different approach to analyzing the shape is thinking about the amount of line segments to create the impression of a straight line or a smeared-out zigzag line. As a straight line is the shortest connection between two points, it needs less segments than a zigzag line. While the line segments are not directly accessible from tracking data, the positions where a particle has been detected are accessible. Due to the relation of

track segments number n_{seg} and detection positions number n_{pos}, which is given by

$$n_{\text{seg}} + 1 = n_{\text{pos}}.$$

The evaluation of detection points can be used to determine the amount of segments. Based on the relation of motion type and detected particle positions, the underlying principle is to calculate the point density and, therefore, the amount of line segments. The point density varies along the track. It can be used to separate the trajectory into diffusive and directed motion segments. Due to this, the chosen approach is termed **P**oint **D**ensity **M**ap (PDM). The tracks are then separated according to point density thresholds.

9.2 Software Algorithms

In this section, the main script will be discussed chronologically. During this description, subroutines will be introduced by name and function. The subroutines are reviewed in more detail in Section 9.2.2. This type of representation is chosen to enable software users to look up the subroutines without reading the whole section. To further support the modular character of this section, all abbreviations used will be introduced in each paragraph if applicable.

9.2.1 Main Script

The main script is called `evaluationsaving.m`. The data supplied to the script needs to be in the format of two files, of which one is with x, and the other one is with y coordinates. Both files must follow the same structure with the coordinates for a track in a matrix row. If a track is shorter than the longest track, the row is filled with zeros or `NaN` flags. When the data is loaded, it is processed track by track.
The first evaluation step is done by filtering the data according to the track length. If a track is longer than 29 points and there are less than 10 % of gaps in the track where the particle could not be detected, evaluation is not executed. If the track meets these requirements, the **P**oint **D**ensity **M**ap (PDM) of the track is calculated within `pdcalc.m`.

The downside of the PDM approach is that the calculated point density is initially a numerical value without meaning. To be able to use it as a measure of motion type track evaluation, there needs to be a reference value for the different types of motion. This reference value could be set by the experimentalist, which poses the risk

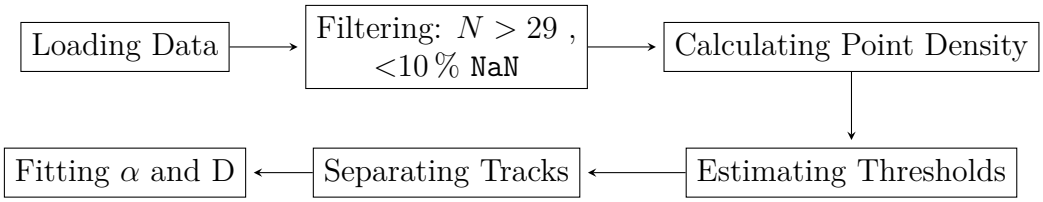

Figure 9.1: Flowdiagram of `evaluationsaving.m`

of bias, depending on the overall visual impression of the track or the point density. To overcome this, a pseudorandom number generator-based simulation introduces a point density threshold as a reference value for the motion types. This is done in the subroutine `pdestimator.m`.

The processes described in this paragraph are performed consecutively for track segments above and below the corresponding threshold but will only be described once. Using these thresholds, the track data is separated into the different types of motion in `trackseparator.m`. The segments are then stored in variables `above`, `between`, and `below`. The tracks above both thresholds are deemed to be of diffusive or subdiffusive motion, and the tracks below both thresholds are deemed to be of directed motion. The track segments between both thresholds are not assigned to any motion type. Most segments between the thresholds originate from transitions of motion types or short segments of Brownian/directed motion nested between longer segments of directed/Brownian motion.

For each found segment, an $\alpha - D$-fit is performed according to Equation (7.3) in `alphadfit.m`. The usage of Equation (7.3) is due to the common representation of the data in $\alpha - D$-maps. Afterwards, the results are saved. In Figure 9.1 a flow diagram of the script is shown.

9.2.2 Subroutines

In this section, subroutines will be discussed in more detail. The paragraphs are in alphabetical order of the subroutine name to enable a dictionary-like use of this chapter. Here a description of the working principle and the used data structures is given. The implementation into MATLAB can be found in Appendix B.3.

`alphadfit.m` is the subroutine applying the theory described in Section 7.1 on the acquired data sets of **M**ean **S**quared **D**isplacement(MSD). Fitting Equation (7.3) is not advisable due to frequent non-convergence of the fitting routine. A weighted linear

relation is fitted to the log-log data set as a solution. The linear relation is given by

$$\mathrm{MSD} = 4D\tau^{\alpha} \rightarrow \log(\mathrm{MSD}) = \log(4D) + \log(\tau)\,\alpha, \tag{9.1}$$

with the diffusion constant D, the lag time τ and an exponential factor α. As the MSD is given in the unit of $pixels^2$ and τ is given in multiples of the acquisition time, the resulting diffusion constant is given in the unit of $pixels^2/(accquisition \quad time)$. As a result of this, the weights are given by the reciprocal of the number of values averaged to calculate the MSD. Due to the high number of evaluated track segments which can easily be in the tens of thousands, a condition is defined to determine if the tracks are sufficiently long to fit. This lower level is chosen to be 29 points. Since only the first quarter of the MSD can be fitted [109], this corresponds to a fitted MSD length of 28 points which in turn results in a minimum track length of 29. This lower limit is chosen as for lower track lengths; the algorithm does not give reliable results. Based on this condition, four points are being averaged for the seventh data point. If the requirement is met, α and D are returned as numerical values; otherwise, `NaN` is returned for both of them.

As input a $1 \times n$ double vector of the MSD is accepted.
The output is a 1×2 vector containing α in the first position and D in the last.

`calcmsd.m` is a simple routine which calculates the **M**ean **S**quared **D**isplacement (MSD) for a given track segment and returns it.

As input, a $m \times n \times 3$ double vector of the track segment data is accepted, where m is the number of track segments handed over, n is the length of the longest segment. For all track segments, there are three entries; the first is the position of the track segment in the original track. The second and third elements are the x and y coordinates of the track segment.
The output is a $m \times n$ vector containing the MSD for all track segments.

`fillnan.m` interpolates `NaN` gaps in the tracks. This is done for the point density calculation only. For the point density, the gaps in a track need to be taken into account. Otherwise, the density would be too low in the vicinity of a gap. The interpolation is done by linearly connecting the last found point before a gap with the first point found after the gap. Here for each gap frame, a point is set equally spaced on the connection line.

The input is a $n \times 3$ vector with the track data. The output is a $n \times 3$ vector with interpolated gaps.

modgauss2.m generates a Gaussian distribution of relative angles between consecutive track segments. The underlying algorithm, however, enables the generation of arbitrary distributions. This is achieved by utilizing the uniform pseudorandom number generator function `rand` included in Matlab. To generate a track with n points, an array of the form

$$\begin{pmatrix} A_1 & B_1 & f(A_1) \\ & \vdots & \\ A_n & B_n & f(A_n) \end{pmatrix},$$

where A and B are uniformly distributed, random values are generated. The function $f(x)$ is the **P**robability **D**ensity **F**unction (PDF) of the distribution which is to be simulated. In the case of generating an angle distribution, A is a proposed angle. The second random B is between 0 and 1. If B is smaller than $f(A)$, the proposed angle is kept. If B is larger than $f(A)$, the random values are replaced and tested against the reference function until the condition $B < f(A)$ is met for all proposed angles. The angles are proposed in the range of $-180°$ to $180°$. In the case of step generation, the steps are generated in an interval of $\mu \pm 3\sigma$, with the mean of the distribution μ and the standard deviation σ.

The input consists of 2 variables. The first is an $n \times 9$ all zero double vector, with n the number of positions to be simulated. The nine columns are to enable different algorithms for step width and angle. The second input is a structure containing the used mode "angle" or "step". In the case of angle, the other fields are the mean of the distribution μ and the standard deviation of the distribution σ. In the case of a step, the other fields are the mean of the distribution μ and the 6σ width of the distribution.

The output is a $n \times 9$ double vector which is filled with the following data:

1. Zeros to mark the data as simulated
2. Proposed angle values A in degree
3. Random value B
4. Proposed step width C in pixel
5. Random value D
6. $f(A)$ for angle values compared to B
7. $f(C)$ for step width compared to D

8. Zeros filled later in `pdestimator`
9. Zeros filled later in `pdestimator`

In Figure 9.2, an exemplary Gaussian distribution generated with `modgauss2.m` is shown. The set parameters are $\mu = 0°$ and $\sigma = 10°$. The corresponding parameters from the shown Gaussian fit are given by $\mu_f = (-0.1 \pm 0.2)°$ and $\sigma = (10.0 \pm 0.2)°$, thus showing accordance with the set parameters. The set parameters are $\mu = 0°$ and $\sigma = 180°$. Here a slight preference for angles around zero is visible. This behavior of the angle relative to the track element before is expected as the particle shows a slight preference to stay in the mode of motion it is in.

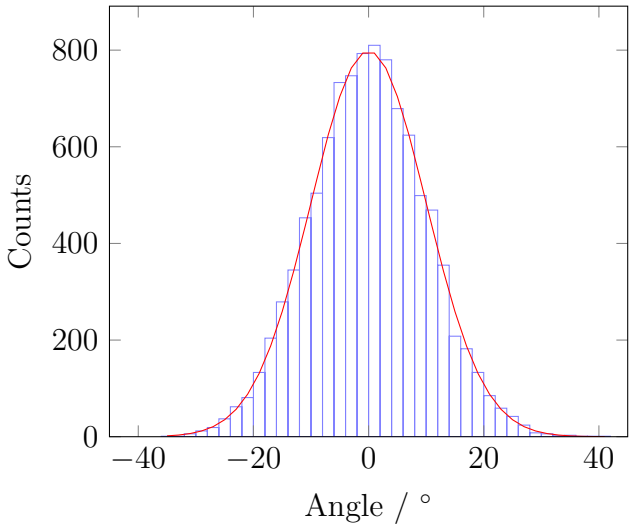

(a) Exemplary distribution with $\mu = 0$ and $\sigma = 10$. The shown Gaussian fit has the parameters: $\mu_f = (-0.1 \pm 0.2)°$ and $\sigma = (10.0 \pm 0.2)°$, with an amplitude of $A = (19\,990 \pm 330)$.

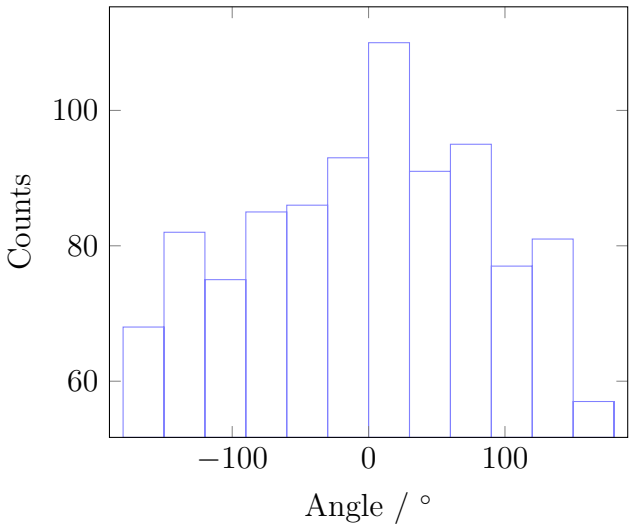

(b) Exemplary distribution with $\mu = 0$ und $\sigma = 180$.

Figure 9.2: Exemplary distributions simulated by `modgauss2.m` with $N = 1000$.

`pdcalc.m` is used to calculate the point density for each point in a track. This is done by calculating a distance matrix, where for each point on the track, the distance to all other points is calculated and noted line by line. For a track with n points, the matrix reads

$$\begin{pmatrix} \overline{p_1p_1} & \overline{p_1p_2} & \dots & \overline{p_1p_n} \\ \overline{p_2p_1} & \overline{p_2p_2} & \dots & \overline{p_2p_n} \\ \vdots & \vdots & \ddots & \vdots \\ \overline{p_np_1} & \overline{p_np_2} & \dots & \overline{p_np_n} \end{pmatrix},$$

where $\overline{p_xp_y}$ denotes the distance between point x and y.

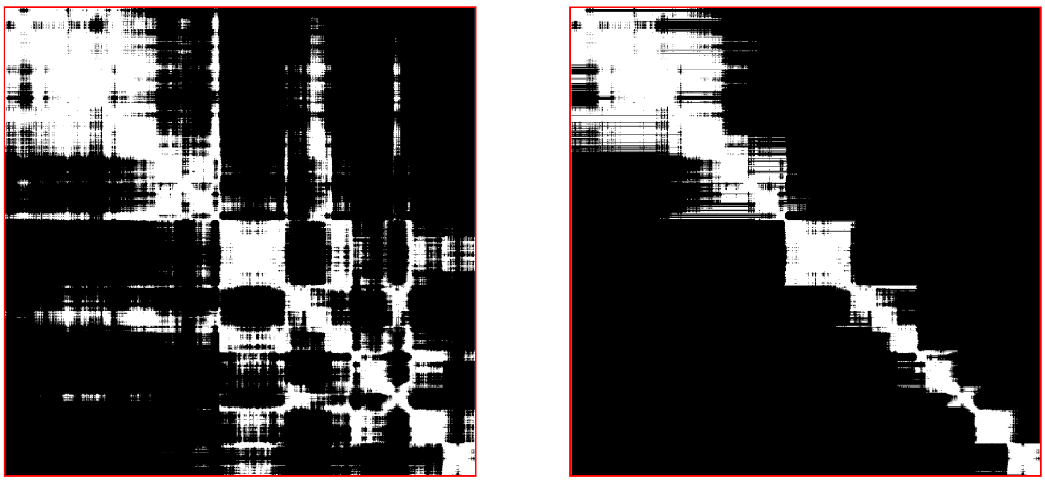

(a) Unfiltered version of the validity matrix.

(b) Filtered version of the validity matrix.

Figure 9.3: Different versions of the validity matrix of a diffusive track, shown as a black-and-white image. Values of `TRUE` are depicted in white, and `FALSE` is depicted in black. A red border is added around the matrix images to visually separate `TRUE` values from the background. The shown data is of a simulated diffusive motion track with a length of 1000 points.

For a point p_y to be valid for the density of point p_x, it needs to be inside a circle with radius r. The radius is calculated dependent on the mean step size s, which is determined by a moving average that averages over five values and is given by

$$r = 5s.$$

The moving average for the search radius determination is included to account for step width changes in a single track. In Figure 9.3, an exemplary validity matrix is shown.

The main diagonal represents the distance of a particle to itself; therefore, it is always zero and valid. The point density is calculated line by line. In each row, valid segments which are connected to the main diagonal represent the particle not leaving the validity circle. If, in between two valid positions, there is an invalid position, this means that the particle left the validity radius, while it is possible for a diffusive moving particle to leave the validity radius for a short time and return, thus causing small sections of positions invalid for the point density calculation. Valid sections are distinct from the main diagonal, indicating that the path crosses itself with a considerable time span in between. In the scope of this work, the gap time span, after which the points inside the radius will not be considered for the point density, is 0.5 s. To exclude these points from the point density calculation, all valid points which are separated from the main diagonal by more than n steps are set to be invalid. Here n is calculated by

$$n = \frac{0.5\,\mathrm{s}}{t_a},$$

with the acquisition time t_a. The point density is then calculated by calculating the sum over all valid particle positions.

The input is a $n \times 3$ vector of the track and the acceptable time a track can leave the radius before not being considered for the point density.

`pdestimator.m` is used to estimate the expected point density for a given type of motion. The estimation is based on a simulated track, which is then evaluated for its point density. The expected point density depends on mainly two factors. The first factor is the type of motion as discussed in Section 9.1. The second factor is the step width. To create an accurate estimate of the point density, both need to be taken into account. The return value is the estimated point density.

The type of motion is determined by the user by adjusting the distribution of the angle between a track element and the following element. The angle distribution is simulated by `modgauss2.m`. The step length is extracted from the track, which will be evaluated with the estimated density thresholds. This is done in `stephistogram.m`, which returns the parameters of a skew Gaussian, which is fitted to a step histogram. With the outputs of `skewgaussgen.m` and `modgauss2.m`, the detection points are simulated. The track data is then evaluated with `pdcalc.m`. For a directed motion, the upper threshold returned is the maximum found point density, as the maximum is a measure for the directness of the motion. For a diffusive motion, the lower threshold median point density is returned. For a Brownian motion, the minimum value is not a robust choice as it is possible that, by chance, a small directed part is in the Brownian motion

type, as the angle between consecutive track segments is not limited. The resulting inaccuracy is compensated for in `trackseparator.m`.

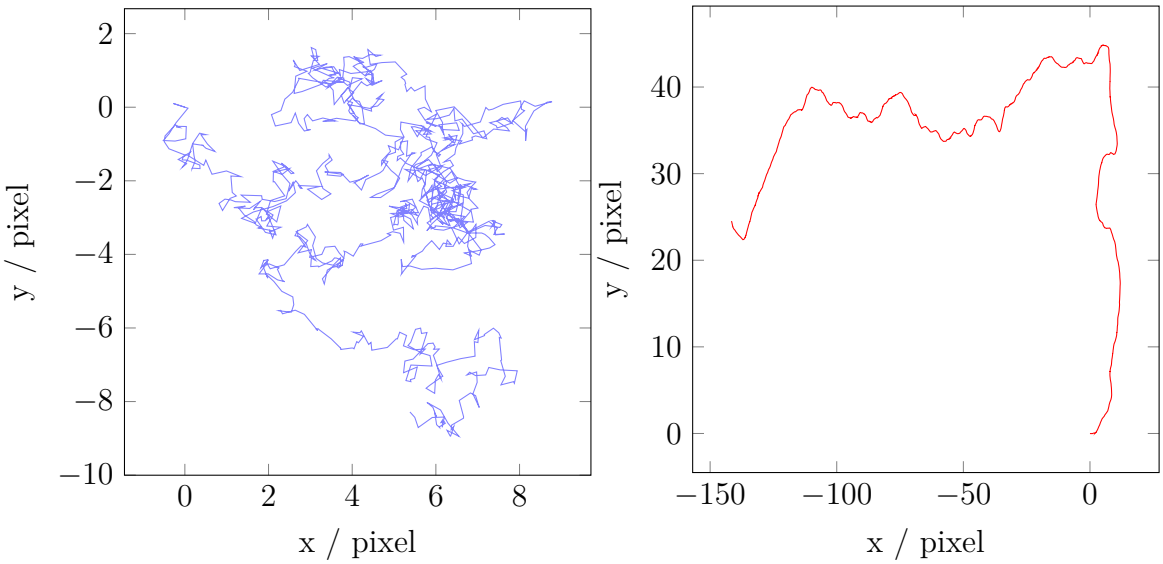

(a) Simulated diffusive track. $\alpha = 1.01$ **(b)** Simulated directed track. $\alpha = 1.89$

Figure 9.4: Exemplary simulated tracks for an angle distribution with $\sigma = 180°$ in a) and an angle distribution with $\sigma = 10°$ in b).

In Figure 9.4, simulated tracks are shown. For both tracks, there are segments that do not resemble the expected shape of directed or Brownian motion. While this indicates that the separation of tracks can include false assignments, there is no way of reconstructing the cause of the motion from the track. The probability for a segment to resemble a certain type of motion by chance is reduced the longer the segment is. Therefore a lower limit for the length of track segments is reasonable. This lower limit is, however, already introduced by the length minimum in `evaluationsaving.m`. While these observations are made on simulated tracks, they also hold true for real tracks as they are also subjected to random events.

In the scope of this project, the chosen standard deviation for directed motion is $\sigma_D = 10°$ and for Brownian motion $\sigma_B = 180°$.

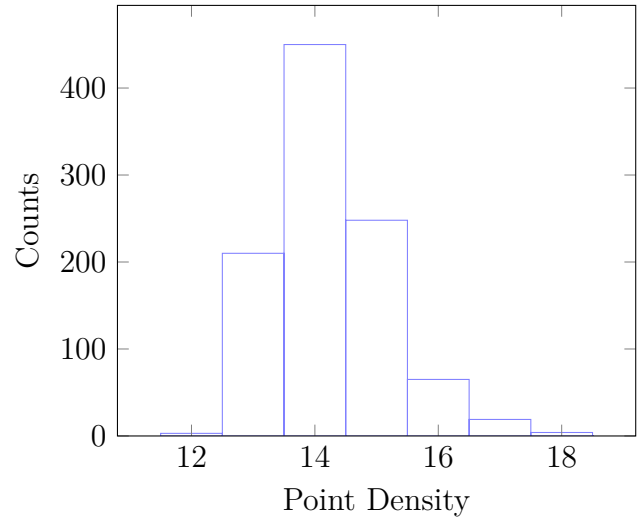

(a) Lower point density estimates.

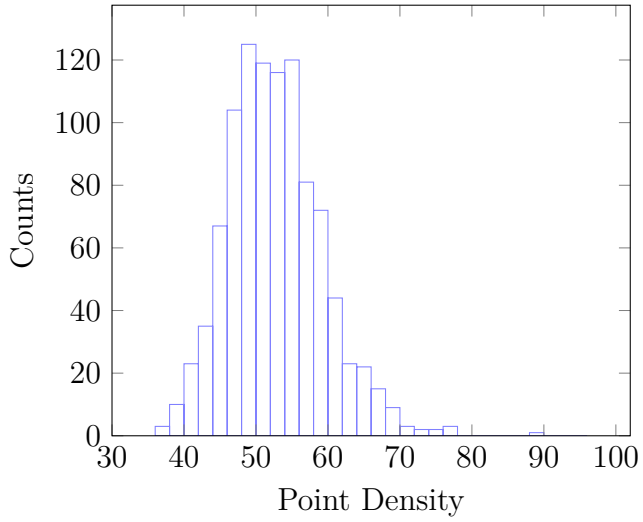

(b) Upper point density estimates.

Figure 9.5: Distributions of the point density thresholds generated by `pdestimator.m` with $N = 1000$.

In Figure 9.5, the distribution of 1000 estimated point density thresholds is shown. For the lower threshold, the distribution is narrow, while for the upper threshold, the distribution is considerably broader.

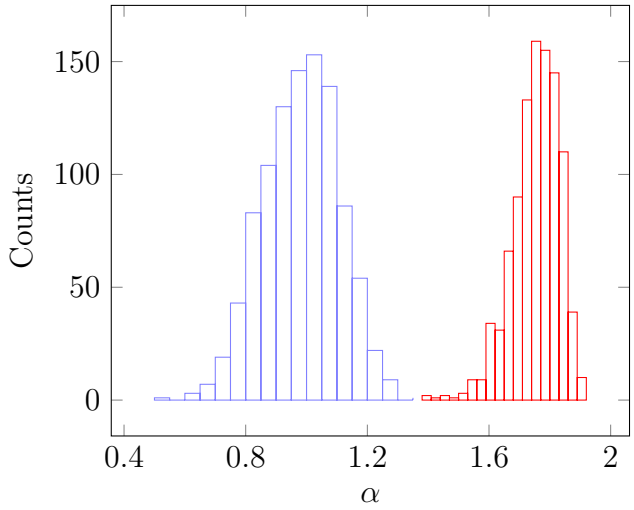

Figure 9.6: Distribution of α values from fitting the **M**ean **S**quared **D**isplacement(MSD) of simulated tracks. In red the α of tracks with $\sigma = 10°$ is shown. In blue the α of tracks with $\sigma = 180°$ is shown.

In Figure 9.6, the α values for simulated tracks are shown. These values are extracted from the tracks by calculating the **M**ean **S**quared **D**isplacement(MSD) via `calcmsd.m` and forwarding the results to `alphadfit.m`. The MSD values for simulated tracks with a given $\sigma = 10°$ shows a distribution in the range of 1.4 to 1.9. The MSD values for simulated tracks with a given $\sigma = 10°$ shows a distribution in the range of 0.5 to 1.35.

The input is a $n \times 4$ vector including track data and point density and a `struct` with the set mode, the distribution standard deviation σ, the point length of the simulated track, and the accepted gap size for `pdcalc.m`. The output is the estimated point density.

`skewgaussgen.m` generates a step width distribution according to the normalized version of the reference formula given in Equation (9.2). The parameters used are supplied by `stephistogram.m`. In theory, the used distribution is never 0. To enable efficient computation, the interval simulated needs to be limited. This is done by limiting the interval of possible step width to $\mu \pm 3\sigma$. The reference function is externalized in `distributionfunc.m`.

For the function principle to generate an arbitrary distribution, input, and output variables, please see `modgauss2.m`.

stephistogram.m determines the step width distribution in a track by fitting a skew Gaussian given by

$$2A \cdot \underbrace{\frac{1}{2}\left[1 + \operatorname{erf}\left(\frac{x-\mu}{\sigma\sqrt{2}}\right)\right]}_{\mathrm{CDF}(x,\sigma,\mu)} \cdot \underbrace{\frac{1}{\sigma\sqrt{2\pi}} \mathrm{e}^{-\frac{1}{2}\left(\frac{x-\mu}{\sigma}\right)^2}}_{\mathrm{PDF}(x,\sigma,\mu)} \tag{9.2}$$

to the histogram of the step width, with the mean μ, the standard deviation σ, the amplitude A, erf is the Gauss error function. The first part of the equation is the Gaussian **C**ummulative **D**istribution **F**unction (CDF), and the second part is the Gaussian **P**robability **D**ensity **F**unction (PDF). This function was chosen solely on the observation that it does resemble the histogram shape. As a result of the monomodal shape of the distribution, it is shown that the step width does not depend on the type of motion observed.

Input is a $n \times 3$ vector. The first column is an index column, second and third columns are x and y coordinates. The output is a 1×3 vector with A, μ, and σ from the skew Gaussian distribution.

trackseparator.m is used to separate the track segments according to the found thresholds. As described in `pdestimator.m`, the threshold for directed motion is the maximum value detected in the simulation, and the threshold for Brownian motion is the median observed point density. As the simulations can only map one instance of reality, these values are not to be understood as absolute. To account for this uncertainty, a correction is introduced. This correction is dependent on the relative difference of the thresholds. The idea is to move the thresholds closer together by a percentage of the difference. In the scope of this work, the limit for directed motion is increased by 10 % of the difference, and the limit for Brownian motion is reduced by 30 %. The larger reduction of the threshold for Brownian motion is due to the choice of the median for the threshold determined by `pdestimator.m`. Using these values has been shown to lead to a segmentation that is consistent with the segmentation that would be done manually by the experimenter.

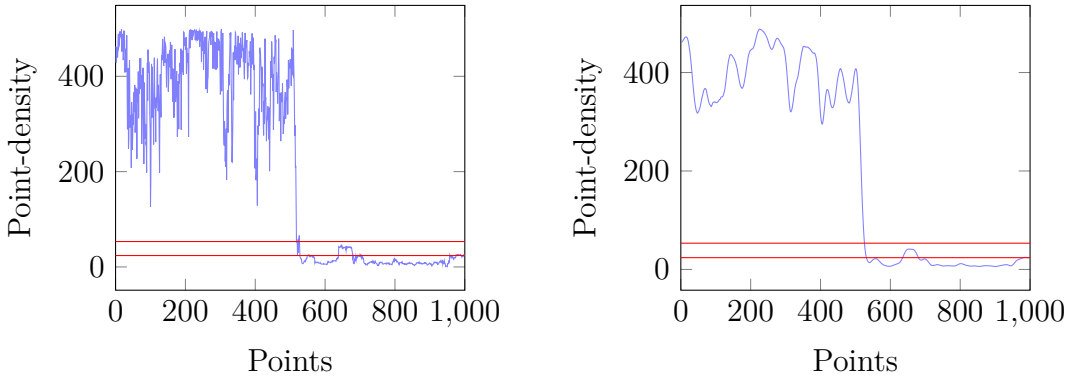

(a) Unfiltered **(b)** Filtered

Figure 9.7: Unfiltered and filtered point-density. The applied filter is a Gaussian filter with a kernel size of 7. The thresholds are indicated as horizontal lines.

The point density calculated by `pdcalc.m` shows erratic changes, especially in the Brownian motion part of a track, as shown in Figure 9.7. Since this could lead to interruptions of track segments, the point density is smoothed with a Gaussian filter. Based on the smoothed point density, the track segments are determined as the part of a track that stays above/below the threshold for Gaussian/directed motion. Returned are the track segments divided into arrays containing the parts above both thresholds, between the thresholds, and below the thresholds.

Input is a $n \times 4$ vector with the track data including the point density, and a `struct` containing the σ of the Gaussian smoothing kernel, the correction factors of the thresholds, upper and lower threshold. The output is three $m \times n \times 3$ vectors. m is the number of segments, n the length of the longest corresponding segment.

9.3 Separation of Endosome Tracks

Endosomes are formed during endocytosis by the invagination of the cell membrane. As the primary mean of internalizing larger particles into the cell, endosomes are important for intracellular transport. To be able to perform fluorescence microscopy on endosomes, endosome markers are used.
In this section, the algorithm is applied to tracking data of endosomes from eight different cells. Each cell takes an image stack of 1000 frames with an acquisition time of 50 ms. The tracking is performed with u-Track (Section 8.2). Exemplary resulting tracks are shown in Figure 9.8 overlayed with a fluorescence image from the cell video.

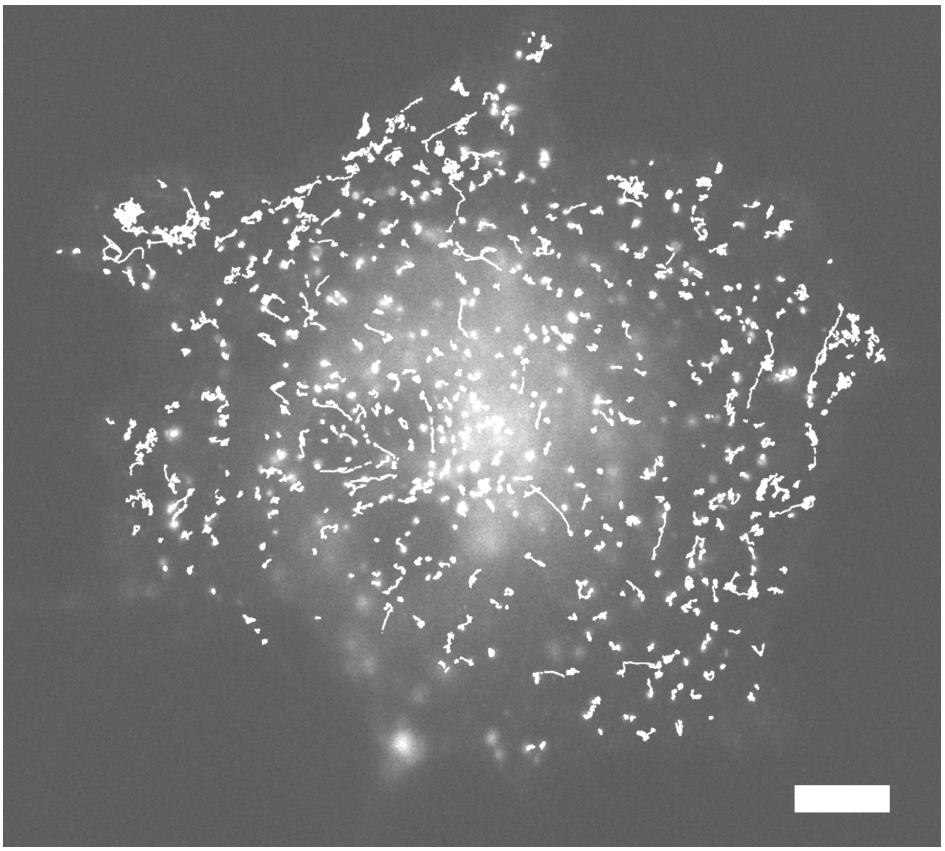

Figure 9.8: Image of a cell with all tracks depicted. Acquisition time is 50 ms. The scalebar is 10 µm. The contrast is enhanced; the original image can be found in Appendix B.5.

It is evident that the majority of tracks show subdiffusive behavior, as the tracks are confined to small areas; there are, however, also path showing directed motion, where the path is elongated. These classifications are based solely on the visual impression from the image. Since the evaluation is based on the visual impression of the image, the evaluation algorithm is expected to find more tracks classified as diffusive than

classified as directed.

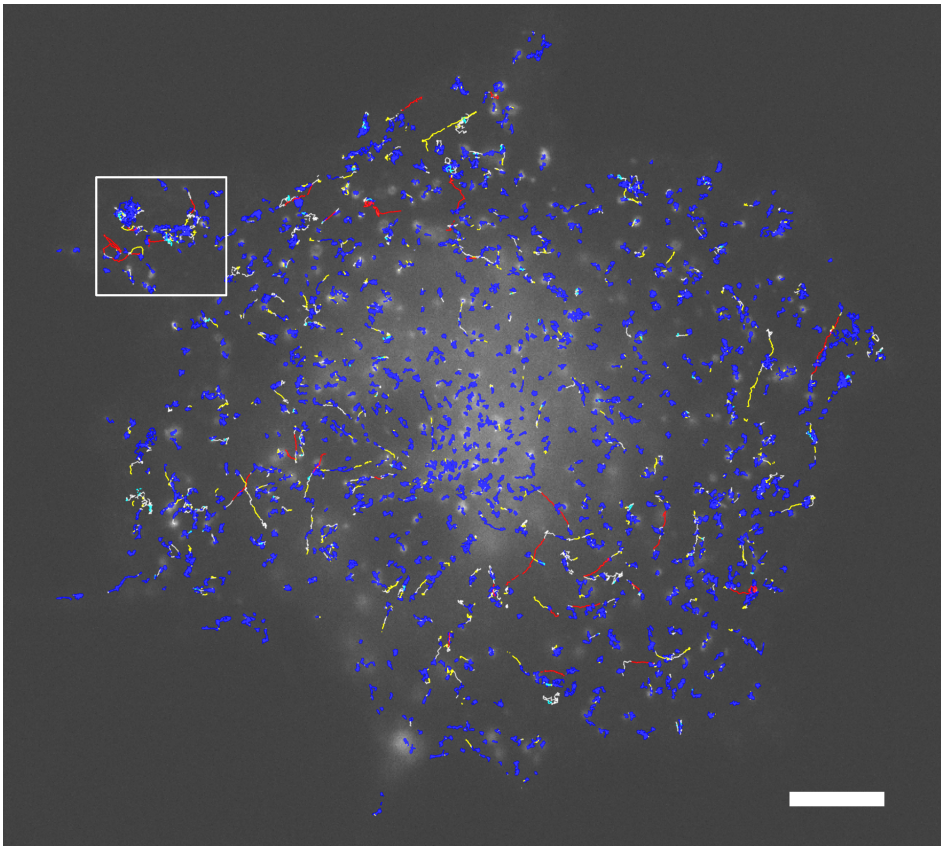

Figure 9.9: Image of a cell with all tracks depicted. Acquisition time is 50 ms. The tracks are color-coded: Blue) Track segments that are above the upper threshold and longer than or equal to 29 Steps. Red) Track segments that are below the lower threshold and longer than or equal to 29 Steps. Cyan) Track segments that are above the upper threshold and shorter than 29 Steps. Yellow) Track segments that are below the lower threshold and shorter than 29 Steps. White) Track segments between the thresholds. The inset is magnified in Figure 9.10. The scalebar is 10 µm. The contrast in the shown image is adjusted, the original image can be found at Appendix B.5.

In Figure 9.9, the tracks are shown color-coded, dependent on the classification of the algorithm. The track segments are color coded. Tracks segments that are classified as diffusive are shown in blue if longer than 28 frames and in cyan if not. Tracks segments classified as directed are shown in red if longer than 28 frames and yellow if not. Track segments are shown white if the point density is between the thresholds. For all blue and red tracks, the MSD is calculated, and Equation (9.1) is fitted.

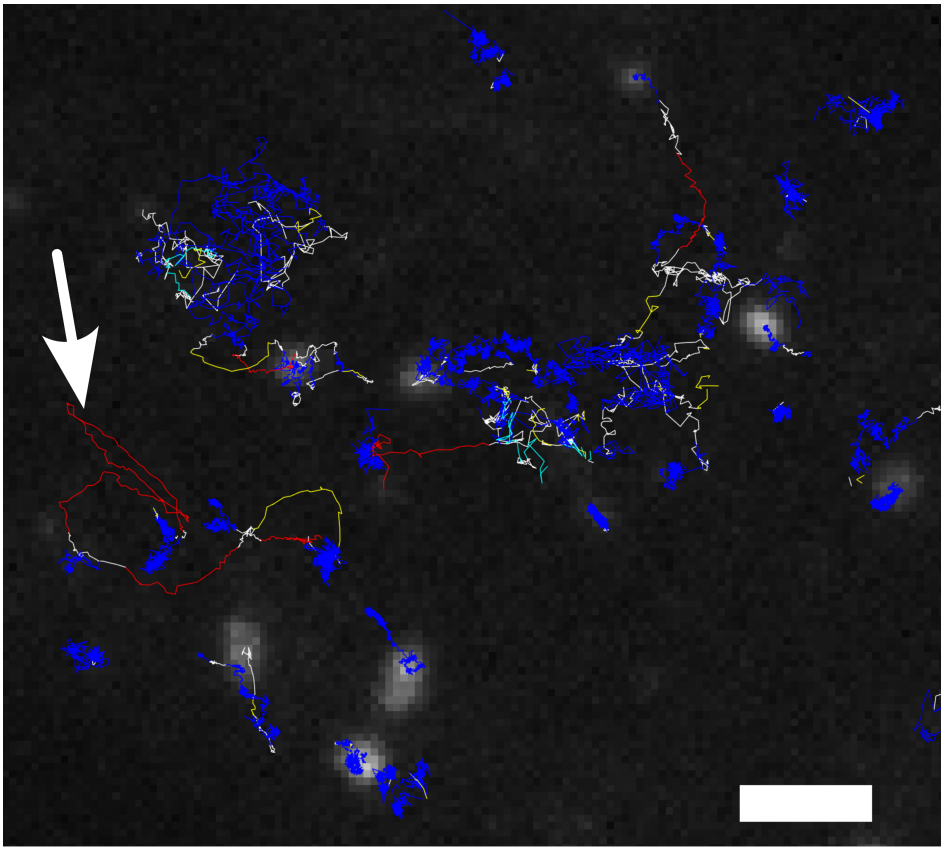

Figure 9.10: Image of a cell with all tracks depicted. Acquisition time is 50 ms.The tracks are color-coded: Blue) Track segments that are above the upper threshold and longer than or equal to 29 Steps. Red) Track segments that are below the lower threshold and longer than or equal to 29 Steps. Cyan) Track segments that are above the upper threshold and shorter than 29 Steps. Yellow) Track segments that are below the lower threshold and shorter than 29 Steps. White) Track segments between the thresholds. The shown image is a magnified inset from Figure 9.9. The scalebar is 2 µm.

In figure Figure 9.10, the inset indicated in Figure 9.9 is shown. Here it can be seen how the tracks are segmented. The blue and red tracks show the expected form for diffusive and directed behavior. It is also visible how the temporal limitation in the point density calculation prevents the increase of the point density by intersections of the same track, as the red track on the left side crosses itself multiple times for track segments below the length limit depicted in cyan or yellow different behavior can be seen. Multiple tracks showing diffusive behavior are shown in yellow. These track segments reveal a shortcoming of the point density approach. For a track with n points, the maximum reachable point density is also n; thus, tracks with a total length below the lower threshold cannot be assigned a higher point density. While this leads to a missed assignment of the tracks, the overall loss of data due to this effect is low since tracks shorter than the lower threshold are not suitable for evaluation.

Track segments between the thresholds are often nested in between diffusive motion parts, which resembles the observed seemingly linear segments in the simulated diffusive tracks.

All evaluation up until now is based on the visual impression of the track segments. While this is a valid approach for a first impression, further evaluation is needed to verify the assignment by point density. As described in Section 7.1, the behavior of a particle can be determined by fitting Equation (7.3). In Figure 9.11, the resulting parameters are shown. However, using a diffusion constant is only valid for an exponent of $\alpha = 1$, a representation in the type of an α-D-Map as it is a well-known graphical representation and enables a fast perception of the results. It is visible that the separation of the track segments according to the point density leads to a separation of movement types.

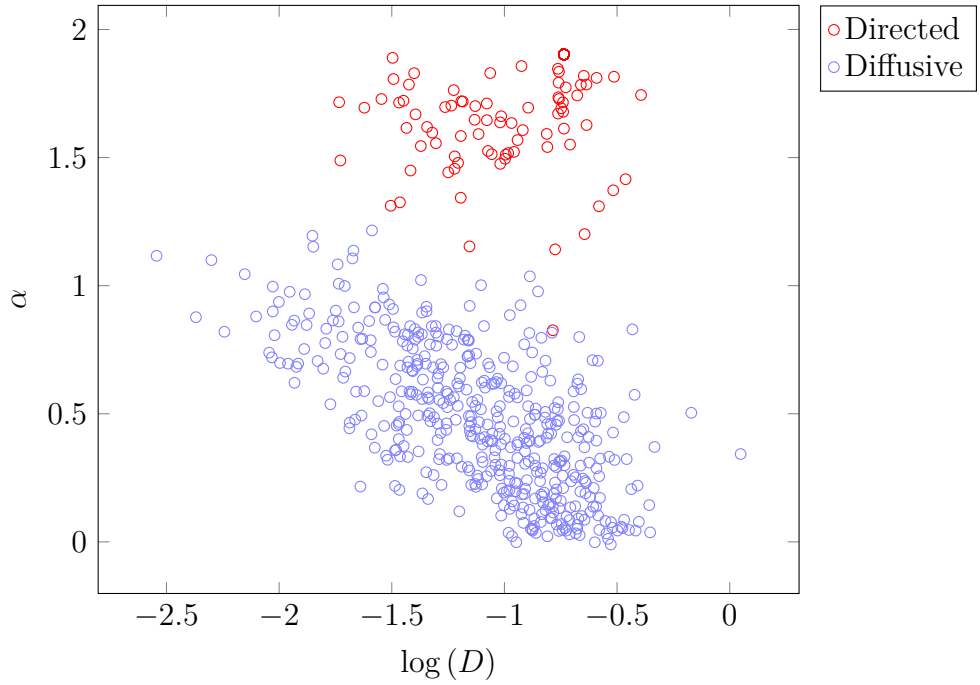

Figure 9.11: α-D plot of the track segments for all cells. The differentiation into diffusive and directed motion is based on the assignment from the point density algorithm. For better visibility, 10 % of the diffusive classified tracks are shown. A unit for D is not given since it changes in the graph. α is unitless.

10 Conclusion

The aim of this project was to develop a method for track segmentation that is based on the visual impression of tracks. This approach is chosen as it is closest to the division by an experimenter. A MATLAB script has been developed to achieve this, which segments the tracks depending on the local point density. The segmentation is based on simulated tracks which are generated based on the distribution of angles defined by three track points and the step width distribution of the investigated track. For the calculation of the point density, the radius is variable along the track defined by the local step width. With the use of this radius, the point density is calculated by the sum of all points which are within the radius and are generated without the particle leaving the radius for more than 0.5 s. Due to the automatic determination of most parameters used in the script, the user inputs could be minimized. The effectiveness of the developed algorithm has been tested by fitting the MSD to determine the exponent α, which is a measure for the type of motion. Here a clear correlation of motion type is determined by the point density, and motion type is determined by the α-D-fit.

The algorithm developed has been shown to fulfill the requirement of separating the tracks according to the motion type without resorting to other statistical models, like ensemble averaging or calculating correlation functions. Thus it is a valuable tool for data selection. The selected data can then be used for further evaluation, for example, cellular signaling processes.

Supplementary Information

A Magnetic Hyperthermia Supplementary Information

A.1 Calculations and Derivations for Understanding

In this appendix, calculations which aid the understanding will be shown. All of these calculations have been performed numerous times before. In publications and books, they are, however, often not explicitly given or deemed to be trivial. They mostly rely on well-known basic physical principles, and some of them are even readily used as exercise tasks. Nevertheless, they might not be known to everyone. For the sake of completeness and as it may cost some time to find them or to do them oneself, they are included here with the aim of sparing the reader from the search for these calculations.

RLC Circuit

Here the calculations are shown, which result in the formulas 4.4 and 4.5. In A.1, the simplest driven RLC circuit is shown. The following calculations are based on this model. For the circuit used in this work, the calculations are still valid, although there are multiple influences on the capacitance, inductance, and resistance. These, however, can be summarized into the given R, L, and C values.

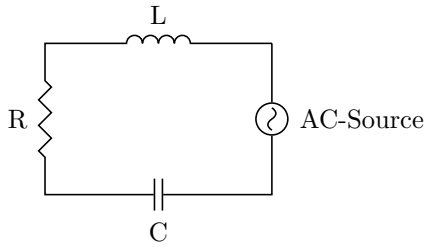

Figure A.1: Simplest representation of a driven RLC circuit.

To describe the circuit, the voltage is a good choice since Kirchhoff's voltage law states that the sum of all voltages is zero for a closed loop. Therefore the voltages can be written as

$$0 = U_{\mathrm{L}} + U_{\mathrm{C}} + U_{\mathrm{R}} - U_{\mathrm{ext}}. \tag{A.1}$$

The voltages for the different components can be expressed concerning their dependency on the charge Q and its temporal derivatives, given by

$$\begin{aligned} U_{\mathrm{C}} &= \frac{Q}{C}, \\ U_{\mathrm{R}} &= RI = R\dot{Q}, \text{and} \\ U_{\mathrm{L}} &= L\dot{I} = L\ddot{Q}, \end{aligned}$$

with the resistance R, the inductance L, and the capacitance C. By substituting the voltages in Equation (A.1) an inhomogeneous differential equation of second order is created, given by

$$\ddot{Q} + \frac{R}{L}\dot{Q} + \frac{1}{LC}Q = \frac{U_{\mathrm{ext}}}{L}.$$

This can be solved with the Ansatz

$$Q(t) = A\mathrm{e}^{\mathrm{i}(\omega t - \theta)}$$

and its temporal derivatives, where A is the amplitude, ω is the circular frequency, t is the time, and θ is the phase lag. By rewriting the external voltage as a complex entity

$$U_{\mathrm{ext}} = U_{\mathrm{ext},0}\mathrm{e}^{i(\omega t - \gamma)},$$

with the amplitude $U_{\mathrm{ext},0}$, one arrives at

$$-A\omega^2\mathrm{e}^{\mathrm{i}(\omega t-\theta)} + A\mathrm{i}\omega\frac{R}{L}\mathrm{e}^{\mathrm{i}(\omega t-\theta)} + A\frac{1}{LC}\mathrm{e}^{\mathrm{i}(\omega t-\theta)} = \frac{U_{\mathrm{ext},0}}{L}\mathrm{e}^{\mathrm{i}(\omega t-\gamma)}.$$

This can be rearranged to

$$-\omega^2\frac{AL}{U_{\mathrm{ext},0}} + \mathrm{i}\omega\frac{AR}{U_{\mathrm{ext},0}} + \frac{A}{CU_{\mathrm{ext},0}} = \mathrm{e}^{\mathrm{i}(\theta-\gamma)}.$$

By exchanging rephrasing $\theta - \gamma = \alpha$ and using the identity of $\exp(\mathrm{i}\alpha) = \cos(\alpha) +$

$\mathrm{i}\sin(\alpha)$ it is possible to determine the equivalence of

$$\cos(\alpha) = \frac{A}{CU_{\mathrm{ext},0}} - \omega^2 \frac{AL}{U_{\mathrm{ext},0}}, \text{and}$$
$$\sin(\alpha) = \omega \frac{RA}{U_{\mathrm{ext},0}}.$$

By further using the relationship $\sin(\alpha)^2 + \cos(\alpha)^2 = 1$ the relationship to α can be removed leading to

$$\left(\frac{A}{CU_{\mathrm{ext},0}} - \omega^2 \frac{AL}{U_{\mathrm{ext},0}}\right)^2 + \left(\omega \frac{RA}{U_{\mathrm{ext},0}}\right)^2 = 1.$$

To extract the amplitude A rewriting as

$$\frac{1}{A^2} = \frac{1}{U_{\mathrm{ext},0}^2}\left(\frac{1}{C} - \omega^2 L\right)^2 + \frac{1}{U_{\mathrm{ext},0}^2}(\omega R)^2$$

is useful. From there A can be rewritten as a function of ω as

$$A(\omega) = \frac{\frac{U_{\mathrm{ext},0}}{L}}{\sqrt{\left(\frac{1}{LC} - \omega^2\right)^2 + \left(\omega \frac{R}{L}\right)^2}}.$$

$A(\omega)$ is the amplitude of $Q(t)$ to calculate the amplitude $\bar{A}$of $U(t)$ it needs to be divided by C leading to

$$\bar{A}(\omega) = \frac{\frac{U_{\mathrm{ext},0}}{LC}}{\sqrt{\left(\frac{1}{LC} - \omega^2\right)^2 + \left(\omega \frac{R}{L}\right)^2}}. \tag{A.2}$$

Outgoing from this formula, the resonance frequency can be found by determining the maximum value. The numerator of Equation (A.2) is not dependent on the frequency; therefore, the expression gets maximal for the denominator being minimal. Due to all individual values in the square root being positive real numbers, the square root is strictly monotonously increasing. Thus the denominator gets minimal for the expression inside the root being minimal. This can be determined via the derivative, which is given by

$$\frac{\mathrm{d}}{\mathrm{d}\omega} = \left(A - \omega^2\right) + (B\omega) = 2\omega\left(B^2 - 2A + 2\omega^2\right),$$

with $A = 1/(LC)$ and$B = R/L$. By finding the zero of this derivative, one gets

$$\begin{aligned} 0 &= 2\omega\left(B^2 - 2A + 2\omega^2\right) \\ \Leftrightarrow \omega &= \sqrt{A - \frac{B^2}{2}}. \end{aligned}$$

Resubstituting A and B and converting from angular frequency to frequency, one arrives at

$$f_\mathrm{r} = \frac{1}{2\pi}\sqrt{1/(LC) - \frac{R^2}{2L^2}}.$$

Conversion of Maxwell equations

In Section 2.1 it is stated that the Integral and differential forms of the Maxwell equations can be transformed into each other. These conversions are done using the Stokes Theorem given by

$$\iint \vec{\nabla} \times \vec{v} \cdot \mathrm{d}a = \oint \vec{v} \cdot \mathrm{d}s$$

stating that the two-dimensional integral of the curl of a vector field $\vec{v}$ over an area a this is equal to the closed path integral of the vector field along the perimeter of the area. The Gauss's theorem is also used, which is given by

$$\iiint \vec{\nabla} \cdot \vec{v} \mathrm{d}^3 r = \oiint \vec{v} \cdot \mathrm{d}\vec{a}$$

stating that the volume integral over the divergence of a vector field v is equal to the integral over the vector field along the surface of the volume. Starting with Equation (2.1)

$$\vec{\nabla} \cdot \vec{E} = \frac{\rho}{\epsilon_0}$$

a 3D integral is done, to be able to apply Gauss's theorem.

$$\iiint \vec{\nabla} \cdot \vec{E} \mathrm{d}^3 r = \iiint \frac{\rho}{\epsilon_0} \mathrm{d}^3 r.$$

On the right-hand side, the constant ϵ_0 can be moved out of the integral; the resulting integral over the charged density ρ is just the total charge Q inside the volume. On

the left-hand side, Gauss's theorem is applied, leading to

$$\oiint \vec{E} \cdot \mathrm{d}\vec{a} = \frac{Q}{\epsilon_0}.$$

Using equation Equation (2.9) $\left(\vec{D} = \epsilon_0 \vec{E}\right)$ in the absence of polarization leads to

$$\oiint \vec{D} \cdot \mathrm{d}\vec{A} = Q.$$

Carrying on with Equation (2.2) given by

$$\vec{\nabla} \cdot \vec{B} = 0$$

is straightforward. By applying a 3D integral, one gets

$$\iiint \vec{\nabla} \cdot \vec{B} \mathrm{d}^3 r = \iiint 0 \mathrm{d}^3 r.$$

Applying Gauss's theorem directly leads to

$$\oiint_{\partial V} \vec{B} \cdot \mathrm{d}\vec{A} = 0.$$

The third given equation in Section 2.1 is

$$\vec{\nabla} \times \vec{E} = -\frac{\partial \vec{B}}{\partial t}.$$

The left-hand side curl indicates to use of Stokes theorem, giving

$$\begin{aligned} \iint \vec{\nabla} \times \vec{E} \cdot \mathrm{d}\vec{a} &= \iint -\frac{\partial \vec{B}}{\partial t} \cdot \mathrm{d}\vec{a} \\ \oint \vec{E} \cdot \mathrm{d}\vec{s} &= -\frac{\mathrm{d}}{\mathrm{d}t} \iint \vec{B} \cdot \mathrm{d}\vec{a}. \end{aligned}$$

The right-hand side of this equation is just the definition of the magnetic flux. Thus it can be rewritten to

$$\oint_{\partial A} \vec{E} \cdot \mathrm{d}\vec{s} = -\frac{\mathrm{d}\Phi_\mathrm{B}}{\mathrm{d}t}.$$

The last equation is given by

$$\vec{\nabla} \times \vec{B} = \mu_0 \vec{j_\mathrm{c}} + \mu_0 \epsilon_0 \frac{\partial \vec{E}}{\partial t}.$$

By integrating both sides of this equation over an area, one obtains

$$\iint \vec{\nabla} \times \vec{B} \cdot \mathrm{d}a = \mu_0 \iint \vec{j_c} \cdot \mathrm{d}\vec{a} + \mu_0 \epsilon_0 \frac{\mathrm{d}}{\mathrm{d}t} \iint \vec{E} \cdot \mathrm{d}\vec{a}.$$

Applying Stokes's theorem to the right-hand side leads to

$$\int \vec{B} \cdot \mathrm{d}\vec{s} = \mu_0 j + \epsilon_0 \mu_0 \frac{\mathrm{d}\Phi_\mathrm{E}}{\mathrm{d}t}.$$

Just like above Equation (2.9) in the absence of polarization in combination with Equation (2.10) in the absence of magnetization $\left(\vec{H} = \frac{\vec{B}}{\mu_0}\right)$ leads to

$$\int \vec{H} \cdot \mathrm{d}\vec{s} = j + \frac{\mathrm{d}\Phi_\mathrm{D}}{\mathrm{d}t}.$$

Coupling Factor

For a transformer the voltages $V_{1/2}$ at the terminals are given by

$$V_1 = i\omega \left(L_1 I_1 + L_{12} I_2\right), \tag{A.3}$$

$$V_2 = -i\omega \left(L_2 I_2 + L_{12} I_1\right), \tag{A.4}$$

where $L_{1/2}$ are the inductances of the two coils, $I_{1/2}$ are the current running through the respective coil, and L_{12} is the mutual inductance [34, p.153]. Of particular interest for a transformer are two load cases that are of special notice. The first is minimum load where there is no secondary side current I_2 because the secondary side is open-circuited. The second is maximum load, where the secondary side is short-circuited, so there is no secondary side voltage V_2.

In the case of the unloaded transformer Equation (A.3) simplifies to

$$V_1 = i\omega L_1 I_1,$$

which is the voltage of a single inductor, therefore for effective inductance L_O, the relation

$$L_O = L_1 \tag{A.5}$$

is found. In the short circuited case V_2 is zero, therefore Equation (A.4) becomes

$$\begin{aligned} 0 =& - i\omega \left(L_2 I_2 + L_{12} I_1 \right) \\ =& i\omega \left(L_2 I_2 + L_{12} I_1 \right). \end{aligned}$$

Solving this equation for I_2 yields

$$I_2 = -\frac{L_{12} I_2}{L_2}. \tag{A.6}$$

By substituting Equation (A.6) into Equation (A.3) one arrives at

$$V_1 = i\omega I_1 \left(L_1 - \frac{L_{12}^2}{L_2} \right). \tag{A.7}$$

Here the effective short circuit inductance can be defined to be

$$L_S = L_1 - \frac{L_{12}^2}{L2}, \tag{A.8}$$

because Equation (A.7) resembles the voltage of a single inductor. By solving Equation (A.8) for L_{12}^2 the expression

$$L_{12}^2 = L_2 \left(L_1 - L_S \right) \tag{A.9}$$

can be found. The definition of the coupling factor k is given by [34, p.152]

$$k = \frac{L_{12}}{\sqrt{L_1 L_2}}. \tag{A.10}$$

Squaring Equation (A.10) and inserting Equation (A.9) gives

$$k^2 = \frac{L_2 \left(L_1 - L_S \right)}{L_1 L_2} = 1 - \frac{L_S}{L_1},$$

which can be transformed to

$$k = \sqrt{1 - \frac{L_S}{L_1}}.$$

Heat Generation by Hysteresis

The first law of thermodynamics, the change of internal energy ΔU, is given by

$$\Delta U = Q + W,$$

with the heat supplied Q and work performed on the system by the surroundings W. One way to understand the heat generated by an AMF is to consider a coil subdued to an alternating current, thus generating an AMF. Consider a cored coil with the length l, cross-sectional area A, and N turns. A minor change in the magnetic field strength B is linked to a change in the magnetic flux ϕ by

$$\Delta\phi = N \int \Delta B \mathrm{d}A.$$

In the case of a homogeneous B field, this simplifies to

$$\Delta\phi = N \cdot \Delta B \cdot A.$$

The change in magnetic flux over time t causes an electromotive force F to form.

$$F = \frac{-\mathrm{d}\phi}{\mathrm{d}t} = \frac{\mathrm{d}}{\mathrm{d}t}\Delta B \cdot A \cdot N = N \cdot A\frac{\mathrm{d}B}{\mathrm{d}t}. \tag{A.11}$$

The power P needed to compensate for the electromotive force is given by

$$P = U \cdot I,$$

here U is given by the electromotive force, which is albeit the name indicating a force a voltage.

$$P = F \cdot I, \tag{A.12}$$

with the current I, and a voltage U. Inserting Equation (A.11) into Equation (A.12) leads to

$$P = N \cdot A\frac{\mathrm{d}B}{\mathrm{d}t}I. \tag{A.13}$$

The work W performed is given by

$$W = P \cdot t, \tag{A.14}$$

leading to

$$\mathrm{d}W = P\mathrm{d}t.$$

Inserting Equation (A.13) leads to

$$\mathrm{d}W = \left(N \cdot A \cdot I \frac{\mathrm{d}B}{\mathrm{d}t}\right) \mathrm{d}t \tag{A.15}$$

$$= N \cdot A \cdot I \mathrm{d}B. \tag{A.16}$$

For a coil, the relation of magnetic field strength H and coil parameters is given by

$$H = \frac{N \cdot I}{l}. \tag{A.17}$$

Inserting Equation (A.17) into Equation (A.16) yields

$$\mathrm{d}W = H \cdot l \cdot A \mathrm{d}B. \tag{A.18}$$

For a whole cycle Equation (A.18) is integrated giving

$$\oint \mathrm{d}W = \oint H \cdot l \cdot A \mathrm{d}B$$

$$W = A \cdot l \oint H \mathrm{d}B.$$

A.2 Original Images for Figure 4.18

In fig. 4.18, contrast-adjusted images are shown for visibility reasons. Here the original images are given.

(a) Fluorescence image of a standard cell sample (FluoCells™ #2, invitrogen, Thermo Fisher Scientific, Waltham, Massachusetts, USA). The excitation wavelength is (575.0 ± 12.5) nm Detected is Fluorescence of the wavelength of 457 nm, 530 nm, and 628 nm. Mainly visible are actin filaments, stained with Texas Red™-X Phalloidin.

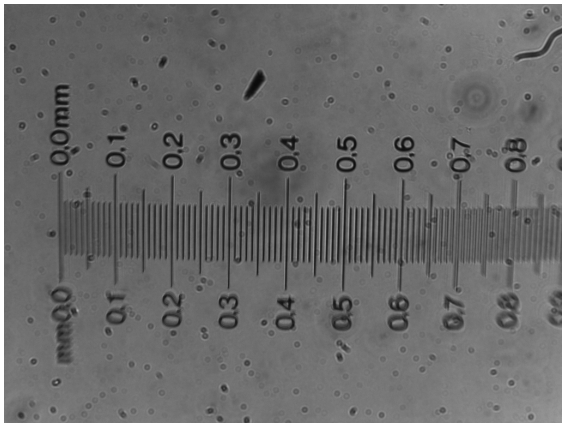

(b) Bright field image of a stage micrometer. In the image, dust particles can be seen; this is due to the limited accessibility, which prohibits frequent cleaning.

Figure A.2: Original contrast images for fig. 4.18.The scale of both images is the same. An additional scale bar is not given since Figure A.2b is the image of a physical scale bar. Please note that a) might seem to be completely black, dependent on screen or printer settings.

B Single Particle Tracking Supplementary Information

B.1 Parts of the Microscopy Setup

Part	**Used Item**	**Manufacturer/Reseller**
Microscope body	IX73 inverted microscope	Olympus, Tokyo, Japan
LED light source	SOLA SE 2	Lumencor, Beaverton, OR, USA
far red excitation filter	F39-638 635/18 BrightLine HC	AHF Analysentechnik AG, Tübingen, Germany
red excitation filter	F37-563 563/9 BrightLine HC	AHF Analysentechnik AG, Tübingen, Germany
green excitation filter	F39-483 482/18 BrightLine HC	AHF Analysentechnik AG, Tübingen, Germany
blue excitation filter	F39-378 378/52 BrightLine HC	AHF Analysentechnik AG, Tübingen, Germany
far red emission filter	F76-635 635 LP Edge Basic Longpass	AHF Analysentechnik AG, Tübingen, Germany
red emission filter	F39-595 595/31 BrightLine HC	AHF Analysentechnik AG, Tübingen, Germany
green emission filter	F37-527 525/39 BrightLine HC	AHF Analysentechnik AG, Tübingen, Germany
blue emission filter	F37-443 442/42 BrightLine HC	AHF Analysentechnik AG, Tübingen, Germany

50/50 beamsplitter		AHF Analysentechnik AG, Tübingen, Germany
Camera	Prime 95 B	TELEDYNE PHOTOMETRICS, Tucson, Arizona, USA
LED light source	SOLASE2	Lumencor, Beaverton Oregon USA
638 Laser	Cobolt 06-MLD	HÜBNER Photonics Kassel,Germany
561 Laser	Cobolt Jive	HÜBNER Photonics Kassel,Germany
488 Laser	Cobolt 06-MLD	HÜBNER Photonics Kassel,Germany
405 Laser	Cobolt 06-MLD	HÜBNER Photonics Kassel,Germany
AOTF	nC-400.650-TN	AA Opto-Electronic Orsay, France
Polarizing Beam splitter	PBS101	Thorlabs, Newton, New Jersey, USA
$\lambda/2$ wave plate	AHWP10M-600	Thorlabs, Newton, New Jersey, USA
Optical Fiber	KineFlex fibre	Qioptiq Photonics GmbH & CO. KG, Göttingen, Germany
Fiber mounts	kinematix fibre mount	Qioptiq Photonics GmbH & CO. KG, Göttingen, Germany
First lens	AC080-010-A-ML	Thorlabs, Newton, New Jersey, USA

second lens	AC508-180-A-ML	Thorlabs, Newton, New Jersey, USA
Third lens	AC254-200-A-ML	Thorlabs, Newton, New Jersey, USA
Quadband filter	BS R406/488/561/635 für Laser Weitfeld Quadb. Set	AHF Analysentechnik AG, Tübingen, Germany
objective	TIRF UA-PON100XOTIRF	Olympus,Tokyo, Japan
613 nm Longapss	LaserMux F38-M05 LM01-613-25	AHF Analysentechnik AG, Tübingen, Germany
552 nm Longapss	LaserMux F38-M04 LM01-552-25	AHF Analysentechnik AG, Tübingen, Germany
427 nm Longapss	LaserMux F38-M01 LM01-427-25	AHF Analysentechnik AG, Tübingen, Germany

Table B.1: List of the parts used in the fluorescence microscopy setup.

B.2 Expression for the Mean Square Displacement from the Langevin Equation

The Langevin equation describes a particle's motion in a fluid or gas in the presence of a random force. A prime example of this motion type is Brownian motion. An often-used derivation is represented once again. The Langevin equation is given by

$$\frac{\mathrm{d}v\left(t\right)}{\mathrm{d}t} = -\xi v\left(t\right) + F\left(t\right), \tag{B.1}$$

where v is the velocity of a particle, t the time, ξ is a drag coefficient, and F is an external random force acting on the particle [110]. The formal solution to Equation (B.1) is given by

$$v\left(t\right) = v\left(0\right)\mathrm{e}^{-\frac{\xi}{m}t} + \frac{1}{m}\int_0^t f\left(t_1\right)\mathrm{e}^{-\frac{\xi}{m}(t-t_1)}\mathrm{d}t_1.$$

Starting at this expression for $v(t)$ an expression for $x(t)$ can be found which is given by

$$x(t) = \int_0^t v(t_1)\,\mathrm{d}t_1. \tag{B.2}$$

Utilizing Equation (B.2) the mean squared displacement $\left\langle x(t)^2 \right\rangle_t$ can be calculated.

$$\left\langle x(t)^2 \right\rangle_t = \int_0^t \int_0^t \underbrace{\langle v(t_1), v(t_2)\rangle_t}_{\substack{\text{Velocity}\\ \text{autocorrelation}\\ \text{function}}} \mathrm{d}t_1 \mathrm{d}t_2.$$

The inner integral over t_1 can be split into two integrals one ranging from 0 to t_2 and a second one ranging from t_2 to t giving

$$\begin{aligned}\left\langle x(t)^2 \right\rangle_t &= \int_0^t \int_0^{t_2} \langle v(t_1), v(t_2)\rangle_t \,\mathrm{d}t_1 \mathrm{d}t_2 + \int_0^t \int_{t_2}^t \langle v(t_1), v(t_2)\rangle_t \,\mathrm{d}t_1 \mathrm{d}t_2 \\ &= \int_0^t \int_0^{t_2} \langle v(0), v(t_2 - t_1)\rangle_t \,\mathrm{d}t_1 \mathrm{d}t_2 + \int_0^t \int_{t_2}^t \langle v(t_1), v(t_2)\rangle_t \,\mathrm{d}t_1 \mathrm{d}t_2. \end{aligned} \tag{B.3}$$

By introducing the new variables $s = t_2$ and $\tau = t_1 - t_2$, with $\mathrm{d}\tau = \mathrm{d}t_1$ and $\mathrm{d}s = \mathrm{d}t_2$ Equation (B.3) can be rewritten to be

$$\begin{aligned} & 2\int_0^t \int_0^s \langle v(0), v(-\tau)\rangle_t \,\mathrm{d}\tau \mathrm{d}s \\ =& 2\int_0^t \int_0^s \langle v(\tau), v(0)\rangle_t \,\mathrm{d}\tau \mathrm{d}s \\ =& 2\int_0^t \langle v(\tau), v(0)\rangle_t \int_0^s \mathrm{d}s \quad \mathrm{d}\tau \\ =& 2\int_0^t \langle v(\tau), v(0)\rangle_t (t-\tau)\,\mathrm{d}\tau \end{aligned} \tag{B.4}$$

To further advance the calculation an expression for $\langle v(t_1), v(t_2)\rangle_t$ needs to be calculated

$$\begin{aligned} & \langle v(t_1), v(t_2)\rangle_t \\ =& \left\langle v(0)^2 \mathrm{e}^{-\frac{\xi}{m}\tau} \right\rangle_t + \frac{1}{m}\int_0^t \underbrace{\left\langle v(0) F(t_1) \mathrm{e}^{-\frac{\xi}{m}(\tau - t_1)} \right\rangle_t}_{\substack{\text{Uncorrelated}\\ =0}} \mathrm{d}t_1 \\ =& \left\langle v(0)^2 \right\rangle_t \mathrm{e}^{-\frac{\xi}{m}\tau}. \end{aligned} \tag{B.5}$$

Inserting Equation (B.5) in Equation (B.4) one arrives at

$$2\int_0^t (t-\tau)\left\langle v\left(0\right)^2\right\rangle_t \mathrm{e}^{-\frac{\xi}{m}\tau}\mathrm{d}\tau. \tag{B.6}$$

In combination with the equipartition theorem in thermodynamic equilibrium, given by

$$\frac{1}{2}m\left\langle v\left(0\right)^2\right\rangle = \frac{1}{2}k_{\mathrm{B}}T,$$

with the Boltzmann constant k_{B}, and the absolute temperature T, Equation (B.6) can be rewritten to be

$$\begin{aligned} &2\int_0^t (t-\tau)\,\frac{k_{\mathrm{B}}T}{m}\mathrm{e}^{-\frac{\xi}{m}\tau} \\ =&2\frac{k_{\mathrm{B}}T}{m}\int_0^t (t-\tau)\,\mathrm{e}^{-\frac{\xi}{m}\tau}. \end{aligned}$$

Integration in parts leads to

$$\begin{aligned} &\frac{2k_{\mathrm{B}}T}{m}\left\{\left[-\frac{m}{\xi}\left(t-\tau\right)\mathrm{e}^{-\frac{\xi}{m}\tau}\right]_0^t \int_0^t \frac{m}{\xi}\mathrm{e}^{-\frac{\xi}{m}\tau}\mathrm{d}\tau\right\} \\ =&\frac{2k_{\mathrm{B}}T}{m}\left\{\frac{m}{\xi}t-\left[.\left(\frac{m}{\xi}\right)^2\mathrm{e}^{-\frac{\xi}{m}\tau}\right]_0^t\right\} \\ =&\frac{2k_{\mathrm{B}}T}{\xi}\left\{t+\frac{m}{\xi}\mathrm{e}^{-\frac{\xi}{m}t}-\frac{m}{\xi}\right\}. \end{aligned}$$

In the case of a light particle with high drag $m/\xi \lll t$, this can be approximated by

$$\left\langle x\left(t\right)^2\right\rangle_t \approx \frac{2k_{\mathrm{T}}}{\xi}t = 2Dt,$$

with the diffusion constant D given by the Einstein relation

$$D = \frac{k_{\mathrm{B}}T}{\xi}.$$

B.3 Matlab Algorithms

In this appendix, the source code of the single particle evaluation script is given.

B.1 evaluationsaving.m

`evaluationsaving.m` is the main script of the evaluation code explained in Section 9.2.1.

```
%
% This program evaluates tracks.
%
% The results are saved in a cell with the following format
%
% Tracknumber ; Trackdata ; TrackMSD ; AboveData ; BelowData ; Settings
% 1
% .
% .
% .
% Tracknumber
%
% Trackdata contains
%
% Pointnumber ; x-coordinate ; y-coordinate ; Pointdensity
% 1
% .
% .
% .
% Pointnumber
%
% Above/BelowData contains
%
% Pointnumber from Track ; Section ID ; Section Alpha ; Section D ; Section
% x-coordinate ; Section y-coordinate
%
close all
clear
%% Input parameters for the different algorithm parts


% settings for the point density estimator for lower an upper threshold

pointnumber = 1000;   %number of simulated steps
                                        %used for estimation of the point
                                        %density

sigmalow = 10;          %sigma for the angle distribution
%mode setting of the estimator

%same as before but for upper threshold
sigmaup = 180;

holewidth = 10;


```

```
%setting for the splittign algorithm
splittingset = struct();
splittingset.filtersigma = 7;   % sigma of the smoothing filter
splittingset.lowercorr = 0.1;   % adjusting factors to minimize unassigned
                                    % parts
splittingset.uppercorr = 0.15;   % make sure that lowercorr+uppercorr <=1

%% loading coordinates

[file,path] = uigetfile('*','Multiselect','on');

if ischar(file)
  filenumber = 1;
end
if iscell (file)
  filenumber = size(file,2);
end
if ~exist(strcat(path,'\Results'),'dir')
   mkdir(strcat(path,'\Results'));
end


%% processing loop for individual files
%please note that the loop is parfor ready if the computer is capable
for p = 1:filenumber

    %waitbar for progress monitoring
    loadingbar = waitbar(0,strcat('Processing', num2str(p)));

    %introducing a local version of splittingset for parallelization
    splittingsetuse = splittingset;

    %loading x and y coordinates from files
    if filenumber == 1
        readfile = file;
    else
        readfile = char(file(p));
    end

    xtemp = load(strcat(path,'\',readfile));
    ytemp = load(strcat(path,'\y',readfile(2:end)));


    x = cell2mat(struct2cell(xtemp));
    y = cell2mat(struct2cell(ytemp));

    tracknumber = size(x,1);

    localizedvalues= zeros(1,4);
    %r =1;

    Results = cell(tracknumber,6);
%%  loop for evaluating individual tracks
    for k = 1:tracknumber

        if mod(k,round(tracknumber/10)) == 0
           waitbar(k/tracknumber, loadingbar, ...
               strcat('Processing', num2str(p)))
```

```
        end

        %introducing trackdata variable

        trackdata = zeros(size(x,2),3);
        trackdata(:,1) = 1:size(x,2);
        trackdata(:,2) = x(k,:);
        trackdata(:,3) = y(k,:);


        trackdata(trackdata(:,2) ==0,2)=NaN;
        trackdata(trackdata(:,3) ==0,3)=NaN;
        %determining step distribution of track
        res = stephistogram(trackdata);
        %setting variables
        densityset = struct();
        densityset.stepwidth = res(2);
        densityset.xrad = 5*res(2);
        densityset.holewidth = 10;

        pdestimatorsetup = struct();
        pdestimatorsetup.mode = 'up';
        pdestimatorsetup.sigma = sigmaup;
        pdestimatorsetup.pointnumber = pointnumber;
        pdestimatorsetup.holewidth = holewidth;

        pdestimatorsetlow = struct();
        pdestimatorsetlow.mode = 'low';
        pdestimatorsetlow.sigma = sigmalow;
        pdestimatorsetlow.pointnumber = pointnumber;
        pdestimatorsetlow.holewidth = holewidth;
        %calculating point density
        trackdata= pdcalc(trackdata,holewidth);
        splittingsetuse.lowerthreshold = ...
            pdestimator(trackdata,pdestimatorsetlow);
        splittingsetuse.upperthreshold = ...
            pdestimator(trackdata,pdestimatorsetup);
        %splitting track into segments
        [above, between, below] = ...
            trackseparator(trackdata,splittingsetuse);
        %calculate MSD
        msdB = calcmsd(below);
        alphaB = zeros(size(msdB,1),1);
        DB = zeros(size(msdB,1),1);

        msdBC = calcmsd(below);
        alphaBC = zeros(size(msdB,1),1);
        DBC = zeros(size(msdB,1),1);
        %perfomring alpha D fit
        for n = 1:size(msdB,1)
            below(below == 0) =NaN;
            if size(find(~isnan(below(n,:,2))),2)> 29 && ...
                    (size(find(~isnan(below(n,:,2))),2)...
                    /find(~isnan(below(n,:,2)),1,'last')) > 0.9
                [alphaB(n),DB(n)] = alphadfit(msdB(n,:));
            else
               alphaB(n) = NaN;
               DB(n) = NaN;
```

```
163             end
164             1;
165         end
166
167         msdA = calcmsd(above);
168         alphaA = zeros(size(msdA,1),1);
169         DA = zeros(size(msdA,1),1);
170
171         msdAC = calcmsd(above);
172         alphaAC = zeros(size(msdA,1),1);
173         DAC = zeros(size(msdA,1),1);
174
175         above(above == 0) =NaN;
176         for n = 1:size(msdA,1)
177             if size(find(~isnan(above(n,:,2))),2)> 30 && ...
178                     (find(~isnan(above(n,:,2)),1,'last')...
179                     /size(find(~isnan(above(n,:,2))),2)) > 0.9
180                 [alphaA(n),DA(n)] = alphadfit(msdA(n,:));
181             else
182                alphaA(n) = NaN;
183                DA(n) = NaN;
184             end
185             1;
186         end
187
188
189         % saving the data
190
191         Results{k,1} = k;
192         Results{k,2} = trackdata;
193         AboveData = cell(size(above,1),6);
194         for mm = 1:size(above,1)
195             AboveData{mm,1} = mm;
196             above(above == 0) = NaN;
197             AboveData{mm,2} = above(mm,:,:);
198             AboveData{mm,3} = alphaA(mm,1);
199             AboveData{mm,4} = DA(mm,1);
200             AboveData{mm,5} = alphaAC(mm,1);
201             AboveData{mm,6} = DAC(mm,1);
202         end
203         Results{k,4}= AboveData;
204         BelowData = cell(size(above,1),6);
205         for mm = 1:size(below,1)
206             BelowData{mm,1} = mm;
207             below(below == 0) = NaN;
208             BelowData{mm,2} = below(mm,:,:);
209             BelowData{mm,3} = alphaB(mm,1);
210             BelowData{mm,4} = DB(mm,1);
211             BelowData{mm,5} = alphaBC(mm,1);
212             BelowData{mm,6} = DBC(mm,1);
213         end
214         Results{k,5}= BelowData;
215         Settings= cell(1,4);
216         Settings{1,1} = densityset;
217         Settings{1,2} = pdestimatorsetlow;
218         Settings{1,3} = pdestimatorsetup;
219         Settings{1,4} = splittingsetuse;
220         Results{k,6} = Settings;
```

```
    end

    if ischar(file)
        savefile = file;
    end

    if iscell (file)
        savefile = file{p};
    end
    waitbar(1,loadingbar,'Saving')
    resultssaver(strcat(path,'Results\',savefile(2:end-4)), Results);
    close(loadingbar)
end
```

B.2 alphadfit.m

`alphadfit.m` determines the α and D values for each track segment.

```
%
%  alpha d fitting based on linear fitting to double logarithmized data
% using log(MSD) = log(4D) + log(tau)alpha
%
function [alpha,D] = alphadfit(msd)
    %determine length
    length = find(~isnan(msd),1,'last');
    usedlength = floor(length/4);
    %if the statistics for MSD are sufficient
    if usedlength >= 7
        %initializing the fit x data in multiples of accuisition times.
        x = 1:usedlength;
        %deleting unused entries in MSD
        msd(usedlength+1:end) = [];
        %defining fit options for linera fit
        ft = fittype( 'a+b.*x', 'independent', 'x', 'dependent', 'y' );
        opts = fitoptions( 'Method', 'NonlinearLeastSquares' );
        opts.Display = 'Off';
        opts.StartPoint = [0.5 1];
        opts.Lower = [-10 0];
        opts.Upper = [5 2];
        opts.Weights = 4*usedlength:-1:3*usedlength+1;
        %performing fit on logarithmised data
        x = log(x);
        y = log(msd);
        [fitresult,~] = fit(x',y',ft,opts);
        fitCo = coeffvalues(fitresult);
        %calculating output values
        alpha = fitCo(2);
        D = 0.25*exp(fitCo(1));
    else
        alpha = NaN;
        D=NaN;
    end
end
```

B.3 calcmsd.m

`calcmsd.m` is a small subroutine which calculates the MSD of track data.

```
%{
calculating the measn square displacement
Input: m x n x 3 double vector of the track segment data
Output: m x n vector containing the msd for all track segments
%}

function msd = calcmsd(tracks)
    %initializing msd variable
    msd = zeros(size(tracks,1),size(tracks,2));
    %loop over track segments handed over
    for m = 1:size(tracks,1)

        valueid = find(tracks(m,:,2));
        %valueid = [valueid];
        length = size(valueid,2);
        %loop over all possible stepwidth
        for k = 1:length-1
            %calculating x and y distance matrices
            x1 = tracks(m,valueid,2);
            x2 = circshift(x1,-k,2);
            xcalc = x1-x2;
            y1 = tracks(m,valueid,3);
            y2 = circshift(y1,-k,2);
            ycalc = y1-y2;
            %calculating Euclidean distance
            distance = xcalc.^2+ycalc.^2;
            msd(m,k) = mean(distance(1:end-k),'omitnan');
        end
    end
  msd(msd == 0) = NaN;
end
```

B.4 distributionfunc.m

`distributionfunc.m` is the externalized skew Gaussian function, used in `stephistogram.m` and `skewgaussgen.m`.

```
%
%skew normal distribution
%
function res = distributionfunc(x,sigma,mu)
    res = 2.*normcdf(x,mu,sigma).* normpdf(x,mu,sigma);
end
```

B.5 fillnan.m

`fillnan.m` fills the gaps in the track for a correct calculation of the point density.

```
%
%Function for linear interpolating points in gaps between track segemnts
%
function filledtrack = fillnan(track)
    %finding NaN positions
    nans = isnan(track(:,2));
    %finding start and end of each gap
    nanid(:,1) = nans == 1 & circshift(nans,1,1) == 0;
    nanid(:,2) = nans == 1 & circshift(nans,-1,1) == 0;
    nanstart = find(nanid(:,1));
    nanend = find(nanid(:,2));
    %determine amount of gaps
    amountnan = size(nanstart);
    filledtrack = track;
    %filling the gaps
    for ii = 1:amountnan
        %if condition to exclude NaN entrys after track end
        if nanend(ii) ~= size(track,1)
            nanlength = (nanend(ii)-nanstart(ii)+1);
            filledtrack(nanstart(ii):nanend(ii),2) =...
                track(nanstart(ii)-1,2)+(1:nanlength)...
                .*(track(nanend(ii)+1,2)-track(nanstart(ii)-1,2))...
                ./(nanlength+1);
            filledtrack(nanstart(ii):nanend(ii),3) =...
                track(nanstart(ii)-1,3)+(1:nanlength)...
                .*(track(nanend(ii)+1,3)-track(nanstart(ii)-1,3))...
                ./(nanlength+1);
        end
    end

end
```

B.6 modgauss2.m

`modgauss2.m` generates a Gaussian distribution for angles or step widths.

```
%%function to genrate a gaussian distribution
function valuesfilled = modgauss2(valuesall,var)
  mode = var.mode;
  indexall = 1:size(valuesall,1);
  %loop for angle generation
  if strcmp('angle',mode)
    done = 0;
    sigma = var.sigma;
    mu = var.mu;

    values = valuesall(indexall,:);
    index  = 1:size(values,1);
    while done ==0
        %generating values between
        values(index,2) = rand(size(index)).*360-180;
        %confining the genrated values to the interval of +/- 180 degree
        %if mu is different than zero
        if values(index,2)+mu > 180
          values(index,2) = values(index,2)-360;
        end
        if values(index,2)+mu < -180
          values(index,2) = values(index,2)+360;
        end
        %generating random values
        values(index,3) = rand(size(index));
        %calculating the control values
        values(index,6) = ((exp(-0.5.*((values(index,2)-mu)./sigma).^2))...
            ./(sigma.*sqrt(2.*pi()))) / ((exp(-0.5.*((0)./sigma).^2))...
            ./(sigma.*sqrt(2.*pi())));
        index = find(values(:,6)<values(:,3));
        if size(index,1) ==0
          done =1;
        end
    end
    valuesall(indexall,:) = values;
    valuesfilled = valuesall;
  end
  %loop for step mode
  if strcmp('step',mode)
    done = 0;
    %calculating sigma from given width
    width = var.width;
    mu = var.mu;
    sigma = width/6;
    values = valuesall(indexall,:);
    index  = 1:size(values,1);
    while done ==0
        %generating values within the interval
        values(index,4) = rand(size(index)).*width- width/2 + mu ;
        values(index,5) = rand(size(index));
        %calculating control values
        values(index,7) = ((exp(-0.5.*((values(index,4)-mu)./sigma).^2))...
            ./(sigma.*sqrt(2.*pi()))  / ((exp(-0.5.*((0)./sigma).^2))...
            ./(sigma.*sqrt(2.*pi()))  ;
```

```
        index = find(values(:,7)<values(:,5));
        if size(index,1) ==0
          done =1;
        end

    end
    valuesall(indexall,:) = values;
    valuesfilled = valuesall;
  end
end
```

B.7 pdcalc.m

`pdcalc.m` is a subroutine which calculates the PDM for a given track.

```
%
%Function to calculate th point density
%

function [density] = pdcalc(value,holewidth)
    %interpolating values for NaN gaps
    valuefill = fillnan(value);
    x = valuefill(:,2)';
    y = valuefill(:,3)';
    %calculating distance matrices in x and y direction
    xdistmat = x-x';
    ydistmat = y-y';
    %calculating step sizes
    stepsize = sqrt(diff(x).^2+diff(y).^2);
    stepsize(1,end+1) = stepsize(1,end);
    %determining local radius for pd calculation
    stepsize = movmean(stepsize,5);
    radius = 5.*stepsize;
    radius = imgaussfilt(radius,3);
    valid = zeros(size(xdistmat));
    %calculating validitymatrix
    for ii = 1:size(xdistmat,1)
        valid(ii,:) = ((xdistmat(ii,:)./radius(1,ii)).^2 ...
            + (ydistmat(ii,:)./radius(1,:)).^2) < 1;
    end
    %removing point which are inside the radius after the track returned
    validbefore = zeros(size(valid));
    validafter = validbefore;
    holearray = zeros(1,holewidth);
    for ii = 1:size(valid,1)
        temp = circshift(valid(ii,:),-ii+1);
        temp1=temp;
        lastvalidpos = min(strfind(temp,holearray));
        temp1(lastvalidpos+1:end) = 0;
        validafter(ii,:) = circshift(temp1,ii-1);
        temp2 = fliplr(temp);
        firstvalidpos = min(strfind(temp2,holearray));
        temp2(firstvalidpos+1:end) = 0;
        validbefore(ii,:) = circshift(fliplr(temp2),ii-1);
    end
    %calculating resulting point density
    result = sum(validafter,2)+sum(validbefore,2)-1;
    density = zeros(size(value,1),4);
    density(:,1:3) = value(:,1:3);
    density(:,4) = result;
end
```

B.8 pdestimator.m

`pdestimator.m` is a subroutine that simulates the point density of a track with a given relative angle and step width distribution.

```
%
%This program simulates the point density for expected track.
%
function pdthreshold = pdestimator(trackdata,var)
    pointnumber = var.pointnumber;
    holewidth = var.holewidth;
    values = zeros(pointnumber,9);
    values(:,1) = 1:pointnumber;
    %gathering step width distribution
    [distparam] = stephistogram(trackdata);
    angleset = struct();
    angleset.mode = 'angle';
    angleset.mu = 0;
    angleset.sigma = var.sigma;
    stepset = struct();
    stepset.mode = 'step';
    stepset.mu = distparam(3);
    stepset.sigma = distparam(2);
    %simulating the angledistribution for the track
    values =modgauss2(values,angleset);
    %simulating the stepdistribution for the track
    values =skewgaussgen(values,stepset);
    %calculating x and y coordinates
    for k = 2:size(values,1)
      values(k,8) = values(k-1,8) + values(k,4).*cosd(sum(values(1:k,2)));
      values(k,9) = values(k-1,9) + values(k,4).*sind(sum(values(1:k,2)));
    end
    %conversion of variable for pdcalc
    workval = zeros(pointnumber:3);
    workval(:,1) = values(:,1);
    workval(:,2) = values(:,8);
    workval(:,3) = values(:,9);
    %calculating point denisty for simualted track
    density = pdcalc(workval,holewidth);
    %determining threshold
    if strcmp(var.mode, 'low')
        pdthreshold = max(density(:,4));
    end
    if strcmp(var.mode, 'up')
        pdthreshold = median(density(:,4));
    end
end
```

B.9 skewgaussgen.m

`skewgaussgen.m` generates a skew Gaussian distribution for angles or step widths.

```
%function to genrate a skew gaussian distribution
function valuesfilled = skewgaussgen(valuesall,var)
 mode = var.mode;
 indexall = 1:size(valuesall,1);
 %function for angle distribution
 if strcmp('angle',mode)
    done = 0;
    sigma = var.sigma;
    mu = var.mu;
    values = valuesall(indexall,:);
    index  = 1:size(values,1);
    %generating the angle values
    while done ==0
        %wraping angles largern/smaller than 180/-180 around
        values(index,2) = rand(size(index)).*360-180;
        if values(index,2)+mu > 180
          values(index,2) = values(index,2)-360;
        end
        if values(index,2)+mu < -180
          values(index,2) = values(index,2)+360;
        end
        %generating and checking control numbers
        values(index,3) = rand(size(index));
        values(index,6) = distributionfunc(values(index,2),sigma,mu)...
            /distributionfunc(mu,sigma,mu);
        index = find(values(:,6)<values(:,3));
        if size(index,1) ==0
          done =1;
        end
    end
    valuesall(indexall,:) = values;
    valuesfilled = valuesall;
 end
 if strcmp('step',mode)
    done = 0;
    sigma = var.sigma;

    mu = var.mu;
    %setting width of simulated data
    width = 6*sigma;
    values = valuesall(indexall,:);
    index  = 1:size(values,1)';
    %generating the step values
    while done ==0
        %generating and checking control numbers
        values(index,4) = rand(size(index)).*width- width/2 + mu ;
        values(index,5) = rand(size(index));
        values(index,7) = distributionfunc(values(index,4),sigma,mu)...
            /distributionfunc(mu,sigma,mu);
        index = find(values(:,7)<values(:,5));
        if size(index,1) ==0
          done =1;
        end
    end
```

```
    valuesall(indexall,:) = values;
    valuesfilled = valuesall;
  end
end
```

B.10 stephistogram.m

`stephistogram.m` determines the distribution of the step width for a given track.

```
%Function for determining the step width distribution of a track
function [res] =  stephistogram(track)
%calculating distances
distance = sqrt(diff(track(:,2)).^2+diff(track(:,3)).^2);
%generating histogram for tailed distributions
[values,bins] = histcounts(distance,'BinMethod','fd');
%calculating middle of bins
binshift = circshift(bins,-1,2);
means = (bins(1:end-1)+binshift(1:end-1))/2;
%fitting of skew Ggaussian
opts = optimset('Display','off');
fitfunction = @(p,x) p(1).*distributionfunc(x,p(2),p(3));
res = lsqcurvefit(fitfunction,[max(values),1,1],means,values,[],[],opts);
end
```

B.11 trackseparator.m

`trackseparator.m` splits the track data into different types of suspected motion according to the thresholds estimated by `pdestimator`, with a user-defined correction value.

```
%Programm for track separation
function [above, between, below] = trackseparator(trackdata,var)
    upperthresh = var.upperthreshold;
    lowerthresh = var.lowerthreshold;
    filtersigma = var.filtersigma;
    uppercorr = var.uppercorr;
    lowercorr = var.lowercorr;
    %adjusting the upper and lower threshold
    threshdiff = (upperthresh-lowerthresh);
    upperthresh = upperthresh-uppercorr .* threshdiff;
    lowerthresh = lowerthresh+lowercorr .* threshdiff;
    %smoothing the point density
    density = trackdata(:,4);
    smoothdens  = imgaussfilt(density, filtersigma);
    %determining the segments above between and below the thresholds
    aboveid = smoothdens >= upperthresh;
    belowid = smoothdens <= lowerthresh;
    betweenid = smoothdens < upperthresh & smoothdens > lowerthresh;
    %finding ids of segments
    aboveidfind = zeros(size(aboveid,1)+1,1);
    aboveidfind(1:end-1) = aboveid;
    belowidfind = zeros(size(belowid,1)+1,1);
```

```
    belowidfind(1:end-1) = belowid;
    betweenidfind = zeros(size(betweenid,1)+1,1);
    betweenidfind(1:end-1) = belowid;
    %adds a zero at the end to find
    %beginnings if the start and end type of motion is the same
    abovestart = aboveidfind == 1 & circshift(aboveidfind,1,1) == 0;
    aboveend = aboveidfind == 1 & circshift(aboveidfind,-1,1) == 0;
    belowstart = belowidfind == 1 & circshift(belowidfind,1,1) == 0;
    belowend = belowidfind == 1 & circshift(belowidfind,-1,1) == 0;
    betweenstart = betweenidfind == 1 & circshift(betweenidfind,1,1) == 0;
    betweenend = betweenidfind == 1 & circshift(betweenidfind,-1,1) == 0;
    %determining the ids of segments
    abovestartid = find(abovestart);
    aboveendid = find(aboveend);
    abovelength = aboveendid-abovestartid+1;

    belowstartid = find(belowstart);
    belowendid = find(belowend);
    belowlength = belowendid-belowstartid+1;

    betweenstartid = find(betweenstart);
    betweenendid = find(betweenend);
    betweenlength = betweenendid-betweenstartid+1;
    %filling the track segment into vectors
    above = zeros(size(abovelength,1),max(abovelength),3);
    below = zeros(size(belowlength,1),max(belowlength),3);
    between = zeros(size(betweenlength,1),max(betweenlength),3);

    for k = 1:size(abovelength,1)
      above(k,1:abovelength(k),1) = abovestartid(k):aboveendid(k);
      above(k,1:abovelength(k),2)= trackdata(abovestartid(k):aboveendid(k),2);
      above(k,1:abovelength(k),3)= trackdata(abovestartid(k):aboveendid(k),3);
    end

    for k = 1:size(belowlength,1)
      below(k,1:belowlength(k),1) = belowstartid(k):belowendid(k);
      below(k,1:belowlength(k),2)= trackdata(belowstartid(k):belowendid(k),2);
      below(k,1:belowlength(k),3)= trackdata(belowstartid(k):belowendid(k),3);
    end

    for k = 1:size(betweenlength,1)
      between(k,1:betweenlength(k),1) = betweenstartid(k):betweenendid(k);
      between(k,1:betweenlength(k),2)= trackdata(betweenstartid(k):betweenendid(k),2);
      between(k,1:betweenlength(k),3)= trackdata(betweenstartid(k):betweenendid(k),3);
    end
end
```

B.12 resultsaver.m

`resultsaver.m` is used to save the results in case a parallel loop is used, but is implemented in the non parallel version too.

```
%Saving results
function resultssaver(file,variable)
    %mode -v7.3 for large files
    save(file,'variable','-v7.3');
end
```

B.4 Used u-Track Parameters

Parameter	Value
Imaging mode	Widefield
Fluorophore	tagrfp
Excitation Wavelength (in nm)	561
Emission Wavelength (in nm)	584
Exposure Time (in seconds)	0.05
Pixel Size (nm)	110
Time Interval (sec)	0.051
Numerical Aperture	1.49
Camera Bit Depth (bit)	16
Object Type	[2D] Single particles
Detection Method	Point source detection
Kalman functions	Brownian + Directed motion models
Problem Dimension	2
Alpha value for asymmetry detection	0.1
Alpha value for moment scaling spectrum analysis	0.05
Maximum gaps to close	4
Minimum length of track segments from first step	1
Step1: Frame to frame linking	Brownian + Directed motion models
PSF Sigma(pxl)	1.2
Alpha	0.05
Fit Mode	xyAc

Max Fit Adjust (pixels)	2.4
Max # Mixtures	5
Redundancy Radius (pixels)	0.25
Fit Window Size (pixels)	5
Prefilter Points	enable
Fit Mixture Models	disable
Step2: Gap closing merging and splitting	Brownian + Directed motion models
Track analysis method	Track Analysis
Check and analyze asymmetric tracks	disable
Check to use threshold that balances the error rate of neighboring classes	disable
Method for calculating the confinement radius	Mean positional standard deviation

Table B.2: Parameters used by Paolino Salamone to perform the tracking of endosomes.

B.5 Original Images

Original Image Figure 9.8

In Figure 9.8, a contrast-enhanced image is shown; the original image is shown here.

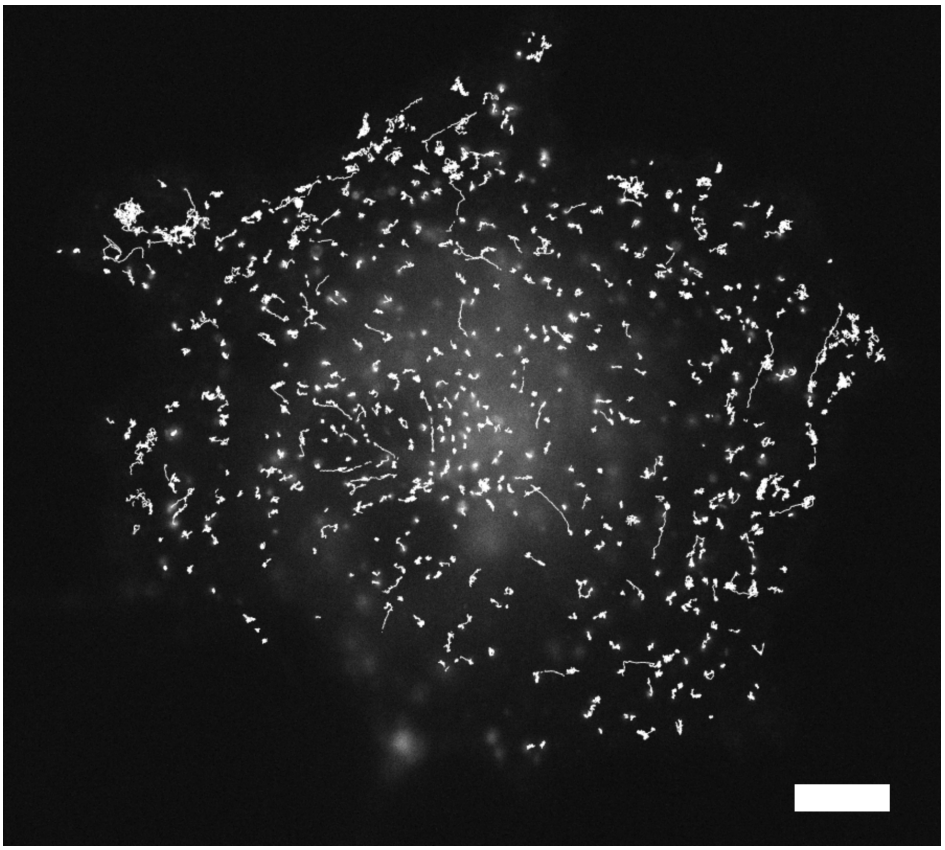

Figure B.1: Image of a cell with all tracks depicted. Acquisition time is 50 ms. The scalebar is 10 µm.

Original Image Figure 9.9

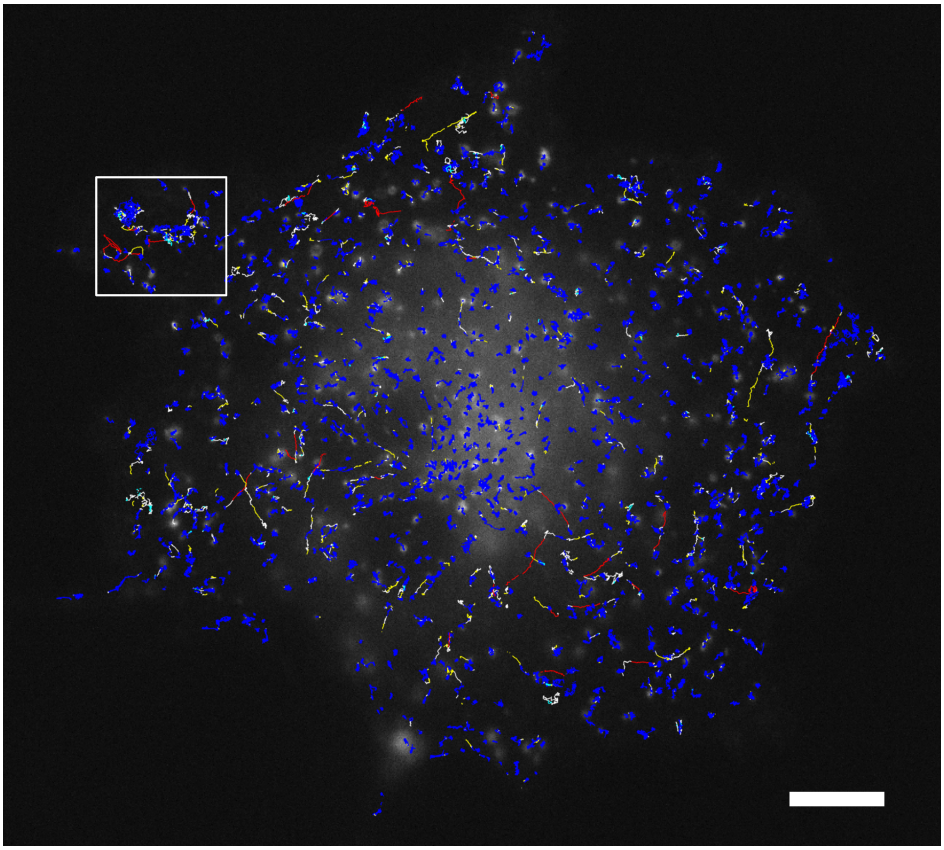

Figure B.2: Image of a cell with all tracks depicted. Acquisition time is 50 ms. The tracks are color-coded: Blue) Track segments that are above the upper threshold and longer than or equal to 29 Steps. Red) Track segments that are below the lower threshold and longer than or equal to 29 Steps. Cyan) Track segments that are above the upper threshold and shorter than 29 Steps. Yellow) Track segments that are below the lower threshold and shorter than 29 Steps. White) Track segments between the thresholds. The inset is magnified in Figure 9.10. The scalebar is 10 µm.

Corrigenda

This work is a revised version of the submitted document. Corrections of spelling-, punctuation-, typesetting-, positioning-, typographical-, grammatical-errors, and color adjustments or the like are not listed. Alterations made for additional information or clarification are given in the following. If not otherwise mentioned the altered parts are in bold.

- p.5) "...magnetosomes **with transmission electron microscopy measurements and properties thereof**. He also..."
- p.8) "$\oiint_{\partial V} \vec{D} \cdot \mathrm{d}\vec{A} = Q$"
- p.9) $\mu \coloneqq \frac{\boldsymbol{B}}{\boldsymbol{H}}$
- p.18) "... one object to another **by lattice vibrations. For electrical conductors the direct transport of thermal energy is also influenced by the movement of electrons, this effect is called Wiedemann–Franz law [42].**"
- p.32) "... $\mu_0 \approx 4\pi \cdot 10^{-7}\mathrm{N} \cdot \mathrm{A}^{-2}$..."
- p.36, Figure 4.2 caption) "... 3C90 (blue). **The winding ratio is 25:5 for solid lines and 5:25 for dashed lines. The shaded areas represent the measurement error.**"
- p.40, Figure 4.6 x-axis label) Frequency / **k**Hz
- p.45) "... currents inside the conductor. **As discussed in Section 4.1.2, there are differences of the coupling factor dependent on the direction of measurement (winding ratios of 25:5 and 5:25). In this measurement the differences are increased by the frequency adaption of the used cable on the secondary side, indicating less efficient coupling to stranded wire.** Due to the overall..."
- p. 59, **magnetic field strength** has been corrected to **magnetic flux density** in the caption of fig. 4.22 and the following paragraph.
- p.65, Figure 4.25) The x-axes are resized to cover the same range of data.
  Figure 4.25 caption) " ...investigated particles. **For the magnetosome measurements, diameters larger than 1000 nm are not shown due to the negligible amount.**"
- p.70) "... image of a **magnetosome** sample shortly before ..."
- p.71 fig. 4.27, p.72 Figure 4.28, p.73 fig. 4.29, p,75 Figure 4.30, 76 Figure 4.31,

p.78 Figure 4.32, p.79 Figure 4.33, p.81 fig. 4.34, p.84 fig. 4.36, p.85 fig. 4.37, p.87 Figure 4.38, p.88 fig. 4.39, p.89 fig. 4.40, p.91 fig. 4.42, p.91 fig. 4.43

In all captions the frequency of the measurement has been added in the format "The particles were measured at XX.XX kHz"

- p.72, fig. 4.28 caption) "... measurement area. **The shown data is recorded with a magnetosome sample.**"
- p.74) "**In this section multiple comparisons of measurements concerning different parameters are done. Due to the measurements being performed during the ongoing development of the setup, the measurement frequency varies. Therefore the measurements from one subsection are not necessarily comparable to measurements from another subsection. The frequency of the measurements is given in the caption of the data figures.**"
- p.80) "...$(18.1 \pm 2.2)\,°\mathrm{C}$ **for magnetosomes**."
- p.80) handling of the particles. **A further limitation to the interpretability is the difference in measurement frequencies. The underlying observation, that different particles show different heating behavior, however is unaffected, as the frequency influence is linear as given by eq. (2.16). The influence of the susceptibility is negligible as the measurement shows a flat slope in the region of 100 kHz (fig. 4.26). The magnetic field has the same amplitude in all measurements.**
- p.86) " ...concentration of 1 mg/mL. **The difference in measurement frequencies does not represent a limitation in the interpretability since the heating of the water sample is solely caused by the temperature rise of the magnet.**"
- p.105) "...two-dimensional case $\boldsymbol{(n=2)}$**, with** $a = \boldsymbol{2nD} = 4D$, $b = 1$, and $c = 0$."
- p.116) "$R'_{I,\mathrm{long}}\,(\mathrm{gap}) = \mathbf{3}\sigma_I \cdot f\,(\mathrm{gap}) + \mathbf{3}\boldsymbol{\sigma}'_I \cdot f\,(\mathrm{gap})$"
- p.128, fig. 9.5 a x-axis label) "**Point Density**"
- p.132) "...directed motion, where the **path is elongated**. These classifications ..."
- p.146) ...the right-hand side leads to $\int \vec{B} \cdot \mathrm{d}\vec{s} = \mu_0 \boldsymbol{j} + \epsilon_0 \mu_0 \frac{\mathrm{d}\Phi_\mathrm{E}}{\mathrm{d}t}$. Just like above Equation (2.9) in the absence of polarization in combination with Equation (2.10) in the absence of magnetization $\left(\vec{H} = \frac{\vec{B}}{\mu_0}\right)$ leads to $\int \vec{H} \cdot \mathrm{d}\vec{s} = \boldsymbol{j} + \frac{\mathrm{d}\Phi_\mathrm{D}}{\mathrm{d}t}$.
- p.148) ... $P = U \cdot I$, **here** $\boldsymbol{U}$ **is given by the electromotive force, which is**

albeit the name indicating a force a voltage. $\boldsymbol{P = F \cdot I}$ ...

- p.150, fig. A.2b caption) "... physical scale bar. **Please note that a) might seem to be completely black, dependent on screen or printer settings.**"
- p. 175, fig. B.2) The adjusted image was shown again.

List of Figures

List of Tables

Acronyms

3M-PALS **M**ixed **M**ode **M**easurement-**P**hase **A**nalysis **L**ight **S**cattering.

AC **A**lternating **C**urrent.

ACS **A**lternating **C**urrent **S**usceptibility.

AMF **A**lternating **M**agnetic **F**ield.

AOTF **A**cousto-**O**ptical **T**unable **F**ilter.

AWG **A**merican **W**ire **G**auge.

BNF **B**ionized **N**ano **F**errite.

CAD **C**omputer **A**ided **D**esign.

CDF **C**ummulative **D**istribution **F**unction.

cf. Short for latin *conferatur*, compare.

DC **D**irected **C**urrent.

DLS **D**ynamic **L**ight **S**cattering.

e.g. ***e****xempli* ***g****ratia*, which means “for example”.

EDL **E**lectric **D**ouble **L**ayer.

ELS **E**lectrophoretic **L**ight **S**cattering.

EMF **E**lectro**m**otive **F**orce.

FFR **F**ast **F**ield **R**eversal.

FWHM **F**ull **W**idth at **H**alf **M**aximum.

IR **I**nfra**r**ed.

LDV **L**aser **D**oppler **V**elocimetry.

LED **L**ight **E**mitting **D**iode.

MNP **M**agnetic **N**ano **P**articles.

MSD **M**ean **S**quared **D**isplacement.

PBS **P**hosphate-**b**uffered **s**aline.

PDF **P**robability **D**ensity **F**unction.

PDM **P**oint **D**ensity **M**ap.

PP **P**eak to **P**eak.

PTFE **P**oly**t**etra**f**luoro**e**thylene.

RF **R**adio **F**requency.

RMS **R**oot **M**ean **S**quare.

SFR **S**low **F**ield **R**eversal.

SI International System of Units from french ***S**ystème **I**nternational d'Unités*.

SLP **S**pecific **L**oss **P**ower.

SMD **S**urface **M**ountable **D**evice.

SPT **S**ingle **P**article **T**racking.

TEM **T**ransverse **E**lectro**M**agnetic modes.

TEM **T**ransmission **E**lectron **M**icroscopy.

Bibliography

[1] James F Kasting, Daniel P Whitmire, and Ray T Reynolds. Habitable zones around main sequence stars. *Icarus*, 101(1):108–128, 1993.

[2] Hans-Christian Pape and Armin Kurtz. *Physiologie (Silbernagl), 9. Auflage*. Thieme, 2014.

[3] Christian H Brandts, Maryse Ndjavé, Wolfgang Graninger, and Peter G Kremsner. Effect of paracetamol on parasite clearance time in plasmodium falciparum malaria. *The Lancet*, 350(9079):704–709, 1997.

[4] Timothy F Doran, Catherine De Angelis, Rosemary A Baumgardner, and E David Mellits. Acetaminophen: more harm than good for chickenpox? *The Journal of pediatrics*, 114(6):1045–1048, 1989.

[5] Carl I Schulman, Nicholas Namias, James Doherty, Ronald J Manning, Pamela Li, Ahmed Elhaddad, David Lasko, Jose Amortegui, Christopher J Dy, Lucie Dlugasch, et al. The effect of antipyretic therapy upon outcomes in critically ill patients: a randomized, prospective study. *Surgical infections*, 6(4):369–375, 2005.

[6] Uwe Hobohm. Fever and cancer in perspective. *Cancer Immunology, Immunotherapy*, 50:391–396, 2001.

[7] Ralf Kleef, Wayne B Jonas, Wolfgang Knogler, and Werner Stenzinger. Fever, cancer incidence and spontaneous remissions. *Neuroimmunomodulation*, 9(2):55–64, 2001.

[8] Harry H LeVeen, Simon Wapnick, Vincent Piccone, Gerald Falk, and Nafis Ahmed. Tumor eradication by radiofrequency therapy: response in 21 patients. *Jama*, 235(20): 2198–2200, 1976.

[9] Ivan A Brezovich and John H Young. Hyperthermia with implanted electrodes. *Medical physics*, 8(1):79–84, 1981.

[10] EB Couple, JW Strohbehn, ED Bowers, and JE Walsh. Cancer therapy with localized hyperthermia using an invasive microwave system. *Journal of Microwave Power*, 14 (2):182–186, 1979.

[11] JW Strohbehn, ED Bowers, JE Walsh, and EB Douple. An invasive microwave antenna for locally-induced hyperthermia for cancer therapy. *The Journal of Microwave Power*, 14(4):339–350, 1979.

[12] Leonard S Taylor. Implantable radiators for cancer therapy by microwave hyperthermia. *Proceedings of the IEEE*, 68(1):142–149, 1980.

[13] RK Gilchrist, Richard Medal, William D Shorey, Russell C Hanselman, John C Parrott, and C Bruce Taylor. Selective inductive heating of lymph nodes. *Annals of surgery*, 146(4):596, 1957.

[14] Hassan A Albarqi, Ananiya A Demessie, Fahad Y Sabei, Abraham S Moses, Mikkel N Hansen, Pallavi Dhagat, Olena R Taratula, and Oleh Taratula. Systemically delivered magnetic hyperthermia for prostate cancer treatment. *Pharmaceutics*, 12(11):1020, 2020.

[15] Sudip Mondal, Panchanathan Manivasagan, Subramaniyan Bharathiraja, Madhappan Santha Moorthy, Van Tu Nguyen, Hye Hyun Kim, Seung Yun Nam, Kang Dae Lee, and Junghwan Oh. Hydroxyapatite coated iron oxide nanoparticles: a promising nanomaterial for magnetic hyperthermia cancer treatment. *Nanomaterials*, 7(12):426, 2017.

[16] Keon Mahmoudi, Alexandros Bouras, Dominique Bozec, Robert Ivkov, and Constantinos Hadjipanayis. Magnetic hyperthermia therapy for the treatment of glioblastoma: a review of the therapy's history, efficacy and application in humans. *International Journal of Hyperthermia*, 34(8):1316–1328, 2018.

[17] Elio Alberto Perigo, Gauvin Hemery, Olivier Sandre, Daniel Ortega, Eneko Garaio, Fernando Plazaola, and Francisco Javier Teran. Fundamentals and advances in magnetic hyperthermia. *Applied Physics Reviews*, 2(4), 2015.

[18] Quentin A Pankhurst, J Connolly, Stephen K Jones, and JJJopDAp Dobson. Applications of magnetic nanoparticles in biomedicine. *Journal of physics D: Applied physics*, 36(13):R167, 2003.

[19] QA Pankhurst, NTK Thanh, SK Jones, and J Dobson. Progress in applications of magnetic nanoparticles in biomedicine. *Journal of Physics D: Applied Physics*, 42(22): 224001, 2009.

[20] Heng Huang, Savas Delikanli, Hao Zeng, Denise M Ferkey, and Arnd Pralle. Remote control of ion channels and neurons through magnetic-field heating of nanoparticles. *Nature nanotechnology*, 5(8):602–606, 2010.

[21] Ritchie Chen, Gabriela Romero, Michael G Christiansen, Alan Mohr, and Polina Anikeeva. Wireless magnetothermal deep brain stimulation. *Science*, 347(6229):1477–1480, 2015.

[22] Dekel Rosenfeld, Alexander W Senko, Junsang Moon, Isabel Yick, Georgios Varnavides, Danijela Gregureć, Florian Koehler, Po-Han Chiang, Michael G Christiansen, Lisa Y Maeng, et al. Transgene-free remote magnetothermal regulation of adrenal hormones. *Science advances*, 6(15):eaaz3734, 2020.

[23] Sarah A Stanley, Jeremy Sauer, Ravi S Kane, Jonathan S Dordick, and Jeffrey M

Friedman. Remote regulation of glucose homeostasis in mice using genetically encoded nanoparticles. *Nature medicine*, 21(1):92–98, 2015.

[24] M Elisa de Sousa, Alejandra Carrea, Pedro Mendoza Zélis, Diego Muraca, Olga Mykhaylyk, Yolanda E Sosa, Rodolfo G Goya, Francisco H Sánchez, Ricardo A Dewey, and Marcela B Fernández van Raap. Stress-induced gene expression sensing intracellular heating triggered by magnetic hyperthermia. *The Journal of Physical Chemistry C*, 120(13):7339–7348, 2016.

[25] Courtney R Thomas, Daniel P Ferris, Jae-Hyun Lee, Eunjoo Choi, Mi Hyeon Cho, Eun Sook Kim, J Fraser Stoddart, Jeon-Soo Shin, Jinwoo Cheon, and Jeffrey I Zink. Noninvasive remote-controlled release of drug molecules in vitro using magnetic actuation of mechanized nanoparticles. *Journal of the American Chemical Society*, 132(31): 10623–10625, 2010.

[26] Andreas Riedinger, Pablo Guardia, Alberto Curcio, Miguel A Garcia, Roberto Cingolani, Liberato Manna, and Teresa Pellegrino. Subnanometer local temperature probing and remotely controlled drug release based on azo-functionalized iron oxide nanoparticles. *Nano letters*, 13(6):2399–2406, 2013.

[27] Esther Cazares-Cortes, Benjamin C Baker, Kana Nishimori, Makoto Ouchi, and François Tournilhac. Polymethacrylic acid shows thermoresponsivity in an organic solvent. *Macromolecules*, 52(15):5995–6004, 2019.

[28] P Fraga García, M Brammen, M Wolf, S Reinlein, M Freiherr Von Roman, and S Berensmeier. High-gradient magnetic separation for technical scale protein recovery using low cost magnetic nanoparticles. *Separation and purification technology*, 150: 29–36, 2015.

[29] Carlos Martinez-Boubeta and Konstantinos Simeonidis. Chapter 20 - magnetic nanoparticles for water purification. In Sabu Thomas, Daniel Pasquini, Shao-Yuan Leu, and Deepu A. Gopakumar, editors, *Nanoscale Materials in Water Purification*, Micro and Nano Technologies, pages 521–552. Elsevier, 2019. ISBN 978-0-12-813926-4. DOI: https://doi.org/10.1016/B978-0-12-813926-4.00026-4. URL https://www.sciencedirect.com/science/article/pii/B9780128139264000264.

[30] Jing Hu, Irene MC Lo, and Guohua Chen. Comparative study of various magnetic nanoparticles for cr (vi) removal. *Separation and Purification Technology*, 56(3):249–256, 2007.

[31] Binh T Mai, Soraia Fernandes, Preethi B Balakrishnan, and Teresa Pellegrino. Nanosystems based on magnetic nanoparticles and thermo-or ph-responsive polymers: An update and future perspectives. *Accounts of chemical research*, 51(5):999–1013, 2018.

[32] James Clerk Maxwell. Viii. a dynamical theory of the electromagnetic field. *Philosophical transactions of the Royal Society of London*, (155):459–512, 1865.

[33] Siegmund Brandt, Hans Dieter Dahmen, Claus Grupen, and Tilo Stroh. *Die Maxwell-Gleichungen*, pages 1–12. Springer Berlin Heidelberg, Berlin, Heidelberg, 2021. ISBN 978-3-662-64313-6. DOI: 10.1007/978-3-662-64313-6_1. URL https://doi.org/10.1007/978-3-662-64313-6_1.

[34] Wolfgang Demtröder. *Experimentalphysik 2*, volume 2. Springer, 1999.

[35] Wolfgang Nolting and Wolfgang Nolting. Magnetostatik. *Grundkurs Theoretische Physik 3: Elektrodynamik*, pages 173–220, 2013.

[36] Walther Meissner and Robert Ochsenfeld. Ein neuer effekt bei eintritt der supraleitfähigkeit. *Naturwissenschaften*, 21(44):787–788, 1933.

[37] metglas. Magnetic materials, 2023. URL https://metglas.com/magnetic-materials/. Metglas 2714A Alloy visited: 2023.02.01.

[38] Mathias Getzlaff. *Fundamentals of magnetism*. Springer Science & Business Media, 2007.

[39] Ronald E Rosensweig. Heating magnetic fluid with alternating magnetic field. *Journal of magnetism and magnetic materials*, 252:370–374, 2002.

[40] Robert J Deissler, Yong Wu, and Michael A Martens. Dependence of brownian and néel relaxation times on magnetic field strength. *Medical physics*, 41(1):012301, 2014.

[41] Harry Pfeifer and Herbert Schmiedel. *Wärmekapazitäten*, pages 112–116. Vieweg+Teubner Verlag, Wiesbaden, 1997. ISBN 978-3-322-83423-2. DOI: 10.1007/978-3-322-83423-2_7. URL https://doi.org/10.1007/978-3-322-83423-2_7.

[42] R Franz and G Wiedemann. Ueber die wärme-leitungsfähigkeit der metalle. *Annalen der Physik*, 165(8):497–531, 1853.

[43] SP Venkateshan. *Heat transfer*. Springer Nature, 2021.

[44] Dennis E Koppel. Analysis of macromolecular polydispersity in intensity correlation spectroscopy: the method of cumulants. *The Journal of Chemical Physics*, 57(11): 4814–4820, 1972.

[45] Kenneth S Schmitz. *Introduction to dynamic light scattering by macromolecules*. Elsevier, 2012.

[46] Malvern Instruments Ltd. Zetasizer nano user manual, 2013.

[47] Dynamic Light Scattering (DLS) | Unchained Labs. URL https://www.unchainedlabs.com/dynamic-light-scattering/. visited: 2023.01.19.

[48] Louis De Broglie. The wave nature of the electron. *Nobel lecture*, 12:244–256, 1929.

[49] Hidetaka Sawada, Naoki Shimura, Fumio Hosokawa, Naoya Shibata, and Yuichi Ikuhara. Resolving 45-pm-separated si–si atomic columns with an aberration-corrected stem. *Microscopy*, 64(3):213–217, 2015.

[50] Kenneth S Cole and Robert H Cole. Dispersion and absorption in dielectrics i. alternating current characteristics. *The Journal of chemical physics*, 9(4):341–351, 1941.

[51] Hannu Karttunen, Pekka Kröger, Heikki Oja, Markku Poutanen, and Karl Johan Donner. *Fundamental astronomy*. Springer, 2007.

[52] John R Howell and Robert Siegel. *Thermal radiation heat transfer*. CRC press, 1972. ISBN 978-1560328391.

[53] Stephan Kabelac and Dieter Vortmeyer. K1 Wärmestrahlung technischer Oberflächen. In Peter Stephan, Stephan Kabelac, Matthias Kind, Dieter Mewes, Karlheinz Schaber, and Thomas Wetzel, editors, *VDI-Wärmeatlas*, pages 1183–1199. Springer Berlin Heidelberg, Berlin, Heidelberg, 2019. ISBN 978-3-662-52988-1 978-3-662-52989-8. DOI: 10.1007/978-3-662-52989-8_68. URL "http://link.springer.com/10.1007/978-3-662-52989-8_68". Series Title: Springer Reference Technik.

[54] Michael Vollmer and Klaus-Peter Möllmann. *Infrared thermal imaging*. WILEY-VCH, 2010. ISBN 978-3-527-40717-0.

[55] Thermography in glass industry | InfraTec. URL https://www.infratec.eu/thermography/industries-applications/glass-industry/. visited: 2023.01.26.

[56] Michael Gary Christiansen. *Magnetothermal multiplexing for biomedical applications*. PhD thesis, Massachusetts Institute of Technology, 2017.

[57] Michael G Christiansen, Christina M Howe, David C Bono, David J Perreault, and Polina Anikeeva. Practical methods for generating alternating magnetic fields for biomedical research. *Review of Scientific Instruments*, 88(8):084301, 2017.

[58] Heinrich friedrich emil lenz. URL https://nationalmaglab.org/magnet-academy/history-of-electricity-magnetism/pioneers/heinrich-friedrich-emil-lenz/. visited: 2023.01.30.

[59] Reto B. Keller. *Skin Effect*, pages 135–143. Springer International Publishing, Cham, 2023. ISBN 978-3-031-14186-7. DOI: 10.1007/978-3-031-14186-7_10. URL https://doi.org/10.1007/978-3-031-14186-7_10.

[60] Ulrich Fischer, Roland Gomeringer, Max Heinzler, Roland Kilgus, Friedrich Näher, Stefan Oesterle, Heinz Paetzold, and Andreas Stephan. *Tabellenbuch Metall*. Europa-Lehrmittel, 2011. ISBN 978-3-8085-1725-3.

[61] New England Wire. Product selection guide, 2005. URL https://www.newenglandwire.com/wp-content/uploads/2018/03/NEW_Catalog.pdf. visited: 2023.02.15.

[62] Kunz Andreas. Senior Export Sales Manager, WIMA, personal correspondance, 2021.03.19.

[63] Estill I Green. The story of q. *American Scientist*, 43(4):584–594, 1955.

[64] micromod. synomag®-d, 2023. URL https://micromod.de/en/product-category/magnetic-particles/synomag-d-magnetic-particles/. visited: 2023.07.21.

[65] micromod. Technical data sheet for synomag®-d 70nm nh_2, 2022. URL https://micromod.de/wp-content/uploads/datasheets/104-01-701_tds_en.pdf. Version 5.01, visited: 2023.07.21.

[66] micromod. Technical data sheet for bnf-starch cooh 100nm nh_2, 2022. URL https://micromod.de/wp-content/uploads/datasheets/10-02-102_tds_en.pdf. Version 5.01, visited: 2023.07.21.

[67] Cindi L Dennis, Kathryn L Krycka, Julie A Borchers, Ryan D Desautels, Johan Van Lierop, Natalie F Huls, Andrew J Jackson, Cordula Gruettner, and Robert Ivkov. Internal magnetic structure of nanoparticles dominates time-dependent relaxation processes in a magnetic field. *Advanced Functional Materials*, 25(27):4300–4311, 2015.

[68] Fred Etoc, Elie Balloul, Chiara Vicario, Davide Normanno, Domenik Liße, Assa Sittner, Jacob Piehler, Maxime Dahan, and Mathieu Coppey. Non-specific interactions govern cytosolic diffusion of nanosized objects in mammalian cells. *Nature materials*, 17(8): 740–746, 2018.

[69] Manon Debayle, Elie Balloul, Fatimata Dembele, Xiangzhen Xu, Mohamed Hanafi, Francois Ribot, Cornelia Monzel, Mathieu Coppey, Alexandra Fragola, Maxime Dahan, et al. Zwitterionic polymer ligands: an ideal surface coating to totally suppress protein-nanoparticle corona formation? *Biomaterials*, 219:119357, 2019.

[70] Philipp Bender, Jeppe Fock, Cathrine Frandsen, Mikkel F Hansen, Christoph Balceris, Frank Ludwig, Oliver Posth, Erik Wetterskog, Lara K Bogart, Paul Southern, et al. Relating magnetic properties and high hyperthermia performance of iron oxide nanoflowers. *The Journal of Physical Chemistry C*, 122(5):3068–3077, 2018.

[71] Jean-Paul Fortin, Claire Wilhelm, Jacques Servais, Christine Ménager, Jean-Claude Bacri, and Florence Gazeau. Size-sorted anionic iron oxide nanomagnets as colloidal mediators for magnetic hyperthermia. *Journal of the american chemical society*, 129 (9):2628–2635, 2007.

[72] Vincent Connord, Pascal Clerc, Nicolas Hallali, Darine El Hajj Diab, Daniel Fourmy, Véronique Gigoux, and Julian Carrey. Real-time analysis of magnetic hyperthermia experiments on living cells under a confocal microscope. *Small*, 11(20):2437–2445, 2015.

[73] L-M Lacroix, Julian Carrey, and Marc Respaud. A frequency-adjustable electromagnet for hyperthermia measurements on magnetic nanoparticles. *Review of scientific instruments*, 79(9):093909, 2008.

[74] E Garaio, JM Collantes, F Plazaola, JA Garcia, and I Castellanos-Rubio. A multi-frequency eletromagnetic applicator with an integrated ac magnetometer for magnetic

hyperthermia experiments. *Measurement Science and Technology*, 25(11):115702, 2014.

[75] Iuliia P Novoselova, Andreas Neusch, Julia-Sarita Brand, Marius Otten, Mohammad Reza Safari, Nina Bartels, Matthias Karg, Michael Farle, Ulf Wiedwald, and Cornelia Monzel. Magnetic nanoprobes for spatio-mechanical manipulation in single cells. *Nanomaterials*, 11(9):2267, 2021.

[76] Kilian Vogele, Jonathan List, Günther Pardatscher, Nolan B Holland, Friedrich C Simmel, and Tobias Pirzer. Self-assembled active plasmonic waveguide with a peptide-based thermomechanical switch. *ACS nano*, 10(12):11377–11384, 2016.

[77] Jing Zhao, Hanquan Su, Gregory E Vansuch, Zheng Liu, Khalid Salaita, and R Brian Dyer. Localized nanoscale heating leads to ultrafast hydrogel volume-phase transition. *ACS nano*, 13(1):515–525, 2018.

[78] Sarah A Stanley, Jennifer E Gagner, Shadi Damanpour, Mitsukuni Yoshida, Jonathan S Dordick, and Jeffrey M Friedman. Radio-wave heating of iron oxide nanoparticles can regulate plasma glucose in mice. *Science*, 336(6081):604–608, 2012.

[79] Hugo Geerts, M De Brabander, Ronny Nuydens, Staf Geuens, Mark Moeremans, J De Mey, and Peter Hollenbeck. Nanovid tracking: a new automatic method for the study of mobility in living cells based on colloidal gold and video microscopy. *Biophysical journal*, 52(5):775–782, 1987.

[80] Jonathan M Crane, Peter M Haggie, and AS Verkman. Quantum dot single molecule tracking reveals a wide range of diffusive motions of membrane transport proteins. In *Colloidal Quantum Dots for Biomedical Applications IV*, volume 7189, pages 177–186. SPIE, 2009.

[81] Alexander Benke, Nicolas Olivier, Julia Gunzenhäuser, and Suliana Manley. Multicolor single molecule tracking of stochastically active synthetic dyes. *Nano letters*, 12(5): 2619–2624, 2012.

[82] Marc Zimmer. Green fluorescent protein (gfp): applications, structure, and related photophysical behavior. *Chemical reviews*, 102(3):759–782, 2002.

[83] Rudolf Simson, Erin D Sheets, and Ken Jacobson. Detection of temporary lateral confinement of membrane proteins using single-particle tracking analysis. *Biophysical journal*, 69(3):989–993, 1995.

[84] Damien Alcor, Géraldine Gouzer, and Antoine Triller. Single-particle tracking methods for the study of membrane receptors dynamics. *European journal of neuroscience*, 30 (6):987–997, 2009.

[85] Ming Xiao, Angie Phong, Connie Ha, Ting-Fung Chan, Dongmei Cai, Lucinda Leung, Eunice Wan, Amy L Kistler, Joseph L DeRisi, Paul R Selvin, et al. Rapid dna mapping by fluorescent single molecule detection. *Nucleic acids research*, 35(3):e16–e16, 2007.

[86] Hisashi Tadakuma, Yo Ishihama, Toshiharu Shibuya, Tokio Tani, and Takashi Funatsu. Imaging of single mrna molecules moving within a living cell nucleus. *Biochemical and biophysical research communications*, 344(3):772–779, 2006.

[87] Carlo Manzo and Maria F Garcia-Parajo. A review of progress in single particle tracking: from methods to biophysical insights. *Reports on progress in physics*, 78(12): 124601, 2015.

[88] Michael J Saxton and Ken Jacobson. Single-particle tracking: applications to membrane dynamics. *Annual review of biophysics and biomolecular structure*, 26(1):373–399, 1997.

[89] Akihiro Kusumi, Chieko Nakada, Ken Ritchie, Kotono Murase, Kenichi Suzuki, Hideji Murakoshi, Rinshi S Kasai, Junko Kondo, and Takahiro Fujiwara. Paradigm shift of the plasma membrane concept from the two-dimensional continuum fluid to the partitioned fluid: high-speed single-molecule tracking of membrane molecules. *Annu. Rev. Biophys. Biomol. Struct.*, 34:351–378, 2005.

[90] Felix Höfling and Thomas Franosch. Anomalous transport in the crowded world of biological cells. *Reports on Progress in Physics*, 76(4):046602, 2013.

[91] Aubrey V Weigel, Blair Simon, Michael M Tamkun, and Diego Krapf. Ergodic and nonergodic processes coexist in the plasma membrane as observed by single-molecule tracking. *Proceedings of the National Academy of Sciences*, 108(16):6438–6443, 2011.

[92] Yann Lanoiselée and Denis S Grebenkov. Revealing nonergodic dynamics in living cells from a single particle trajectory. *Physical Review E*, 93(5):052146, 2016.

[93] Aurélie Dupont and Don C Lamb. Nanoscale three-dimensional single particle tracking. *Nanoscale*, 3(11):4532–4541, 2011.

[94] Khuloud Jaqaman, Dinah Loerke, Marcel Mettlen, Hirotaka Kuwata, Sergio Grinstein, Sandra L Schmid, and Gaudenz Danuser. Robust single-particle tracking in live-cell time-lapse sequences. *Nature methods*, 5(8):695–702, 2008.

[95] Robert Brown. Xxvii. a brief account of microscopical observations made in the months of june, july and august 1827, on the particles contained in the pollen of plants; and on the general existence of active molecules in organic and inorganic bodies. *The philosophical magazine*, 4(21):161–173, 1828.

[96] Albert Einstein. Zur theorie der brownschen bewegung. *Annalen der physik*, 324(2): 371–381, 1906.

[97] Albert Einstein. Theoretische bemerkungen über die brownsche bewegung. *Zeitschrift für Elektrochemie und angewandte physikalische Chemie*, 13(6):41–42, 1907.

[98] Marian Von Smoluchowski. Zur kinetischen theorie der brownschen molekularbewegung und der suspensionen. *Annalen der physik*, 326(14):756–780, 1906.

[99] Paul Langevin. Sur la théorie du mouvement brownien. *Compt. Rendus*, 146:530–533, 1908.

[100] Ralf Metzler and Joseph Klafter. The restaurant at the end of the random walk: recent developments in the description of anomalous transport by fractional dynamics. *Journal of Physics A: Mathematical and General*, 37(31):R161, 2004.

[101] Edward U Condon. The franck-condon principle and related topics. *American journal of physics*, 15(5):365–374, 1947.

[102] Megan Amy Bryden and Eli Zysman-Colman. Organic thermally activated delayed fluorescence (tadf) compounds used in photocatalysis. *Chemical Society Reviews*, 50 (13):7587–7680, 2021.

[103] Mikhail Y Berezin and Samuel Achilefu. Fluorescence lifetime measurements and biological imaging. *Chemical reviews*, 110(5):2641–2684, 2010.

[104] Miłosz Pawlicki, Hazel A Collins, Robert G Denning, and Harry L Anderson. Two-photon absorption and the design of two-photon dyes. *Angewandte Chemie International Edition*, 48(18):3244–3266, 2009.

[105] August Köhler. *Mikrophotographische untersuchungen mit ultraviolettem licht*, volume 21. Zeitschrift für wissenschaftliche Mikroskopie und für mikroskopische Technik, 1904.

[106] Lumencor. Sola se ii light engine instruction manual, 2014. URL `https://www.newport.com/medias/sys_master/images/images/h7b/hae/8797264150558/SOLA-SE-II-Light-Engine-User-Manual.pdf`. visited: 2023.08.21.

[107] AHF Anlysentechnik. 50r/50t strahlenteiler uv-vis, 2023. URL `https://www.ahf.de/produkte/spektralanalytik-photonik/optische-filter/strahlenteiler/neutralteiler/1398/50r/50t-strahlenteiler-uv-vis`. visited: 2023.07.19.

[108] Danuser Lab. Danuserlab/u-track, 2021. URL `https://github.com/DanuserLab/u-track`. Version: 2.0 ; visited: 2023.07.23.

[109] Todd Saxton. The effects of partner and relationship characteristics on alliance outcomes. *Academy of management journal*, 40(2):443–461, 1997.

[110] L Cohen. A review of brownian motion based solely on the langevin equation with white noise. *Mathematical Analysis, Probability and Applications–Plenary Lectures: ISAAC 2015, Macau, China 10*, pages 1–35, 2016.

Publications

During the PhD I contributed to the aforementioned and further projects, from which the following publications arose:

Sabrina Koch, Anne-Bart Seinen, Michael Kamel, Daniel Kuckla, Cornelia Monzel, Alexej Kedrov, and Arnold J.M. Driessen, (2021). "Single-molecule analysis of dynamics and interactions of the SecYEG translocon." The FEBS Journal, 288(7), 2203-2221. https://febs.onlinelibrary.wiley.com/doi/epdf/10.1111/febs.15596

Valeska Rathe, Daniel Kuckla, Cornelia Monzel "Phase separation in biological membranes: An overview with focus on experimental effects of illumination and osmotic pressure changes" Advances in Biomembranes and Lipid Self-Assembly (2021) Volume 33, Elsevier (invited) https://doi.org/10.1016/bs.abl.2021.11.002

Daniel Alexander Kuckla, Julia-Sarita Brand, Andreas Neusch, Bastian Czech, Jan Vinzenz Jüttner, Amirarsalan Asharion, Iuliia Pavlovna Novoselova, Philipp Hagemann, Mathias Getzlaff and Cornelia Monzel "An efficient magnetothermal actuation setup for fast heating/cooling cycles or long-term induction heating of different magnetic nanoparticle classes“ Journal of Physics D: Applied Physics, under revision

Luisa Coen, Daniel Kuckla, and Cornelia Monzel "Case Study of Mobile or Immobile Obstacles in Supported Lipid Bilayer Systems and their Effect on Lipid Mobility“ Langmuir, submitted

Danksagung

An dieser Stelle möchte ich mich bei all denen bedanken, die mich während der Doktorarbeit begleitet haben.

Mein Dank gilt Frau Prof. Dr. Monzel dafür, dass sie mir die Möglichkeit gegeben hat, diese Arbeit in ihrer Gruppe anzufertigen und mir bei der Umsetzung der Projekte großen persönlichen Spielraum gelassen hat.

Vielen Dank an Prof. Dr. Mathias Getzlaff für die Bereitschaft, das Zweitgutachten anzufertigen.

Ich möchte mich für die tolle Zusammenarbeit bei allen Kollegen bedanken. Dabei gilt mein besonderer Dank auch den von mir betreuten Studenten, durch deren Fragen ich noch viel lernen konnte.

Ich möchte mich bei meiner Familie und meinen Freunden bedanken, die mich auch vor der Arbeit bei allen Vorhaben unterstützt haben, wobei mein besonderer Dank meinen Eltern und meiner Frau gilt.